Constraining the dynamics and masses of the TRAPPIST-1 planets with the transit timing variations method

Auteur : Houge, Adrien
Promoteur(s) : Gillon, Michaël
Faculté : Faculté des Sciences
Diplôme : Master en sciences spatiales, à finalité approfondie
Année académique : 2019-2020
URI/URL : http://hdl.handle.net/2268.2/9196

University of Liège
Faculty of sciences
Astrophysics, Geophysics and Oceanography department

Constraining the dynamics and masses of the TRAPPIST-1 planets with the transit timing variations method

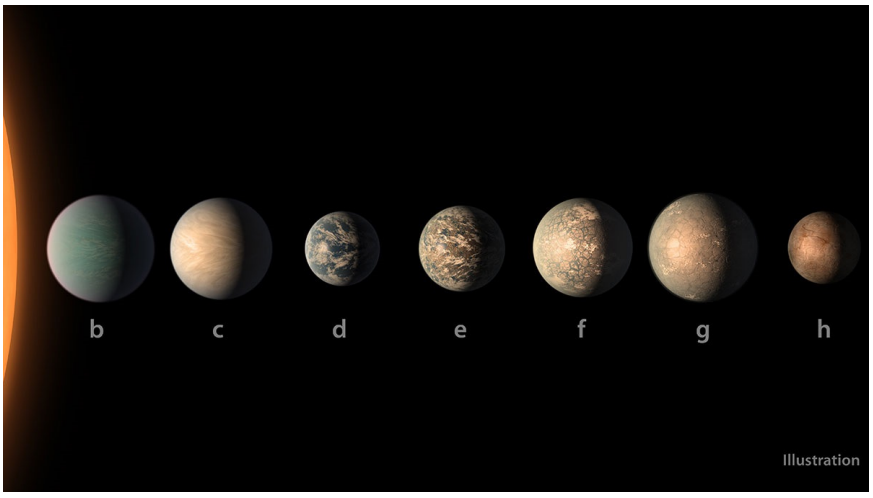

Thesis presented by **Adrien HOUGE** to
obtain the **Master's degree in Space Sciences**

Supervisor:
Michaël Gillon

Board of Examiners:
Olivier Absil
Laetitia Delrez
Fran Pozuelos
Valerie Van Grootel

June 2020

Contents

Acknowledgements

First of all, I would like to sincerely thank my supervisor, Michaël Gillon, who selected me for this amazing project. This Master thesis offered me the possibility to develop my skills in several domains and gave me the opportunity, thanks to a complete immersion in a research environment, to confirm the fact that a research-related career is what I want to do with my life. I thank Elsa Ducrot for all her precious advice notably concerning the use of the MCMC algorithm. Despite being focused on her PhD and the writing of her article, she always managed to find time for me. I am grateful for all the help provided by Lionel Garcia concerning the use of SPECPHOT, and Sandrine Sohy for the informatics-related issues. I acknowledge Eric Agol for useful discussions about the transit timing variations method, and the members of the Board of Examiners, Olivier Absil, Laetitia Delrez, Fran Pozuelos, and Valerie Van Grootel, for the time they will devote to this Master thesis.

Then, I would like to use this section for a special thanks to Michaël De Becker, who supported me during all the important steps of my academic experience, from my registration in the Master in Space Sciences to the PhD applications, passing by the organization of my Erasmus in Oulu, Finland. This international exchange was a major turning point in my academic and personal life, and I am very grateful towards him and the University of Liège for making it possible.

In addition, I would like to thank my family, Sabrina, Philippe, Améline, and Eliott, for all the support during these five years at the University of Liège, and all the future support during my PhD in Exeter, England.

Finally, I thank all my friends who helped to take my mind off when I needed some breaks, notably during the months of lock-down. I think notably about François, Alexis, Arnaud, Thibault and Julien from the EMH, Laura, Clémence, Margot, Dima, Guillaume, and Jascal. But also all my amazing international friends met during the Erasmus in Oulu, Jakob, Lili, Felix, Mojo, Pedro, Maeva, Samuel, David, and Ella. Last but not least, a very special thanks to my partner and best Tirolintie flatmate, Angelica. Despite being at more than 3000km from me, it feels like we are always next to each other.

CHAPTER 1

Theoretical introduction

1.1 Exoplanetology

Since the dawn of Humanity, we have tried to catch the meaning of our role in the Universe. Most of the ancient cultures used metaphysical models to understand human nature and make logical sense of the planets, the stars, the Moon, the Sun and their respective motions. The geocentric model, mainly supported by Aristotle and Ptolemy in Ancient Greece, was the first in attempting to provide an explanation without relying on supernatural or divine beliefs. In this model, the Earth and humans are the center of everything, the stars occupy a distant fixed background, and the planets, the Sun and the Moon are in circular motions around the Earth. Even though the latter concept had been accepted for more than a thousand years in Europe, it did not survive the Copernican revolution and was replaced by the heliocentric model, thanks to the rise of Newtonian mechanics combined with rigorous observations. In consequence, the Sun was gradually considered as an individual star similar to any visible one when looking up at the sky. And as a result, the Earth lost its singularity and became one common planet lost in the many others potentially cohabiting in the Universe. Following this approach, the evolution of life had no reason to be limited to a single planet and could have emerged in any other worlds, provided conditions for life development are met.

Exoplanetology is based upon this thought and is dedicated to the search and study of extrasolar planets. Its most ambitious objective is the detection of traces of life beyond the Solar System. On top of that, other precious information can be gathered from this field. For example, the discovery of Jupiter-sized planets orbiting close to their host stars, named hot Jupiters, enabled scientists to confirm the fundamental process of planetary migration, which is of major importance in the evolution of planetary systems, Solar System included (see Nice model [1]).

However, the detection of exoplanets remained a daunting task until the end of the last century. Their luminosity depends on their size, temperature and albedo (i.e. their ability to reflect the light from their host stars) and even under the best circumstances, it is extremely faint compared to the brightness of their host stars. Moreover, the size of a planetary system is small as opposed to the distance between the Earth and this system, resulting in a low angular separation between an exoplanet and its host (smaller than a second of arc). This makes the direct observation of exoplanets extremely challenging, which explains why most of the objects known so far have been discovered through indirect methods.

It is Otto Struve who paved the way in 1952. In its article "*Proposal for a project of high-precision stellar radial velocity work*" he argued that, provided a significant improvement in precision, putative short-period giant exoplanets could be detected by radial velocity and eclipse techniques, used at that time to study eclipsing binaries. Forty-three years later, in 1995, Michel Mayor and Didier Queloz used the first of these two techniques to announce the first genuine detection of an exoplanet, the gas giant 51 Pegasi b [2]. For their work, they were awarded the Nobel Prize in Physics in 2019. In the years that followed, several methods were developed and even more exoplanets were detected (Fig.1.1). As each method is more practical and efficient for different populations of exoplanets (e.g. larger sizes and shorter orbital distances for transits, or larger sizes, orbital distances and temperatures for imaging), the discovery of a wide variety of objects was made possible (Fig.1.2). Throughout years of technical improvement, instruments have increased their sensitivity and scientists have been enabled to push the limits of every method.

Today, 25 years after the first discovery, we can count more than 4000 confirmed exoplanets with more than a half of them by the method that will be the main focus of this Master thesis – the transit method.

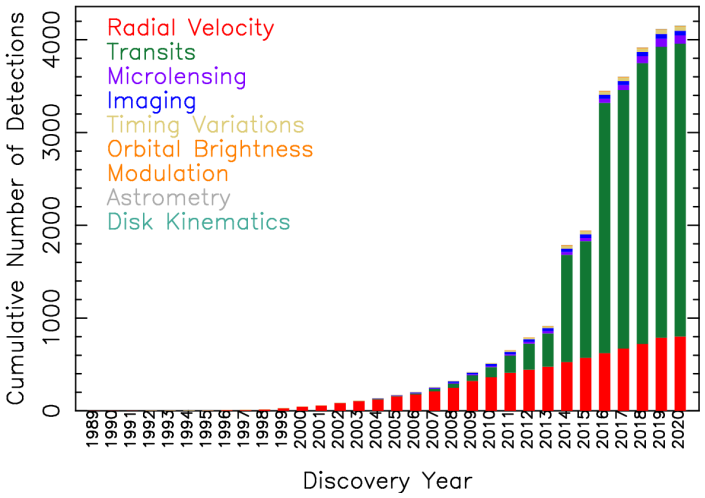

Figure 1.1: Cumulative number of exoplanet detections per year for different methods. This plot was made with data from April 2020. The sharp increase around 2016 is due to the transit survey of the Kepler Space Telescope. [3]

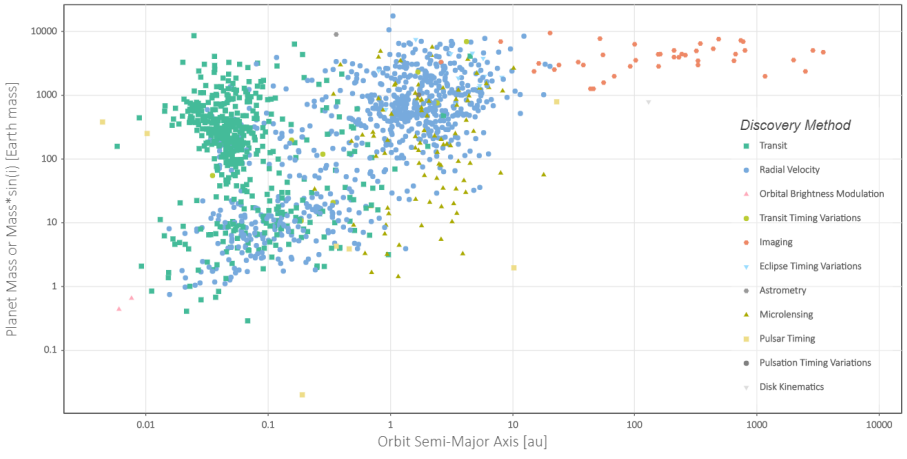

Figure 1.2: Approximate masses and orbital distances of known planets and exoplanets obtained from April 2020 data. We can see how each method works preferably for certain masses and distances. [3]

1.2 Transit

As outlined at the end of the first section, the transit method has been the most efficient one so far in the discovery of new extrasolar planets. It consists in photometric measurements of a star in order to detect a drop in the received flux, which could be associated to the crossing of its disk by a planet in orbit around it. Over the twentieth century, several discussions about the detection of exoplanet transits had been initiated [4]. The first actual implementation awaited 1996 and the mission proposal FRESIP (FRequency of Earth-Sized Inner Planets) of William Borucki et al. [5], which was designed to study the frequency of Earth-sized planets around Sun-like stars, and which is, in fact, the proposal behind the Kepler mission. The first detection of an exoplanet using the transit method was in 1999, with the hot Jupiter HD209458b already known from radial velocity measurements [6]. The first planet discovery due to a photometric survey came in 2002, with OGLE-TR-56b [7], a hot Jupiter of $1.30R_{\mathcal{Y}}$. Since then, nearly 3000 exoplanets have been identified through transit measurements, not only with the help of the Kepler Space Telescope ([8], [9]) but also of other dedicated surveys like WASP [10].

In this section, I will describe the transit method and how it is used in a context of exoplanet discovery and characterization.

1.2.1 Method

In the event that we reach a reasonable level of geometric alignment between two objects and an observer (typically on the Earth), eclipses may appear. During such a phenomenon, one body passes in front of the other one and partly blocks its light from the observer's perspective (e.g. the solar eclipse which occurs when the Moon passes in front of the Sun, as seen from the Earth).

When the concerned astronomical system is an exoplanet and its host star, there are two types of eclipses we can see from our position. An exoplanet passing in front of its host star darkens a part of the stellar disk, resulting in a received flux decrease from the system. This phenomenon is called primary eclipse, or transit. On the contrary, when the exoplanet moves behind its host star (half an orbital period later if the orbit is circular), the star blocks the planet, also resulting in a received flux drop, although different in intensity. This phenomenon is referred to as secondary eclipse, or occultation. In this work, only the primary eclipse will be examined as it constitutes the core of the transit method.

Photometric measurements taken in sequence constitute what is called a lightcurve, displaying the variation of the received flux as a function of time. In the case of a transit event (Fig.1.3), it is mainly characterized by the following three geometrical equations ([11], [12], [13]).

1. The transit depth ΔF:

$$\Delta F = \frac{F_{notransit} - F_{transit}}{F_{notransit}} = \frac{R_P^2}{R_\star^2} \tag{1.1}$$

   For a giant planet transiting a solar-sized star, the decrease in amplitude is about 1% of the total stellar flux. For a smaller terrestrial planet, this value goes down 0.01%. Therefore, transit surveys require great precisions unless smaller hosts like M dwarfs are targeted.

2. The total transit duration t_T:

$$t_T = \frac{P}{\pi} \arcsin\left[\frac{R_\star}{a}\left(\frac{\left[1+(R_p/R_\star)\right]^2 - \left[(a/R_\star)\cos i\right]^2}{1-\cos^2 i}\right)^{1/2}\right] \tag{1.2}$$

3. The transit shape, represented by the ratio between the duration of the full superposition (flat) part t_F and t_T:

$$\frac{t_F}{t_T} = \frac{\arcsin\left[\frac{R_\star}{a}\left(\frac{\left[1-(R_p/R_\star)\right]^2 - \left[(a/R_\star)\cos i\right]^2}{1-\cos^2 i}\right)^{1/2}\right]}{\arcsin\left[\frac{R_\star}{a}\left(\frac{\left[1+(R_p/R_\star)\right]^2 - \left[(a/R_\star)\cos i\right]^2}{1-\cos^2 i}\right)^{1/2}\right]} \tag{1.3}$$

Where:

- R_p (resp. $R_\star$) is the radius of the exoplanet (resp. host star);
- P is the orbital period, determined by the time interval between two consecutive transits;
- a is the orbital semi-major axis;
- i is the inclination of the orbit;
- F is the total received flux from the star.

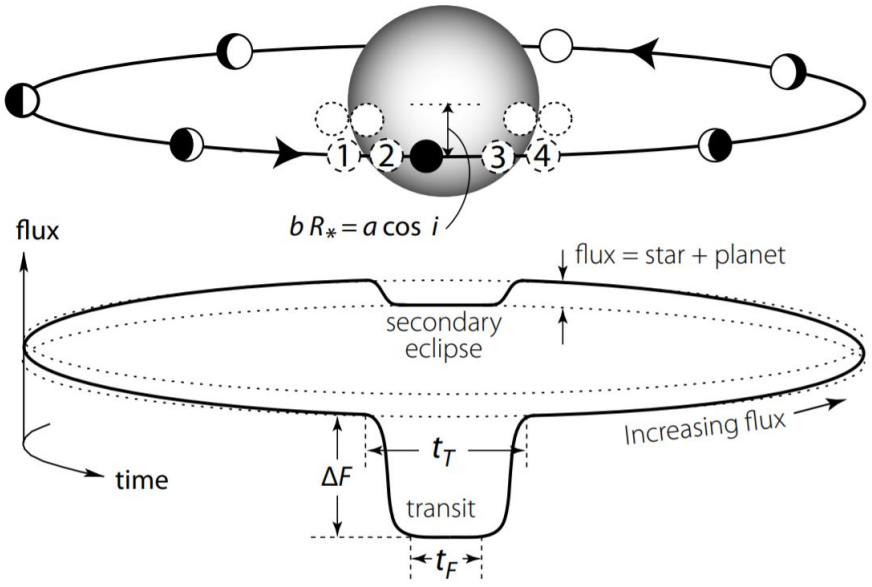

Figure 1.3: Diagram showing the evolution of the flux of a transiting and occulting system along a full orbit of the planet. During transit, we observe a first flux drop. Then, the flux received by the system increases as the planet's day side comes more and more into view. Afterwards, we see the second drop corresponding to the occultation, followed by a decrease in received flux as the planet's night side comes more into view. [12]

From these equations can be constructed three dimensionless parameters. The planet-star radius ratio is, directly from (1.1):

$$\frac{R_P}{R_\star} = \sqrt{\Delta F} \tag{1.4}$$

The impact parameter b which, as seen on Figure 1.3, represents the projected distance between the exoplanet and star center during mid-transit in unit of $R_\star$, is, from (1.3) and (1.4):

$$b = \left[\frac{(1-\sqrt{\Delta F})^2 - \left[\sin^2(t_F\pi/P)/\sin^2(t_T\pi/P) \right](1+\sqrt{\Delta F})^2}{1 - \left[\sin^2(t_F\pi/P)/\sin^2(t_T\pi/P) \right]} \right]^{1/2} \tag{1.5}$$

And the ratio $a/R_\star$ is, from (1.2) and (1.4):

$$\frac{a}{R_\star} = \left[\frac{(1+\sqrt{\Delta F})^2 - b^2\left[1 - \sin^2(t_T\pi/P)\right]}{\sin^2(t_T\pi/P)} \right]^{1/2} \tag{1.6}$$

In addition, we obtain an expression for the stellar density $\rho_\star$ from (1.6) and Kepler's third law (assuming $M_p << M_\star$):

$$\rho_\star = \frac{M_\star}{R_\star^3} = \frac{4\pi^2}{P^2 G}\left(\frac{a}{R_\star}\right)^3 = \frac{4\pi^2}{P^2 G}\left[\frac{(1+\sqrt{\Delta F})^2 - b^2\left[1 - \sin^2(t_T\pi/P)\right]}{\sin^2(t_T\pi/P)} \right]^{3/2} \tag{1.7}$$

Therefore, through the lightcurve, we have a knowledge of $R_\star/a$ and b, hence the orbital inclination of the exoplanet is directly obtained from the definition of the impact parameter:

$$i = \arccos\left(\frac{bR_\star}{a}\right) \tag{1.8}$$

The other physical parameters of the system - $R_\star$, R_p and a - can also be determined from the transit parameters, provided some external information about the star. The typical approach consists in deducing the stellar radius by another means which then leads to a and R_p with the equations (1.4) and (1.6).

For example, this calculation could be executed based on spectroscopic observations of the star. They provide T_{eff}, [Fe/H] and $log(g)$ which allow to derive the mass of the star when associated with evolution models. With the mass, and the density known via transit measurements (1.7), the radius of the star is established.

As far as nearby stars are concerned, we could also directly obtain $R_\star$ from interferometric observations or thanks to a good knowledge about the luminosity, distance and effective temperature [14].

In some cases, it is also feasible to use a stellar mass empirical law calibrated with a population of known eclipsing binaries, such as the one presented by G.Torres [15]. Here again, together with the density taken from transit data, the radius is inferred. However, we note that this method cannot be applied to very low-mass stars like TRAPPIST-1 due to their poor sampling in known eclipsing binaries.

In the context of this discussion on transit lightcurves, it is worth mentioning the effect of limb darkening that can affect them significantly [11]. When we observe a star, we look into its atmosphere down to an optical depth $\tau \sim 1$, as it becomes opaque after this. Owing to geometric considerations, the penetration of different lines of sight to an optical depth of unity corresponds to different depths in the stellar photosphere, so as we look towards the limb, we see higher photospheric layers. However, the temperature varies with the altitude so higher layers are colder, hence their emissions are less intense. As a consequence, the limb is less bright and appears darker than the center. We note that this effect decreases with the wavelength. It can be seen mathematically by considering the stellar intensity to be related to the Planck function B_λ. By definition, its variation according to the temperature dB_λ/dT is inversely proportional to λ^4, so at higher wavelengths, the intensity varies less across the stellar disk and the limb darkening is attenuated.

The consequence on a transit lightcurve concerns its shape. When the planet passes in front of the bright center, the flux drop is larger than $R_P^2/R_\star^2$, but when it is near the darker limb, the drop is smaller. This effect tends to round off the signal (Fig.1.4). When it comes to lightcurve analysis, it is important to take this effect into account. It is commonly done by describing the intensity profile on the stellar disk with a quadratic law [16]:

$$\frac{I(\mu)}{I(1)} = 1 - u_1(1-\mu) - u_2(1-\mu)^2$$

Where $I(\mu)$ is the intensity in the line of sight, $I(1)$ is the intensity at the center, $\mu = cos(\gamma)$ where γ represents the angle of our line of sight, and u_1 and u_2 are the quadratic limb darkening coefficients. We note that it is also possible to use a linear equation, but progress in stellar atmosphere modeling showed that it is not the more appropriate. Oppositely, more complex laws can be used to analyze transit lightcurves of extremely-high precisions, e.g. a four-coefficient law [17].

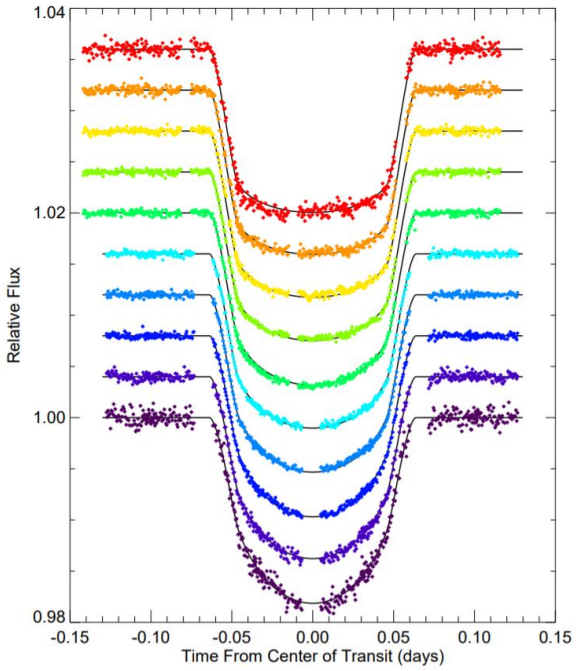

Figure 1.4: Transit lightcurves of HD 209458b observed at different wavelengths ($0.32\mu m$ to $0.97\mu m$). A vertical offset is added to construct the figure. For shorter wavelengths (bottom) the limb darkening is more intense and the round-off more visible than at longer ones (top). [18]

1.2.2 A discovery tool

To discover new transiting exoplanets, photometric blind searches are carried out in order to detect periodic transit-like signals. Based on geometric considerations, it is possible to compute the probability $p_{transit}$ (resp. p_{occult}) for an exoplanet to be transiting (resp. occulting). Eclipses can be seen by any observer located in the shadow cone of the system. Since the exoplanet orbits its host star, the shadow cone describes a band projected on the celestial sphere (Fig.1.5). The probability to observe an eclipse is therefore the probability for the observer to be located inside this band. For the general case of an elliptic orbit, the equations for both primary and secondary eclipses are written as follows [11]:

$$p_{transit} = \left(\frac{R_\star \pm R_p}{a}\right)\left(\frac{1 + e\sin\omega}{1 - e^2}\right) \tag{1.9}$$

$$p_{occult} = \left(\frac{R_\star \pm R_p}{a}\right)\left(\frac{1 - e\sin\omega}{1 - e^2}\right) \tag{1.10}$$

Where:

- e is the orbital eccentricity;
- ω is the argument of pericenter. For a transit (resp. occultation), we have $\omega + f = +\frac{\pi}{2}$ (resp. $\omega + f = -\frac{\pi}{2}$), where f is the true anomaly.

These equations can be used to calculate the probability for an exoplanet orbit to be favorably inclined for an eclipse, provided some constraints (or assumptions) on its eccentricity and argument of pericenter. If we consider grazing eclipses, the + sign is chosen in both equations (1.9) and (1.10), otherwise, the − sign is chosen. The shadow cone has a larger opening angle Θ in the first case, hence probabilities are higher when considering grazing eclipses. These equations[1] also indicate that an eclipse occurring at the pericenter of an eccentric orbit is more likely to be detected. Even though the time passed around it is shorter, the distance from the star is smaller, resulting in a higher cone-opening angle.

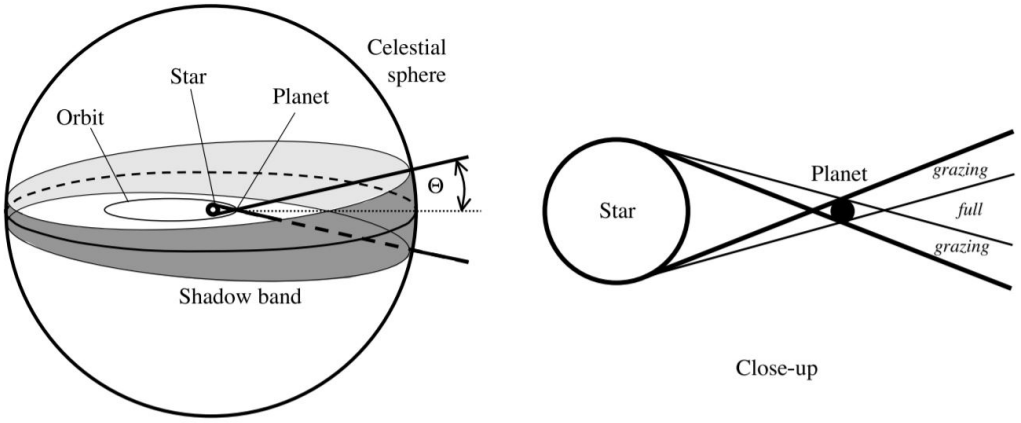

Figure 1.5: Band swept out by the shadow cone projected on the celestial sphere. The opening angle Θ is larger when grazing eclipses are considered. [11]

[1] $w = +\frac{\pi}{2}$ for a transit occurring at the pericenter, hence $p_{transit}$ is maximized (1.9). For an occultation at the pericenter, $w = -\frac{\pi}{2}$ and we also maximize the probability (1.10).

In the specific case of a circular orbit, with $R_p << R_\star$, the probabilities are [11]:

$$p_{transit} = p_{occult} = \frac{R_\star}{a} \approx 0.005 \left(\frac{R_\star}{R_\odot} \right) \left(\frac{a}{1AU} \right)^{-1} \tag{1.11}$$

We can see that when looking at circular orbits, transits and occultations come together. But in the general case of an elliptic orbit, we could be facing a primary eclipse without the secondary and vice versa. By applying (1.11), we get a probability of 0.005% for an Earth analog exoplanet, and 0.001% for a Jupiter analog. Given these low probabilities, the use of wide fields by transit surveys takes on a crucial dimension in order to observe simultaneously many stars and compensate for the rarity of events. It is worth mentioning that this is a purely geometric consideration, which does not include the instrument limit. Even though an Earth analog is five times more likely to be transiting than a Jupiter analog, the associated drop in brightness is one hundred times smaller (1.1), hence it is more challenging to detect.

When eventually a transit-like signal is observed, it is classified as candidate. In order to confirm the source as a new exoplanet, other astronomical objects subject to the same variability need to be discarded to avoid false positives – e.g. a grazing eclipsing binary, an eclipsing binary in the background, or a brown dwarf transit. To this end, further studies are required, including Doppler spectroscopy, higher-resolution transit photometry and imaging, and catalogs of known contaminating sources. As an example, Fressin et al. [19] estimated, based upon statistical studies, that about 9% of the NASA's Kepler space telescope candidates should be false positives.

If eventually the transit-like signal is confirmed to be an exoplanet, the lightcurve is used to derive the first exoplanet parameters as depicted in Subsection 1.2.1.

1.2.3 Further studies

Further studies of a known transiting exoplanet enable scientists to gather precious information about it and its system. This section will present some of them.

Transit spectroscopy

In the previous section, we assumed that exoplanets have a sharp edge, at R_p, whereas in reality the atmosphere surrounding them makes this edge fuzzy. When a primary eclipse occurs, a fraction of the stellar light passes through this gas layer. At certain wavelengths, depending on the atmospheric composition, it is more opaque, resulting in more absorption of stellar flux. As a consequence, the apparent planet radius increases, by a factor of a few atmospheric scale heights H, where H is defined by[2] [12]:

$$H = \frac{k_B T}{\mu_m g} \tag{1.12}$$

[2]We assume here a well mixed atmosphere, like the homosphere of the Earth. When it is not the case, like in the heterosphere of the Earth, each atmospheric compound follows its own scale height, and μ_m is replaced by the compound mass.

With:

- $k_B = 1.3806 \times 10^{-23} J/K$ is the Boltzmann constant;
- T is the atmosphere's temperature;
- μ_m is the mean molecular mass;
- g is the planet's surface gravity.

By definition of the transit depth (1.1), an increase of the radius implies an increase of ΔF. Denoted by δ, the transit depth increment follows [12]:

$$\delta \approx 2N_H \frac{R_p H}{R_\star^2} \tag{1.13}$$

Where :

- N_H is the number of effective scale heights, typically around 5 [20];
- $R_\star$ is the host star radius.

The opacity of the atmosphere, thus the transit depth, depends on the wavelength. Therefore, a spectroscopic time-series observation of a transit gives insight into atmospheric absorption, from which we infer the main components in the atmosphere. This method is referred to as **transmission spectroscopy**.

In accordance with (1.12) and (1.13), the signature appears stronger for high temperature low-density atmospheres mainly composed of hydrogen, hence hot Jupiters are effective targets in the scope of such spectroscopic studies. In order of magnitude, an increment $\delta \sim 10^{-4}$ is expected for a typical hot Jupiter[3] orbiting a solar-sized star. This value drops down to 10^{-6} for an Earth-like planet[4] – too small to become detectable by any existing or upcoming instruments. Nevertheless, equation 1.13 shows that the transmission signals scale as the inverse of the square of the host radius. For a star ten times smaller than the Sun, similar in size to the smallest M-dwarfs, the atmospheric signals of a terrestrial planet should thus be as large as those of a hot Jupiter in front of a Sun-like star, and within reach of current technology. For this reason, the TRAPPIST-1 planets, orbiting a Jupiter-sized M-dwarf, are promising candidates for atmospheric characterization of Earth-sized objects.

Interesting results came from transit spectroscopy, such as the identification of H_2O in the hot Jupiter WASP19b [21] and hot Neptune HAT-P-26b [22], or the discovery of escaping atmospheres (for instance [23]). However, the current instrumental precision limits us to exoplanets with extended atmospheres such as hot Jupiter and prevents us from acquiring a greater knowledge of the actual atmospheric composition. Nonetheless, it is a promising method and it is certain that future instruments such as the James Webb Space Telescope will go deeper in disclosing the atmospheric properties of these worlds [24].

Rossiter-Mc Laughlin effect

As a star rotates around its rotational axis, one part of the stellar disk is approaching us while the other is receding, resulting in blueshifted and redshifted lights coming from these

[3] $T = 1300K$, $g = 25m/s^2$, $R_p \sim R_{♃}$ and $\mu_m = 2u$, by assuming a H dominated atmosphere.
[4] $T = 273K$, $g = 10m/s^2$, $R_p \sim R_\oplus$ and $\mu_m = 28u$, by assuming an Earth-like atmospheric composition.

separate parts. As an exoplanet transits its rotating host star (Fig.1.6), it progressively blocks slightly more blueshifted or redshifted light, adding up a small spectroscopic signal to the orbital Doppler shift (Fig.1.7). The maximum amplitude of the signal follows [11]:

$$\Delta V_{RM} \approx \left(\frac{R_p}{R_\star}\right)^2 \sqrt{1-b^2}(v_\star \sin i_\star) \tag{1.14}$$

Where:

- R_p (resp. $R_\star$) is the radius of the exoplanet (resp. host star);
- b is the impact parameter;
- $v_\star \sin i_\star$ is the component of the stellar equatorial rotation velocity in the plane of the sky.

Besides, the shape of the signal depends on λ, the angle between the projections of the stellar rotation axis and the planet's orbital axis onto the plane of the sky. The study of this angle teaches us about the dynamical history of the system. For example, planetary formation simulations favor a formation of hot Jupiters above the snow line followed by an inward migration, rather than a formation in situ. However, plenty of migration scenarios are possible. A follow-up of hot Jupiters with the Rossiter-Mc Laughlin effect revealed that a significant fraction of them have misaligned orbits that are better explained by tidally induced migrations subsequent to a planet-planet or planet-star scattering event, rather than other processes such as disk-driven migration [25].

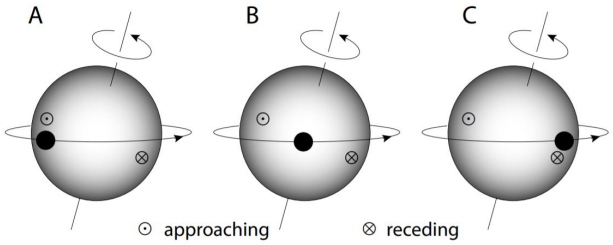

Figure 1.6: An exoplanet transiting its rotating host star. In A, it obscures a more blueshifted part of the stellar disk, while in C it obscures a more redshifted part. [12]

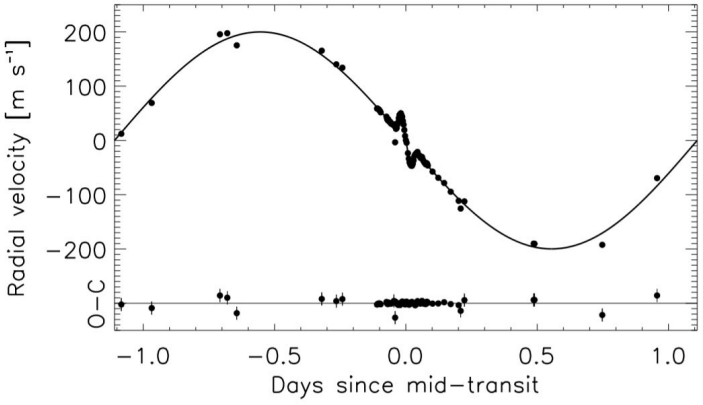

Figure 1.7: Phase-folded radial velocities of HD 189733 from spectroscopic measurements. The main signal is created by the orbital motion of HD 189733b while the smaller central signal is the Rossiter-Mc Laughlin anomaly. [26]

In addition to the transmission spectroscopy and the Rossiter-Mc Laughlin, the transit timing variations method is a precious tool to further characterize an exoplanet and the dynamics of its system. Since this method is the main subject of this Master thesis, the next section will be entirely dedicated to it.

1.3 Transit timing variations

In this section, I will detail the transit timing variations method, usually abbreviated TTV.

1.3.1 Method

In a two-body system consisting in a star of mass $m_\star$ and a planet of mass m_p, the planet follows an elliptic trajectory with a constant orbital periodicity P in accordance with the Kepler laws (*Keplerian* orbit) [27]:

$$P = 2\pi\sqrt{\frac{a^3}{G(m_\star + m_p)}}$$

If we are dealing with a transiting exoplanet, the time interval between two transits, and the duration of each transit, are constants.

But in a **multiplanetary** system, we have additional gravitational interactions between planets. They act like a perturbation and create deviations from the standard Keplerian orbit, especially in the orbital elements a, e, and ω. As a consequence, planets are following non-Keplerian orbits and, if they are transiting, the timing between two transits (resp. the duration) can vary. Seeking for these variations in a multiplanetary system constitutes the core of the Transit Timing Variation = TTV (resp. Transit Duration Variation = TDV) method. In this work, only the TTV will be considered.

The intensity of the TTV is linked to the system architecture, the largest variations are expected from planets near orbital resonance [27]. In this configuration, two bodies or more experience periodic gravitational interactions due to their orbital elements being related by an integer ratio, which greatly enhances their mutual influences. Systems like Kepler-223 or TRAPPIST-1 made up respectively of four and seven planets in a chain of resonances are therefore perfect targets for TTV study.

Usually, TTVs are represented as an Observed-Calculated (**O-C**) diagram [27]. The observed times are obtained from data on transit surveys, while the calculated times are based upon a constant-period model (Keplerian orbit) and found according to the equation:

$$C = T_0 + P \times E \tag{1.15}$$

Where P is the period, E is an integer transit number, called epoch, and T_0 is the time of the transit numbered $E = 0$. Their subtraction corresponds to the timing deviations from the Keplerian reference. Refer to Figure 1.8 to see an example of an O-C diagram.

After transit variations are found, the masses and orbits of the planets can be recovered from numerical integration of an N-body system. This constitutes an inversion problem: instead of simulating a system with a known dynamical state to fully predict orbital deviations, we do the opposite by recovering its dynamics from a set of observed time variations. This challenging task requires an optimized N-body integrator as well as a significant set of transit data [29].

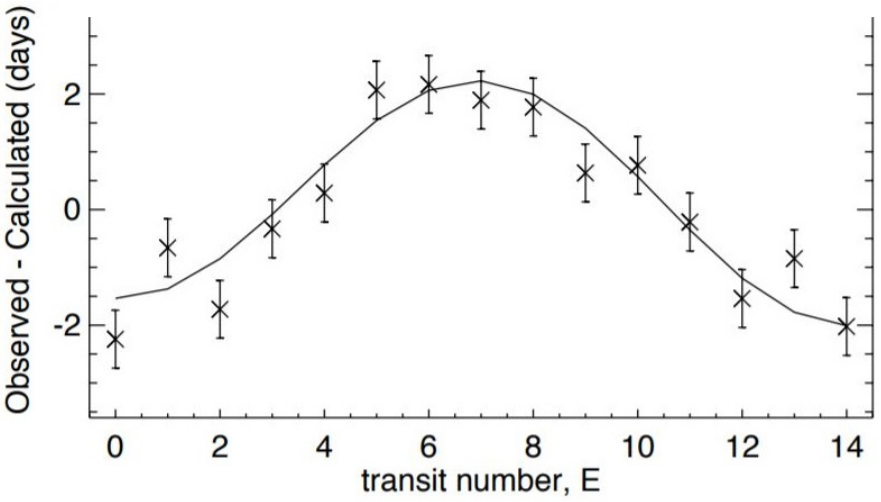

Figure 1.8: O-C diagram representing the Transit Timing Variations (TTVs) modeled from transits of WASP-47b [28]. The perturbations are greatly exaggerated. O-C < 0 (resp. > 0) means that the transit times come earlier (resp. later) than the constant-period model. A sinusoidal function is plotted as a line for illustrative purpose. [27]

1.3.2 Results

Miralda-Escudé initiated the first discussion on transit timing variations due to planetary interactions in 2002 [30]. Two other papers were successively released in 2005, going into more detail about the crucial effect of resonances ([31], [32]).
The Kepler telescope achieved the first tangible detection of TTVs. In the system Kepler-9 were detected two Saturn-sized exoplanets, which displayed large variations (Fig.1.9), giving information on the dynamics of the system. In this respect, Holman et al. [33] attributed these variations to a near 2:1 orbital resonance between the two objects.

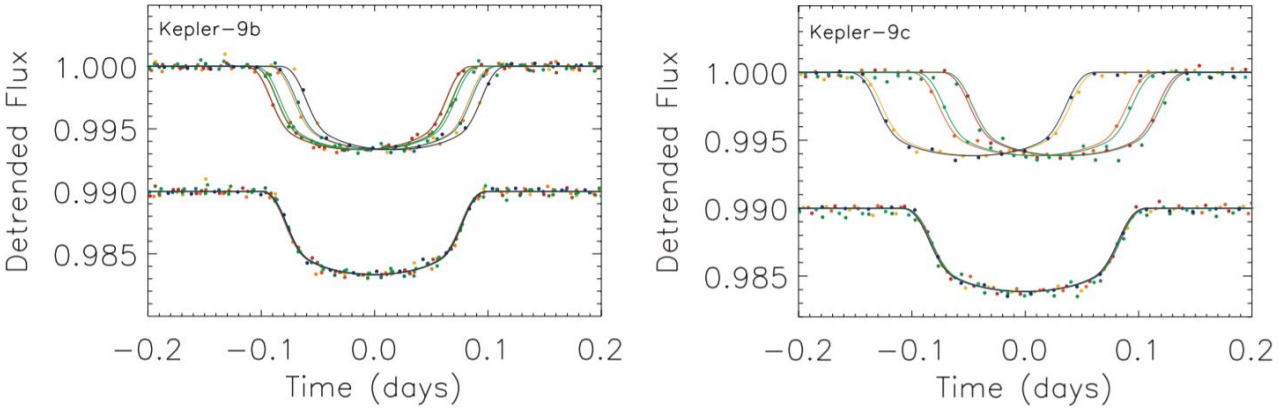

Figure 1.9: Lightcurves for Kepler-9b and c. The top curves show the displacements in time related to different transits due to TTVs (points and lines colored by transit epoch). For Kepler-9b (resp. c), we have variations up to ~ 4min (resp. ~ 39min). The bottom curves (moved downward for clarity) show the transits shifted to a common center. [33]

Afterwards, many discoveries followed, and nowadays more than 100 extrasolar systems indicate transit variations [27]. Their study using the TTV method offers several opportunities, depending on the context. On the next page are the most important cases detailed.

– **Candidate confirmation**: As mentioned in Subsection 1.2.2, a newly discovered transit-like signal needs further investigation to corroborate the fact that an exoplanet would have created such signal. The TTV method provides, under certain circumstances, a way to make confirmations.

Let's consider a pair of planets. The conservation of energy implies in many cases that their interaction will lead to an anti-correlated change of their periods: while one planet has a variation due to the influence of the second, the second simultaneously has a variation with an opposite sign (and a different amplitude). Therefore, the presence of anti-correlated TTV signals supports the evidence that the candidates are true planets [27]. This method for confirmation of exoplanets has been mainly used with Kepler candidates, and there are different techniques to detect anti-correlation. See for example the article of J.H. Steffen et al. [34] that confirmed four planetary systems with a Fourier-domain study.

– **Exoplanet detection**: Some transiting exoplanets display TTVs, but without any known companion that could explain these variations. This might fairly be due to the presence of an additional planet in the system, not discovered yet because either it is not transiting or its long orbital period reduces the likelihood of observation. TTV measurements can then be used to characterize this object (e.g. possible orbits, mass limit) [12]. We notice that this is the same approach as the method used to discover Neptune in 1846, with which the orbital deviations of a known object are studied to infer the presence of another one.

The use of TTV to detect new exoplanets has been performed in a number of cases. A good example is Kepler-88b which showed transit timing variations with an amplitude of 12 hours. Nesvorný et al. [35] related these to an additional object, Kepler-88c, which was then confirmed with the radial velocity method.

– **Exoplanet characterization**: Known exoplanets in a multiplanetary system can be further studied with the TTV method to constrain their orbital parameters and masses. The mass is particularly interesting to obtain. Along with the radius deduced from transit survey, it allows scientists to calculate the average density, hence giving insight on the internal composition. Such data are of major importance when studying the habitability, or the formation processes from the protoplanetary disk.

In general, mass estimates are determined by radial velocity measurements. It must however be combined with another method (e.g. transit method) to obtain the inclination i, otherwise, RV will only provide $M_p sin(i)$, the estimated minimal mass of the object [12]. But with the TTV method, if the multiplanetary system architecture does not keep us from addressing the inversion problem, we can in fact obtain excellent mass estimates. See for example the article of S.L.Grimm et al. (2018) [29] that constrained the masses of the TRAPPIST-1 planets, with precisions ranging from 8% to 17%.
We can also note that TTV can be used to characterize certain populations of exoplanets impractical for the radial velocity method (e.g. low mass objects) [12].

1.4 TRAPPIST-1

TRAPPIST-1 is the multiplanetary system we are focusing on in this work. It is composed of seven Earth-sized planets orbiting an Ultra Cool Dwarf (UCD) star. In this section, we will go through the discovery and properties of the system, with emphases on its scientific significance.

1.4.1 Discovery

2MASS was an all-sky astronomical survey of celestial sources observed in the near-infrared. Since Ultra-Cool Dwarfs (i.e. very low-mass stars and brown dwarfs with $T_{eff} < 2700K$ [36]) have a maximum intensity in the infrared, 2MASS was a golden opportunity to detect and study them. In 2000, this was done through J.E. Gizis et al.'s article [37] which aimed at completing the nearby stars census. Among the 60 objects studied was 2MASS J23062928-0502285, classified then as a M7.5[5] dwarf star.
In 2015, a monitoring of this star with the 60cm TRAPPIST (TRansiting Planets and PlanestIsimals Small Telescope) robotic telescope ([39], [40]), then with other telescopes, revealed several transit-like signals. After discarding non-planetary origin (false positive), Gillon et al. (2016) [41] attributed them to two Earth-sized exoplanets transiting their host with respective periods of 1.51 and 2.42 days. The planetary system was named TRAPPIST-1 after the telescope used at the time of this discovery, and the two planets were called TRAPPIST-1b and TRAPPIST-1c. Furthermore, two additional transits that they could not relate to b and c were suggested to be from a third planet, TRAPPIST-1d. However, these two signals were not observed continuously, hence eleven different periods could be associated with d.

After the article was submitted, further analysis of the second transit attributed to d revealed it to be caused not by one, but by at least two distinct objects (Fig.1.10). This discovery led to an intensive follow-up of the star with ground-based instruments and the Spitzer Space Telescope (20d-long nearly continuous monitoring, see Figure 1.11). As a consequence, Gillon et al. released a second article in 2017 [42], discarding the eleven potential periods for d, and proving the two transits were caused by different objects. Moreover, from the collected data, they identified four additional Earth-sized exoplanets named TRAPPIST-1d, e, f and g with orbital periods of 4.04, 6.06, 9.21 and 12.35 days respectively. Another planet called TRAPPIST-1h was announced, but its period could not be constrained as it was associated to a single transit signal. Its determination awaited R. Luger et al.'s study [43]. According to their analysis, as the six inner planets' periods are close to the ratios of small integers, they form a near-resonant chain. They suggested TRAPPIST-1h could be the seventh link of this chain, making them theoretically predict six potential periods. K2 mission then indicated that one of them, 18.77 days, was the correct one.

Within a few years, these three different papers enabled the scientific community to begin the characterization of this unique system of seven Earth-sized exoplanets orbiting an Ultra-Cool Dwarf. As TRAPPIST-1 became of major importance for the study of terrestrial exoplanets, many subsequent scientific studies aimed at constraining, for instance, the mass, the stability, or the atmospheric composition of the planets.

In the rest of this section, we will extend our current knowledge of the system.

[5] Posterior studies converged on a spectral type M8.0 ± 0.5, see [38].

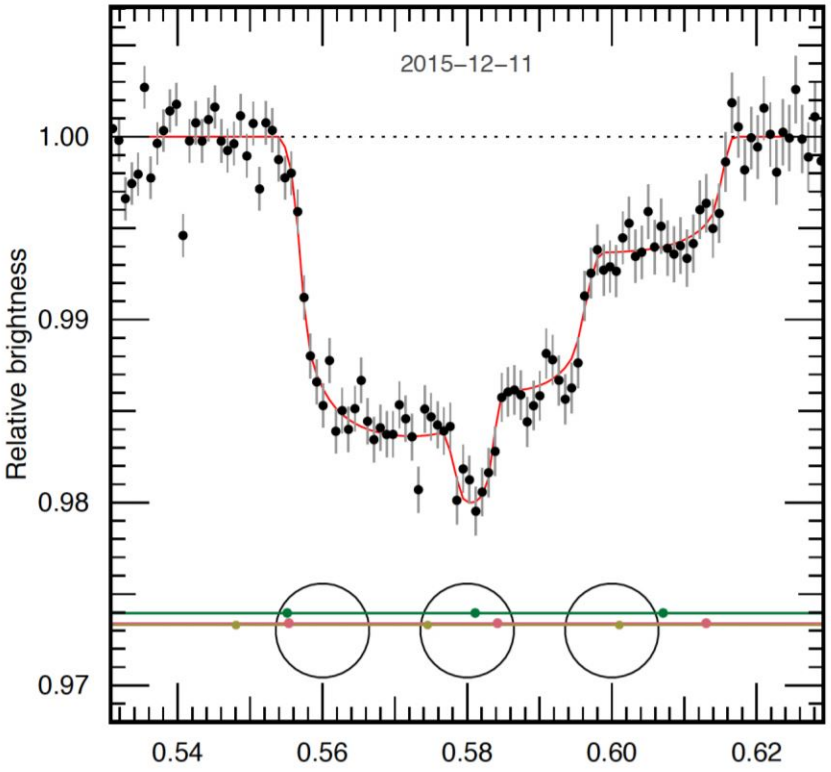

Figure 1.10: Plot of the photometric points with 1-σ error bars (black) extracted from VLT/HAWK-I data. The red line corresponds to the best-fit with a triple transit model. The hypothetical configurations of the different planets in front of the stellar disk are pictured below (c in red, e in yellow, f in green). [42]

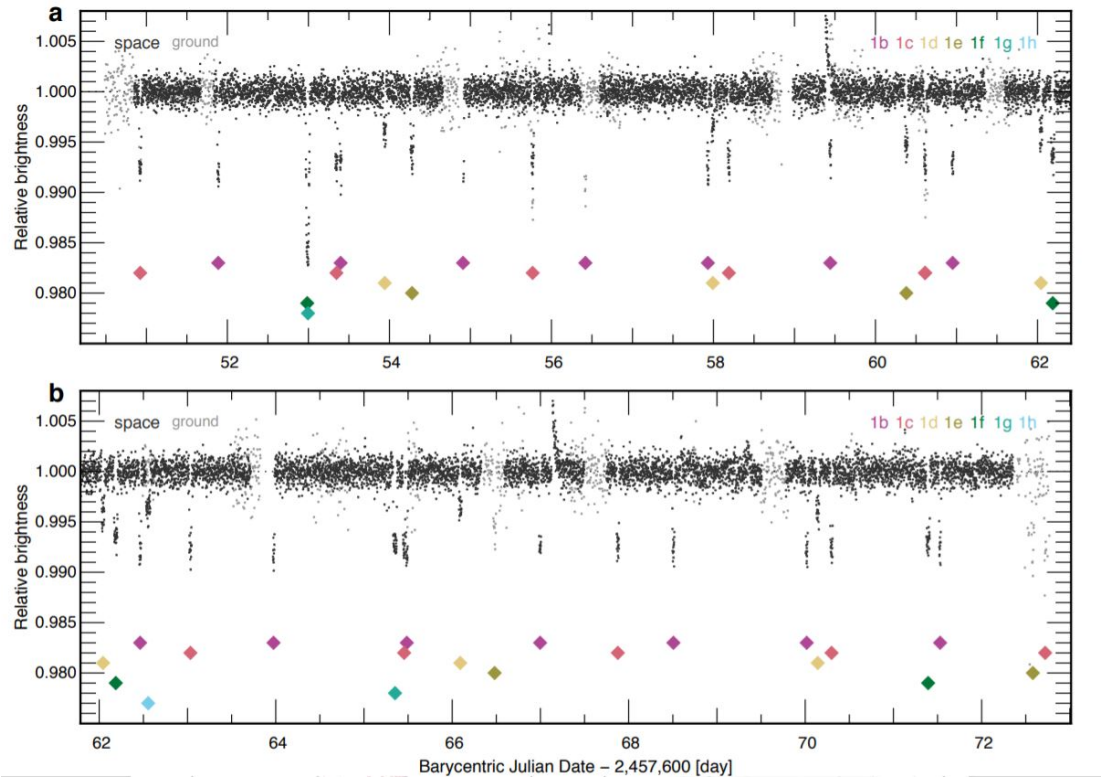

Figure 1.11: Plot of the photometric points obtained from ground-based observations (grey) and from the Spitzer's 20d-long nearly continuous monitoring (black) conducted between 19 Sep and 10 Oct 2016. The dips correspond to transits that can be associated to the different planets by measuring the transit shapes and their periodicities. [42]

1.4.2 Host star

As already specified TRAPPIST-1, or 2MASS J23062928-0502285, is an Ultra-Cool Dwarf (UCD) star with spectral type M8.0 ± 0.5 [38]. Being of low temperature (T_{eff} = 2547 ± 48), its emission peaks in the near-infrared. It is at a distance d = 12.14 ± 0.12pc from the Solar System [44]. Based upon measurements of its kinematics, photometric variability, and magnetic activity indicators, the dwarf was estimated to be 7.6 ± 2.2Gyr old [45]. The main stellar parameters of TRAPPIST-1 are indicated in Table 1.1. Those presented have been constrained from transit observations with Spitzer, combined to stellar evolution models [44].

Table 1.1: Stellar parameters of TRAPPIST-1 (from [46]).

Quantity	**Value**
Luminosity $L_\star$ ($L_\odot$)	0.000552 ± 0.000018
Radius $R_\star$ ($R_\odot$)	0.1234 ± 0.0033
Mass $M_\star$ ($M_\odot$)	0.0898 ± 0.0023
Density $\rho_\star$ ($\rho_\odot$)	47.98 ± 3.90
Effective temperature T_{eff} (K)	2520 ± 39
Metallicity [Fe/H] (dex)	0.0535 ± 0.088

In the context of discovery and characterization of transiting Earth-sized exoplanets, which is of major importance in our search for a potentially habitable world, Ultra-Cool Dwarfs like TRAPPIST-1 represent promising targets for a number of reasons.

An Earth-sized exoplanet transiting such a small star has a much deeper transit depth than Earth-Sun analogs, facilitating its detection even through ground-based observations [47]. More specifically, a terrestrial planet $R_p = R_\oplus$ transiting TRAPPIST-1 would have a depth ΔF = 5760 ppm while this value goes down to 84 ppm for the Sun (1.1). Moreover, the magnitude of terrestrial planets transmission spectra around UCDs can be high enough to assess the corresponding atmospheric composition, since $\delta \propto R_\star^{-2}$ (1.13). This feature is extremely important since the search for an extrasolar biosphere is passing by atmospheric characterization to detect biosignatures and key elements like H_2O, O_3 or O_2 [12]. It is worth highlighting that the low temperature of UCDs make their emission significant only in the infrared. Therefore, the signal to noise ratio at other wavelengths, like in the ultraviolet, is feeble, preventing possible detection of absorption lines in these domains[6]. Fortunately, most of the interesting molecular signatures are present in the IR domain.

Then, owing to their low luminosity, the habitable zone (HZ) is closer. Therefore, planets located inside the HZ of UCDs orbit closer to their hosts with shorter period orbits (~ days). As a consequence, their shadow cones are larger and their probabilities of transit are higher (1.11). As their orbital periods are shorter, a great number of transits may occur in less time and with shorter duration photometric monitoring [47]. For all the reasons we have just listed, only ~ 10 years of survey are required by the SPECULOOS project to fully explore the habitable zone of ~ 1600 targets [49], as we will see in Subsection 3.1.1.

[6]Here we speak about absorption lines in the atmosphere itself. In the context of an exoplanet with a potential exosphere of atomic hydrogen, an ultraviolet observation of the Lyman-alpha line is feasible. This has already been attempted for TRAPPIST-1 by Bourrier et al. [48].

Furthermore, it appears that low-mass M-dwarfs tend to have more short-period terrestrial planets than more massive stars [50]. They are also more frequent in the Galaxy than Sun-like stars. Indeed, UCD stars represent about 15% of the population of astronomical objects close to the Sun [51]. In total, they should house more terrestrial objects, which are detected and characterized more easily, especially in the habitable zone. It turns them into perfect and numerous targets for the study of Earth-sized exoplanets, in particular with Spitzer, the near-to-come JWST or upcoming giant ground-based telescopes like the ELT.

As we just saw, UCDs are promising targets in the study of terrestrial worlds, which is of major importance in the context of habitability study. However, do planets orbiting Ultra-Cool Dwarfs have a chance to be habitable ? In fact, M dwarfs are in average much more magnetically active than solar-type stars, resulting in strong quiescent luminosities in the extreme ultraviolet (EUV) and X-ray which are even amplified during their frequent flares [52]. Moreover, as planetary systems around M-dwarfs are compact and close to their hosts, the erosion by stellar wind is intensified. Regarding the TRAPPIST-1 system, it has been estimated that the stellar wind pressure experienced on the planets is between 10^3 and 10^5 times greater than on Earth [53]. Such an environment can significantly influence the composition and structure of an atmosphere, causing for instance ionization, atmospheric erosion [54] or desiccation [55]. Considering the impact on living organisms, opinions differ: some conclude life could survive, while others say it could make the surface uninhabitable ([56], [57], [58]). Some even argue that to a certain extent, the flaring activity could be beneficial for life as a minimum ultraviolet flux can allow the synthesis of ribonucleic acid (RNA) and trigger prebiotic chemistry [59].

As a conclusion, the effects could be diversified. Assessing the precise impact of the high-energy emissions would require a better understanding of the magnetic activity of M dwarfs in the present, but also in the past. Empirical observations have, as a matter of fact, shown that the activity of UCDs decreases with their age [45], hence their past activities could have impacted the planets significantly. For example, the young M8 type star 2M0837+2050 shows more frequent flares, three times more energetic in comparison with TRAPPIST-1 [60]. However, the number of M8 type stars studied so far is limited and it is complex to evaluate the current and past activities of TRAPPIST-1 and UCDs in general. The impact on the planets also depends on their intrinsic atmospheric properties and the strength of their potential magnetic fields, which are both poorly constrained [61]. The next generation of surveys and instruments, such as the JWST, will for sure shed light on whether or not these worlds could harbour life on their surface, notably by revealing if some of these planets can manage to keep an atmosphere despite their large received EUV and charged particles fluxes.

1.4.3 Planets

Since its initial detection in 2015, our knowledge of TRAPPIST-1 has greatly increased and this multiplanetary system is now one of the best – if not the best – constrained thanks to consecutive studies using transit, TTVs and transmission spectroscopy, among other methods. As represented on Figure 1.12, we can see that TRAPPIST-1 is very compact, with the seven planets in close-in orbit with their host. Indeed, they all orbit at semi-major axis $a \leq 0.0619 AU$ [29], while Mercury, in comparison, orbits the Sun at $a = 0.3870 AU$ [62]. But owing to the low luminosity of the star (Table 1.1), the planets do not receive an excessive amount of stellar

irradiation. Three of them, TRAPPIST-1e, f and g, are in fact located inside the habitable zone, hence could harbour stable liquid water on their surface, if we deal with Earth-like atmospheres [42].

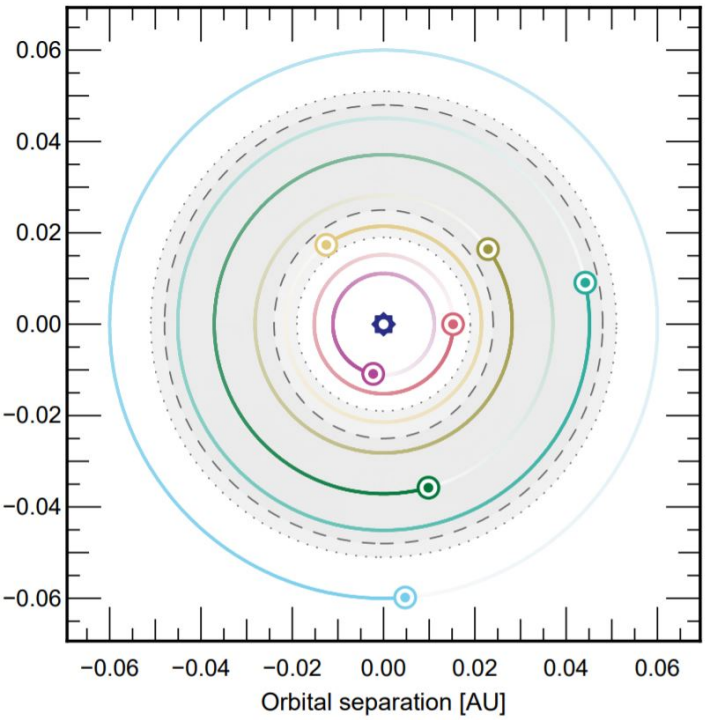

Figure 1.12: Representation of the TRAPPIST-1 system from above. The grey annulus shows the habitable zone and the dashed lines the alternative boundaries (conservative or optimistic [63]). [43]

As mentioned earlier, the seven planets form a compact near-resonant chain as their periods (1.51, 2.42, 4.04, 6.06, 9.21, 12.35 and 18.77 days) are close to the ratios of small integers ([42], [43]). In the same way as the Galilean satellites Io, Europa and Ganymede, each of the TRAPPIST-1 planets interact mostly with the pair of adjacent ones within a three-body Laplace resonance, linking every member of the chain [43]. This complex architecture, in addition to the poverty of material in the inner part of the protoplanetary disk of UCDs, suggest that the planets did not form *in situ*, but more likely at larger distance before slowly migrating inward in concert. As the disk's inner edge acted as a migration barrier, the planets would have piled up into the near-resonant chain observed nowadays ([41], [43], [64]).

Furthermore, the near-resonant chain increases the gravitational interactions between the planets, causing transit timing variations of several minutes [29]. These variations are significant enough to allow the use of the TTV to constrain the masses of the planets. This is of major importance since we cannot rely in this case on the radial velocity method, generally used for masses estimates. In fact, TRAPPIST-1 is too faint in the optical to achieve precise Doppler measurements with spectrographs like HARPS [65] or ESPRESSO [66]. Some new spectrographs operating in the near-IR should be able soon to reach RV precisions at the $1m/s$ level for nearby UCD stars like TRAPPIST-1 (e.g. SPIROU [67] or NIRPS [68]), but these precisions will still be too low to make possible a thorough characterization of the system dynamics and the planets masses. Even the mere detection of the seven planets via near-IR Doppler spectroscopy would require an intense and continuous follow-up from complementary longitude sites on Earth [67].

As a consequence, the TTV approach is currently the only avenue to precisely measure the masses of TRAPPIST-1 planets, and it is made possible by the strong interactions resulting of the resonant chain. The most recent mass estimates published in the literature are those of S.L. Grimm et al. [29] found in Table 1.2 along with other relevant parameters. This study significantly improved the precision we had so far concerning the masses of the planets, and subsequently, their density and internal composition were assessed in a more effective way, as described in Subsection 1.3.2. The scientists found that TRAPPIST-1c and e likely have rocky interiors while TRAPPIST-1b, d, f, g and h could bear volatile-rich layers in the form of a thick atmosphere, ocean, or ice envelope. These results are consistent with the hypothesis described previously stating the planets most likely formed in the outer part of the protoplanetary disk, rich in volatile materials, before migrating inward.

This compact architecture makes the planets experience strong tidal forces as well. These interactions should have synchronized their rotation and orbital periods in such a way that one side of the planet permanently faces the host star (tidal locking) [41]. This could have a dramatic effect on the habitability if the atmosphere does not redistribute efficiently the heat between the hot day side and the cold night side [69]. Moreover, tidal forces tend to decrease the orbital eccentricity (tidal circularisation). During this process, orbital energy is converted into heat that dissipates in their interiors. The tidal heating decreases as the orbit circularizes, and stops when $e = 0$. For a single planet orbiting close to its star the circularisation is fast, whereas in a multiplanetary system experiencing resonance motions like TRAPPIST-1, the gravitational perturbations help maintain non-zero eccentricities, hence the tidal heating ([43], [70]). Similarly, Jupiter's moon Io keeps a tidal heat flux at about $2 - 4W/m^2$ [71]. For TRAPPIST-1 planets, assuming Earth-like tidal dissipation, b may have a flux larger than Io, c to e between values similar to Earth and Io, and f to h smaller than the Earth [43]. Tidal heating can have a significant impact on the habitability of a planet: negative if it results in an excessive volcanic activity like on Io; positive if it increases the outgassing of volatiles from the mantle, offering a replenishment mechanism that counteracts atmospheric erosion due to the star magnetic activity [70]. It can also have a positive impact for bodies with a thick layer of ice, as it is potentially the case for TRAPPIST-1b, d, f, g and h [29]. The tidal heating could be sufficient to have a part of the ice layer melt and a subsurface water ocean that may house living organisms created [72].

In regard to their atmospheres, the Hubble Space Telescope's observations ruled out a cloud-free hydrogen-dominated atmosphere for six of the seven planets. Being a powerful greenhouse gas, a significant amount of hydrogen in an atmosphere could either have a positive impact on the habitability of the outer planets, when preventing the atmospheres to freeze, or a negative one on the inner planets as it is significantly increasing the surface temperature, preventing water to remain in liquid state. As stable liquid water is a key element in our search for living organisms, the fact that hydrogen-dominated atmosphere has been dismissed for the inner planets increases their potential habitability ([73], [74], [75]). However, the composition and structure remain unconstrained as their study is beyond the reach of current instruments. Nevertheless, preliminary studies demonstrated that the JWST would be perfectly capable of covering more in depth their atmospheric properties [24]. In the following years, it is therefore expected that the JWST survey reveals the presence, composition and structure of the atmospheres around the TRAPPIST-1 planets.

Additional TTV analysis, like the one Agol et al. [76] are currently preparing, will help constrain further their densities and interior compositions, and gain a better insight about their formation history and tidal dissipation. It will also possibly uncover a new exoplanet in the system, allowing to explain the orphan transit-like structures found among Spitzer data [46].

Table 1.2: Parameters of the seven planets of TRAPPIST-1.

Planet	**b**	**c**	**d**	**e**	**f**	**g**	**h**
From E.Ducrot et al. (2020) [46]							
Period (days)	1.51088432 ±0.00000015	2.42179346 ±0.00000023	4.04978035 ±0.00000266	6.09956479 ±0.00000178	9.20659399 ±0.00000212	12.3535557 ±0.00000341	18.7672745 ±0.00001876
Mid-transit time T_0 - 2,450,000 (BJD_{TDB})	7322.514193 ±0.0000030	7282.8113871 ±0.0000038	7670.1463014 ±0.0000184	7660.3676621 ±0.0000143	7671.3737299 ±0.0000157	7665.3628439 ±0.0000206	7662.5741486 ±0.0000913
Transit depth at 3.6μm (%)	0.7209 ±0.0067	0.721 ±0.014	0.351 ±0.016	0.491 ±0.011	0.655 ±0.019	0.724 ±0.024	0.313 ±0.027
Impact parameter ($R_\star$)	$0.254^{+0.110}_{-0.085}$	$0.254^{+0.110}_{-0.087}$	$0.235^{+0.120}_{-0.094}$	$0.299^{+0.085}_{-0.072}$	0.391 ± 0.056	0.430 ± 0.049	0.448 ± 0.054
Transit duration (min)	36.309 ± 0.093	42.42 ± 0.12	49.37 ± 0.32	56.31 ± 0.25	63.28 ± 0.31	69.10 ± 0.36	76.28 ± 0.81
$R_p/R_\star$ at 3.6μm	0.084903 ±0.00040	0.08495 ±0.00086	0.0593 ±0.0013	00.07009 ±0.00075	0.0809 ±0.0013	0.0851 ±0.0014	0.0559 ±0.0025
Inclination (°)	89.28 ± 0.32	89.47 ± 0.24	89.65 ± 0.15	89.663 ± 0.092	89.666 ± 0.059	89.698 ± 0.044	89.763 ± 0.037
Semi-major axis (10^{-3} AU)	$11.534^{+0.099}_{-0.092}$	$15.79^{+0.14}_{-0.13}$	$22.26^{+0.19}_{-0.18}$	$29.24^{+0.25}_{-0.23}$	$38.7740^{+0.33}_{-0.31}$	$46.81528^{+0.40}_{-0.37}$	$61.8656^{+0.53}_{-0.49}$
Scale parameter $a/R_\star$	$20.13^{+0.46}_{-0.55}$	$27.57^{+0.62}_{-0.76}$	$38.85^{+0.88}_{-1.1}$	$51.0^{+1.2}_{-1.4}$	$67.1^{+1.15}_{-1.9}$	$81.7^{+1.8}_{-2.3}$	$107.9^{+2.4}_{-3.0}$
Irradiation ($S_\odot$)	4.15 ± 0.16	2.211 ± 0.085	1.114 ± 0.043	0.645 ± 0.025	0.373 ± 0.014	0.252 ± 0.0097	0.144 ± 0.0055
Equilibrium temperature[1] (K)	397.6 ± 3.8	339.7 ± 3.3	286.2 ± 2.8	249.7 ± 2.4	217.7 ± 2.1	197.3 ± 1.9	171.7 ± 1.7
From S.L.Grimm et al. (2018) [29]							
Eccentricity	0.00622 ±0.00304	0.00654 ±0.00188	0.00837 ±0.00093	0.00510 ±0.00058	0.01007 ±0.00068	0.00208 ±0.00058	0.00567 ±0.00121
Argument of periapsis (°)	336.86 ± 34.24	282.45 ± 17.10	−8.73 ± 6.17	108.37 ± 8.47	368.81 ± 3.11	191.34 ± 13.83	338.92 ± 9.66
Radius ($R_\oplus$)	$1.121^{+0.031}_{-0.032}$	$1.095^{+0.030}_{-0.031}$	$0.784^{+0.023}_{-0.023}$	$0.910^{+0.026}_{-0.027}$	$1.046^{+0.029}_{-0.030}$	$1.148^{+0.032}_{-0.033}$	$0.773^{+0.026}_{-0.027}$
Mass ($M_\oplus$)	$1.017^{+0.154}_{-0.143}$	$1.156^{+0.142}_{-0.131}$	$0.297^{+0.039}_{-0.035}$	$0.772^{+0.079}_{-0.075}$	$0.934^{+0.080}_{-0.078}$	$1.148^{+0.098}_{-0.095}$	$0.331^{+0.056}_{-0.049}$
Density ($\rho_\oplus$)	$0.726^{+0.092}_{-0.091}$	$0.883^{+0.083}_{-0.078}$	$0.616^{+0.067}_{-0.062}$	$1.024^{+0.076}_{-0.070}$	$0.816^{+0.038}_{-0.036}$	$0.759^{+0.034}_{-0.033}$	$0.719^{+0.117}_{-0.102}$

[1] assuming a null Bond albedo.

CHAPTER 2

Goal of this Master thesis

As we have seen throughout Chapter 1, TRAPPIST-1 is an exceptional multiplanetary system that will be at the center of many studies and probably major breakthroughs in the following years. Notably, we saw that its architecture creates important gravitational interactions between the planets, turning it into a perfect target for the analysis of transit timing variations. From this analysis, we can learn more about its dynamics and constrain the masses of its planets. However, retrieving these pieces of information from timing variations is a challenging N-body inversion problem, and it requires a significant amount of timing data, see for example S.L.Grimm et al. (2018) [29] who used a set of 284 individual transit timings for their study, or the upcoming work of Agol et al. (2020) [76] that used 447.

In this context, the goal of this Master thesis is to provide transit timing data of the TRAPPIST-1 system that will be used to support the next generation of TTV study designed to constrain even more accurately the mass and density of the seven planets. These data could for instance be combined with data from the Spitzer Exploration Program Red Worlds, recently analyzed by E. Ducrot et al. (2020) [46]. They captured 188 transits of TRAPPIST-1 among more than 1000 hours of observation between February 2016 and October 2019. The accurate results gathered from the future TTV analyses will be a key element to pave the way for subsequent studies focusing for example on their tidal dissipation, directly dependent on their internal composition, their habitability, and formation history from the protoplanetary disk.

To provide new transit timings, the TRAPPIST-1 system was observed with the telescope Io from the SPECULOOS Southern Observatory (SSO) during the year 2019, more precisely between May and December in accordance with the observability of the target from Chile, where operate the SSO telescopes. Then, the obtained raw images were calibrated and the stellar fluxes measured by aperture photometry, using the autonomous pipeline specifically built for SSO observations. Next, I performed differential photometry with SPECPHOT, a photometric Python package mainly developed by L. Garcia from the University of Liège. As a result, accurate lightcurves came out of the observations, which were then subjected to a Markov Chain Monte Carlo (MCMC) simulation following two approaches: an individual one to gather the timings, best-fit of the lightcurves, and study transient phenomena such as flares; and a global one by grouping the lightcurves planet by planet to achieve the best constraints on the system parameters.

In total, I analyzed and computed the timing data of 47 transits from the TRAPPIST-1 planets. The different results of this survey will be presented in Chapter 4.

CHAPTER 3

Data acquisition and analysis

In this chapter will be detailed the acquisition, reduction, and analysis, of the TRAPPIST-1 planets' transit lightcurves collected during the observational campaign with SPECULOOS-South between May and December 2019. Some context will first be provided about the SPECULOOS Observatories and how they were used for my observations. Then, the reduction of my data with the SSO pipeline and SPECPHOT will be discussed. I will conclude this chapter with a description of the lightcurve analysis done with the Markov Chain Monte Carlo (MCMC) method.

3.1 Observation

3.1.1 SPECULOOS project

As my observations were made using SPECULOOS-South, I will start this section by going through the SPECULOOS project, its telescopes, and its objectives.

Figure 3.1: The four 1m robotic telescopes of the SPECULOOS Southern Observatory (SSO). From left to right: Callisto, Ganymede, Europa and Io. [77]

SPECULOOS, for **S**earch for habitable **P**lanets **EC**lipsing **UL**tra-c**OO**l **S**tars, is a project that aims at the detection of Earth-sized exoplanets in the habitable zone of nearby Ultra-Cool Stars (spectral type M7 or latter). Its main objective is to pave the way for further atmospheric characterization and potential biosignature detection with the future JWST and Extremely Large Telescope (ELT). It is based on a network of six 1m robotic telescopes: the four telescopes of the SPECULOOS Southern Observatory (SSO) in Chile, the telescope of the SPECULOOS Northern Observatory (SNO) in Tenerife, and the SAINT-EX telescope in Mexico. While not being parts of the SPECULOOS network, the two 60cm robotic telescopes TRAPPIST devote a fraction of their observational time to the project. In fact, they even paved its way as they demonstrated with the TRAPPIST-UCDTS prototype survey [47] and the detection of the TRAPPIST-1 system that the study of nearby UCD stars can be achieved with a sufficient photometric precision by using small ground-based telescopes [49]. They are twin robotic telescopes – TRAPPIST-South is installed at the ESO La Silla Observatory in Chile and TRAPPIST-North operates from the Oukaïmeden Observatory in Morocco [77].

The SPECULOOS project is a scientific collaboration between the University of Liège (Belgium), the Massachusetts Institute of Technology (USA), the University of Bern (Switzerland), the Canary Islands Institute of Astrophysics (Spain), the University of Cambridge and the University of Birmingham (England). SSO has operated since January 2019 and is composed of four identical robotic telescopes named after the Galilean moons of Jupiter - Io, Europa, Ganymede, and Callisto (Fig.3.1). SNO was inaugurated more recently in June 2019 and is currently based on one telescope, Artémis, which is a SSO's twin. This is also the case of the SAINT-EX telescope whose operations at San Pedro Martir Observartory (Mexico) started in summer 2019. They are Ritchey-Chretien telescopes with a combined focal ratio F/8 for the system of the 1-m diameter primary and 28-cm diameter secondary mirrors. Each of them is associated with a robotic equatorial mount and a camera with a 2K×2K CCD detector of pixel size 13.5 μm and scale 0.35″/pixel leading to a field of view of $12' \times 12'$. The camera is cooled (Peltier effect) to minimize its dark current. The cooling can go down to −100°C but it generally operates at −60°C to reach a dark current of $\sim 0.1 e^{-}/s$/pixel. The CCD detector has a good sensitivity from the near-UV (~ 350 nm) to the near-IR (~ 950 nm). However, as SPECULOOS focuses on UCD that peaks in the infrared, there is a CCD window that maximizes the transmissivity in the IR, while blocking everything below ~ 400 nm. In addition, each camera comes with a filter wheel so observations with SPECULOOS telescopes can be conducted with the following set of filters: Sloan -g', -r', -i', -z', $I+z$ and blue-blocking [49]. Their transmission curves are shown in Figure 3.2.

The target list of this project consists in 1657 known UCD stars all located within 40pc of the Solar System. They are divided into three programs [78]. The first contains a census of targets for which the JWST should be able to perform a thorough atmospheric characterization of Earth-sized planets. It is made of 365 stars. Program 2 is dedicated to study the overlap region between the targets observable by SPECULOOS and TESS (Transiting Exoplanet Survey Satellite). Indeed, TESS is examining brighter stars and its detection potential falls down at spectral type around M5, which corresponds to the earlier UCDs observable with SPECULOOS. It includes 171 targets all with spectral types between M5 and M6.5V. The third program is made of the 1121 targets not covered by the first two programs, its results will help building a statistical database related to planets around UCDs.

Each target will be observed sufficiently to explore its habitable zone, as it is the goal of the

survey. The coverage represents 200 hours for the first program and 100 hours for the second and third. This difference of observation time is explained by the highest scientific importance of planets potentially found by program 1.

The SPECULOOS survey started in 2017 and has until now (June 2020) observed about 10% of the targets with more than 50 hours [78]. It is important to note that because they are spread all over the sky, each target is monitored individually and it requires telescopes settled in both hemispheres. Moreover, the monitoring has to be done continuously during the night to not miss any potential transits as their duration is small (~ 15 minutes for a planet with $P < 1d$). By taking into account the six telescopes of the SPECULOOS network and potential lost nights due to bad conditions (e.g. weather), it would require ~ 10 years to complete the HZ monitoring of the targets [49].

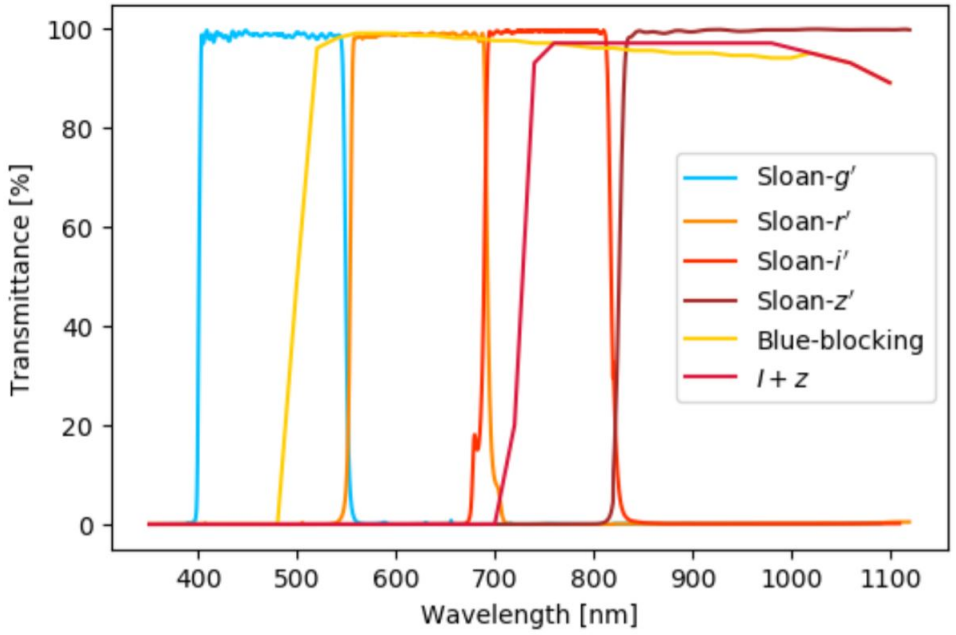

Figure 3.2: Transmission curves of the broad-band filters available on the robotic telescopes of the SPECULOOS Observatories. [49]

3.1.2 Data acquisition

Since they were developed to monitor UCDs and their transiting planets, SPECULOOS telescopes are perfectly suitable for a follow-up on the TRAPPIST-1 system. It is what we have done in 2019 with SSO/Io. The observations extended from May to December because of the ideal position of the star in the sky during this time interval. Indeed, to be observed properly, the star needs to be visible at night from the observatory and needs to be at a sufficient altitude in the sky to decrease the airmass, hence the perturbations and extinction due to the atmosphere. With a right ascension of $23h\ 06m\ 29.2s$ and a declination of $-05°\ 02'\ 28.59''$ ([79], J2000 coordinates), the star satisfied the criteria from SPECULOOS-South between May and December (Fig.3.3).

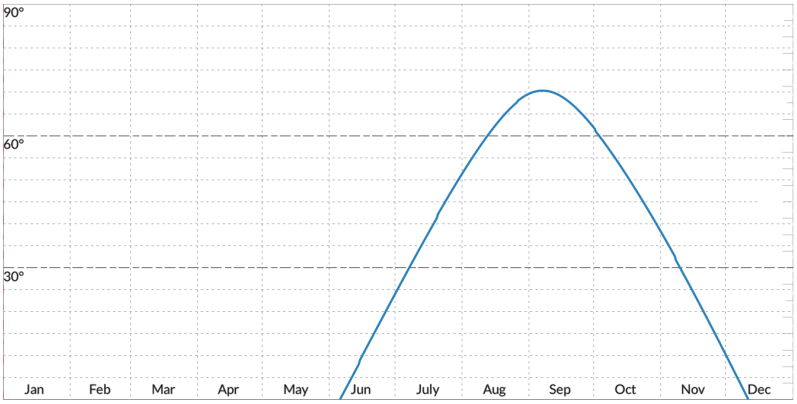

Figure 3.3: Altitude of TRAPPIST-1 at local midnight throughout the year from the SSO. In May, it appeared after midnight but went sufficiently high in the sky to be observable. [80]

Each transit event happening between May and December 2019 was predicted with an approximate mid-transit time. It could then be observed by the telescope if the following conditions were met:

- the event had to occur at night and at high altitude in the sky to decrease atmospheric perturbations (typically 25° above the horizon);
- the moon should not be too close to the star (distance in the sky > 30°);
- the weather conditions needed to be propitious, i.e. no cloud covers and low humidity to achieve precise measurements, and a low wind speed to avoid damaging the instruments (automatic closing when $v_{wind} > 18m/s$).

All the observations were made with the same telescope to prevent a potential offset on the lightcurves due to intrinsic instrumental disparities. If the conditions were adapted[1], the observation extended before and after the predicted event time to, (1) properly distinguish the eclipse ingress and egress, (2) have enough no-transit time for lightcurve normalization purpose, and (3) not miss the transit in case TTVs had significantly changed the timing. Each image was taken with an exposure time of 23 seconds as calculated with SSO's exposure time calculator. TRAPPIST-1 is, as a matter of fact, a relatively bright UCD star (J-band magnitude of 11.35 [81]), hence a longer exposure time could quickly saturate the CCD of Io. Regarding the filter, we selected the $I + z$ as it offers a high transmittance (Fig.3.2) in the wavelength where UCD stars emit the most (i.e between 700nm and 1000nm). The blue-blocking could also be used but the transmittance increases from 500nm. Since UCDs do not emit significantly below 700nm, this filter would just intensify the background noise in the data. The Sloan -i' also has an acceptable transmittance in the near-infrared but we lose some signals since its transmissivity decreases around 800nm. At the end of the night, all raw images recorded by Io were automatically uploaded to the online ESO archive and downloaded to a server at the University of Cambridge (UK).

In total, I observed 47 transits from the TRAPPIST-1 planets spread in 40 observation nights between May and December 2019. In these transits, 20 are from b, 11 from c, 9 from d, 3 from e, 1 from f and g, and 2 from h. The list of the observation dates with the concerned planet(s) can be found in Table 3.1.

[1]For instance, if the transit occurred at the beginning of the night, we could not extend the observation before because it would be during daytime.

Table 3.1: Observation dates of TRAPPIST-1 between May and Dec 2019 along with some remarks.

UT date	**Planet(s) in the observation**	**Remark**
2019/05/21	b	×
2019/05/22	d	×
2019/05/23	c	×
2019/05/24	b	×
2019/07/04	b	×
2019/07/10	b ; f	×
2019/07/13	c ; b	blended transits
2019/07/16	b	×
2019/07/28	b	×
2019/07/30	d ; c ; h	bad weather + d and c blended
2019/07/31	b	×
2019/08/03	d ; b	No egress of b - end of the night
2019/08/11	c ; d	blended transits
2019/08/28	c	flare
2019/09/02	c	×
2019/09/04	b	×
2019/09/10	b	×
2019/09/16	b	×
2019/09/19	c	×
2019/09/25	b	×
2019/10/02	d	only egress - beginning of the night
2019/10/06	c	×
2019/10/07	d	bad weather – clouds
2019/10/18	c	×
2019/10/19	d	×
2019/10/20	e	×
2019/10/21	b	no ingress - beginning of the night
2019/10/23	d	×
2019/10/24	b	×
2019/10/26	e	×
2019/10/27	b	×
2019/10/30	b	flare
2019/11/01	h	×
2019/11/02	g ; b	bad weather – high humidity
2019/11/04	c	×
2019/11/05	b	×
2019/11/14	b	×
2019/11/21	c	×
2019/12/20	e	×
2019/12/27	d	only egress - beginning of the night

3.2 Data processing

The raw data emerging from the observational campaign need to be processed before being analyzed. This task is divided in two parts: using an autonomous pipeline specifically built for SSO observations and using a Python package designed to retrieve and analyze photometry from full frame astronomical images, specphot.

3.2.1 SSO pipeline

Due to the consequent amount of data gathered by the SSO telescopes and the photometric challenges specific to this survey, an autonomous pipeline dedicated to SSO images has been designed (developed at the University of Cambridge). The main steps are [82], (1) image calibration, (2) aperture photometry, (3) differential photometry, and (4) water vapor correction. To process the data of this Master thesis, I used steps 1 and 2 of the pipeline before doing the differential photometry with specphot. These steps will be detailed in this section.

Even with high quality instruments, collected images are affected by various instrumental effects that should be corrected to obtain accurate photometric measurements. It is done through image calibration. Every night, we take three types of calibration images called bias, dark and flat.[82].

– **Dark**: a CCD detector works with the excitation of bound electrons by photons coming from observed sources. The problem is that they can also be excited thermally, which creates an additional signal on the data called dark current. The amplitude of this signal can be greatly reduced by cooling down the detectors, but it is not completely damped. Therefore, we collect dark frames which are taken at dawn once the telescope dome is closed, with no light striking the array, so that most of the measured electrons are those generated by thermal excitation. As this process is random, several dark images are collected and averaged into a 'master dark'. Since cosmic rays can still interact with the detector when the dome is closed, we produce the master dark image with a sigma-clip process that keeps only the values close to the median. The resulting master dark is then subtracted from all the raw images.

– **Flat**: The pixels composing a CCD slightly differ from each other in their sensitivity due to inherent manufacturing disparities or the presence of dusts on the camera and filters which shade the pixels behind. To get accurate photometric measurements, it is necessary to correct this effect with flat-field frames captured under the uniform twilight sky at both dusk and dawn with the filter used during the observation since flat-fields are filter-dependent. The response of the CCD detector to this uniform light source will be non uniform due to the pixel sensitivity variation. The flat-fields are averaged to create a master flat-field frame using sigma clipping. Each raw image is then divided by it to reduce the sensitivity variations.

– **Bias**: When the camera is read and the electron signal turned into digital units, a pixel-dependent offset is added to the measured counts. In order to rectify this effect, bias frames are gathered with a zero second exposure time at dawn once the telescope dome is closed. Here, again, several frames are taken and averaged using sigma clipping. The master bias is then subtracted from the raw images.

Once the science images have been calibrated with dark and bias subtraction and flat-field division, they are ready for photometric measurements done through aperture photometry.

Aperture photometry is a way to retrieve the total flux of the sources detected in an image by defining a two-dimensional area centered on each object, called measuring aperture. Its shape is usually a circle, particularly when we consider stars in an image like it is the case here. However, in case of extended structures like galaxies and nebulae, the shape can be different, e.g. an ellipse. After the aperture is defined, we calculate the source flux by summing the counts on the pixels located within the area and by subtracting the sky background contribution [83]. The challenge with this technique comes from the selection of an aperture size. If it is too small, we lose some source signal and the signal to noise ratio (S/N) decreases. But if it is too extended, the S/N also decreases because the noise encompassed in the aperture increases [84]. It is therefore required to consciously choose the aperture size. In my case, the SSO pipeline detects every source and measures the fluxes in every science image with 13 different aperture sizes [82].

3.2.2 SPECPHOT

SPECPHOT is a Python package designed to perform stellar photometry on a set of observations, mainly based on an Astropy package called photutils [85] and currently under development at the University of Liège by the PhD student L. Garcia. It can accomplish various tasks including image calibration, aperture and differential photometry, lightcurve visualization and detrending. As opposed to the automatic SSO pipeline which is handling a great amount of images without any human intervention, SPECPHOT gives a manual control on the data processing, allowing the user to perform finely tuned analysis for a specific set of observations. It is motivated by this reason that I pursued the processing of the data with this tool[2].

As SPECPHOT was first designed for the SPECULOOS survey, it offers an automatic way to download all the data from their storage, on the server of the University of Cambridge. This is done with a function that takes in argument the different characteristics of the considered set of observations. In my case, specifying the target and the year is sufficient to gather the data of all the transits of TRAPPIST-1 observed between May and December 2019. After the download is complete, SPECPHOT stores the information on the workstation in two files per observation. The first one simply consists in a stack image (Fig.3.4) while the other contains all the observation data such as the photometry for all stars in every image at the 13 apertures and the value of the different systematics. As they are now available on the user computer, they can be opened, modified and visualized easily.

Afterwards, we have to apply differential photometry to the data by selecting in the image one or several other stars, called *comparison stars*, and representing the signal of the target as the difference between its magnitude and the comparison star's one, or a combination if there are several. By doing so, most of the flux variations not intrinsic to the target are removed, including those due to atmospheric turbulence and clouds passing in the line of sight. It is particularly convenient when it comes to measure small stellar flux variations from ground-based observations, like it is the case for the SPECULOOS transit survey. The comparison stars need to be close to the target to ensure that they are affected by the same atmospheric perturbations. Moreover, they should not be variable stars themselves [83]. With SPECPHOT, a specialized function selects the optimal comparison stars, applies the differential photometry on the target's lightcurve with the 13 apertures and normalizes it so that the mean flux outside

[2] I could also have used SPECPHOT from the beginning with the image calibration.

of the transit signal equals to one. The optimal comparison stars are selected following notably the algorithm detailed in Broeg et al. (2005) [86].

The final aperture of a given observation is then chosen by keeping the one that minimizes the *average spread* of the lightcurve, defined as the average out-of-transit standard deviation in five-minute bins [82].

This method resulted in 40 differential lightcurves of TRAPPIST-1, each corresponding to a given observation night (Table 3.1).

Figure 3.4: Stack image of the observation of a transit of TRAPPIST-1b on 15 Jul 2019.

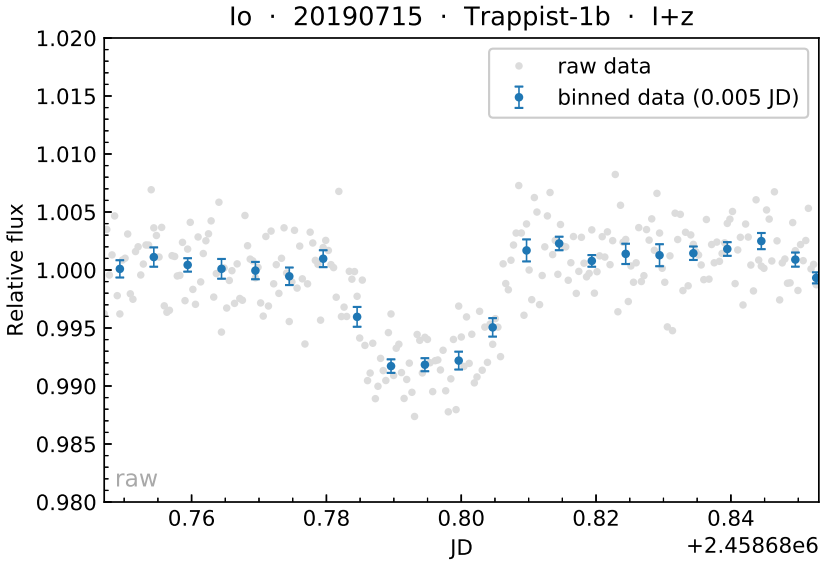

Figure 3.5: Final differential lightcurve of TRAPPIST-1 for the observation on 15 Jul 2019.

3.3 Data analysis

Once the data processed, I subjected them to a Markov Chain Monte Carlo analysis using a code written by M. Gillon [87]. With my lightcurves as input, this code enabled me to derive the parameters of the planets and their host star, along with their corresponding errors. In this section, I give a brief introduction to the MCMC analysis as a complete description would be beyond the scope of this work. I then describe more specifically how I used it with the dataset presented in this Master thesis. The results of this analysis are given in Chapter 4.

3.3.1 The Markov Chain Monte Carlo method

The Markov Chain Monte Carlo method is a stochastic simulations algorithm based on Bayesian statistics whose goal is to derive the posterior probability distribution functions of a set of parameters of interest given an assumed model and some input data. It is well suited for exoplanet data analysis where we deal with extensive parameter spaces, particularly with multiplanetary systems like TRAPPIST-1. The algorithm is conditioned by, (1) a dataset represented in my case by the photometric points of the lightcurves, and (2) a model, here the eclipse model of Mandel & Agol (2002) [88] multiplied by a baseline model that aims to represent the effect of other astrophysical and instrumental mechanisms able to produce photometric variations, such as airmass variation during an observation [87]. The MCMC links two concepts: the Monte Carlo and the Markov Chain. The Monte Carlo describes the process of sampling a distribution only by drawing random samples from it, generally because it is too complex for a purely analytical representation. As an example, under this approach one would find the mean of a given distribution by taking the mean of a number of random samples taken from it rather than from an analytical equation. The Markov chain part of the MCMC implies that the random samples are generated through a sequential process where each sample is used to generate the next one. Therefore, a new sample is only linked to the one preceding it and the algorithm keeps no memory of all the past samples. This memoryless property in a random process is referred to as *Markov* property, hence the name given to the chain. By combining these two concepts we obtain the Markov Chain Monte Carlo method which can be tuned to converge to the posterior probability distribution functions of a model's parameters [89].

In practice, during the MCMC simulation some parameters that we call jump parameters are randomly perturbed. This perturbation changes their value, making their parameter space exploration possible. Generally the jump parameters are the following [87]:

- the stellar mass $M_\star$;
- the stellar radius $R_\star$;
- The stellar effective temperature T_{eff};
- The metallicity [Fe/H];
- the combinations $c_1 = 2 \times u_1 + u_2$ and $c_2 = u_1 - 2 \times u_2$ where $u_1 = 0.8846 \pm 0.14$ and $u_2 = 0.05 \pm 0.14$ are the quadratic limb darkening coefficients for TRAPPIST-1 with the $I + z$ filter interpolated from Claret et al. (2012) [90];
- the transit depth dF;
- the impact parameter b;

- the orbital period P;
- the transit duration W;
- the time of inferior conjunction T_0, i.e. when the distance on the plane of the sky between the center of the star's disk and the center of the planet's disk is minimal (with the planet closer to the Earth than the star). It corresponds to the mid-transit time for a circular orbit [11].

The jump parameters dF, W, b, P and T_0 are taken for each planet appearing in the lightcurve. From the new drawn values, we derive a model and the other physical parameters of the system (e.g. planetary radius) according to our baseline and the eclipse model [88]. Afterwards, the goal is to quantify the relative probability of the step.

In Bayesian statistics, the probability of an event is interpreted as a degree of belief, which depends on our opinion on its value prior to the analysis, but also on newly observed data. Formally, this approach uses the new perceived data **D** about a set of parameters to update the prior beliefs **I** to posterior beliefs. We express it mathematically with the Bayes' theorem [91]:

$$p(M|D,I) = \frac{p(M|I)p(D|M,I)}{p(D|I)} \tag{3.1}$$

Where $p(M|D,I)$ is the posterior probability that the model M is true, considering the data D and the prior state of beliefs I, $p(M|I)$ is the prior probability, $p(D|M,I)$ is the likelihood that quantifies the agreement between the model and the data, and $p(D|I)$ is a normalization factor. The prior beliefs on a parameter are given to the MCMC as a probability distribution function. In the code used for this work, it is possible to fix either a uniform or a normal prior. In the first case, no value is more probable than another one and the exploration of the parameter space is free. Whereas in the second case, the given normal distribution $\mathcal{N}(\mu,\sigma^2)$ defines a high probability region around μ, whose size is related to the standard deviation σ. As a consequence, when the MCMC draws a value of the parameter in this region, the prior probability is higher, and the same applies for the posterior probability (see the Bayes' theorem). As we will see after, this forces the algorithm to spend more time in this region, which constrains the exploration of the parameter space[3]. For instance, I assumed in my analyses a prior $0.0898 \pm 0.0023 M_\odot$ on the stellar mass, well constrained by E. Ducrot et al. (2020) [46], which the algorithm interprets as a normal distribution $\mathcal{N}(0.0898, 0.0023^2)$ $M_\odot$.
It is worth mentioning that with these distributions can be associated physical limits, for example negative values are not allowed for dF, W, b, P, and T_0, and b should be inferior to $a/R_\star$ (1.8).

At each new step i, the posterior probability P_i is computed from the prior probability and the likelihood function. We then compare it to the posterior probability P_{i-1} acquired at the previous step[4] using the Metropolis-Hastings algorithm [92]. It works as follows:

- if $P_i > P_{i-1}$, step i is better and accepted, the chain continues from there;

[3] The exploration constraint is even more important as the given σ is small, since it defines the size of the high probability region of the Gaussian.

[4] Only the previous step is considered, in agreement with the Markov property of the chain.

- if $P_i < P_{i-1}$, the MCMC draws a random number u between 0 and 1. If $P_i/P_{i-1} > u$, step i is accepted, but if $P_i/P_{i-1} < u$, then step i is rejected and the chain goes back to the step $i-1$ to continue the chain.

Having such a rule, the simulation ends up converging in high posterior probability region while still having a sufficient flexibility to explore the parameter space without getting stuck in local maxima. The MCMC keeps exploring step by step following this process. Each time a certain value of a parameter is drawn, it increases the statistical weight of this value which will be used at the end of the chain to build the posterior probability distribution function (PDF) of each parameter. Since the Metropolis-Hastings algorithm makes the MCMC converge in high probability region, the more likely values are kept more than the others hence their statistical weight increases. When it reaches the number of steps limited by the user, the MCMC stops and discards the first unstable steps of the chain that did not already converge, so that they do not affect the posterior PDFs. We call this removed fraction the burn-in phase, and it represents 20% of the chain size in my case. The algorithm then outputs several information, especially the median and $1-\sigma$ deviation of the parameters' PDF. The best-fit of the lightcurve is obtained as a by-product from the model that got the highest posterior probability during the chain.

3.3.2 Analysis of the dataset

Before analyzing my 40 lightcurves, I converted the time unit. SPECPHOT works indeed in julian date with the coordinated universal time standard (UTC), denoted JD_{UTC}, not convenient when dealing with astronomical events [93]. For instance, due to the finite speed of light, an event coming from a specific source can be detected at different times depending on the position of the Earth on its orbit. Since the semi-major axis of our planet is $1AU$, an event can be early or delayed up to $1AU/c$ ($\sim$ 8.3 minutes). Also, due to relativistic effects, time passes differently on moving objects. To correct these, we must convert the time in BJD_{TDB}. In BJD (barycentric julian date) the reference frame is not the Earth but the Solar System's center of mass. TDB stands for barycentric dynamical time and is a time standard which takes into account notably the relativistic effects and also the drift introduced by leap seconds. An online applet developed by J. Eastman allows this conversion [94]. After the time converted, I built the specific input file needed for the MCMC code with the help of SPECPHOT. It consists in a text file for each lightcurve that contains the following information for every photometric point: the time in BJD_{TDB}, the flux and its error from the target's differential lightcurve, the exposure time of the image, and the systematics. The systematics (or 'external' parameters) represent astrophysical and instrumental phenomena that can create photometric variations on the lightcurves, their values across an observation are necessary to build the baseline model as we will see after. The considered systematics are the following:

- the full width at half maximum (fwhm) of the PSF[5] that represents its size on the array. The MCMC code also requires the values of fwhm_x and fwhm_y, useful if the PSF is asymmetric, but in this case it is not necessary since SPECULOOS telescopes assume a symmetric PSF.

[5]The point spread function (PSF) describes the response of an optical system (here the telescope) to a point source (here stars).

- dx and dy, the position of the PSF on the pixels. Depending on how it is centered, variations can appear due to inter-pixel and intra-pixel inhomogeneity. The former is still present despite the flat-field division because it only corrects partially this effect. The latter has an impact mostly if the PSF is undersampled and only covers a few pixels. This is the case for instance with the IRAC detector of Spitzer that has a PSF typically with a fwhm ~ 1.5 pixel [95].
- the airmass which quantifies the layers of atmosphere the light from a source has to go through. It equals 1 for an object at the zenith and increases with decreasing altitude. As stars move in the sky during a night, owing to the Earth's rotation, the airmass varies and can cause flux variations on a lightcurve.
- the sky, representing the flux variation in the sky background, originating from diffused/scattered photons from the Moon and/or the Sun, airglow, and so on.

At that stage, the MCMC analysis was ready. It was divided in two parts. Firstly, I performed individual analyses on the 40 lightcurves listed in Table 3.1 aimed at determining independently the physical parameters with a clear focus on their mid-transit time T_0 in the context of this work. Individual analyses also enabled me to select the best baseline model to apply on each lightcurve and study transient phenomenon such as the flare of the 28 Aug 2019. Secondly, I conducted global analyses by grouping all the transits obtained for one specific planet at a time. Subsequently, I increased the number of photometric points given to the MCMC to get the best constraints on the system parameters. It is particularly important for the transit ingress and egress that generally lack measurements due to their short time duration.

Individual analysis

I initiated this part by assuming some prior PDFs for the different parameters that are used for all the individual analyses. A summarize can be found on Table 3.2. Concerning the stellar parameters of TRAPPIST-1, I set normal prior distributions on the mass, effective temperature and metallicity based on the results of E. Ducrot et al. (2020) [46] presented in Table 1.1. Then for each planet I assumed a uniform prior on the transit duration and normal priors on the transit depth[6] and impact parameter also based on the results of E. Ducrot et al. depicted in Table 1.2. In addition, the planets are assumed to be in circular orbit[7] ($e = 0$) and I considered a normal prior on the mid-transit time T_0 which needs to be adapted for each lightcurve since it is changing. I found its approximate value by visualizing the lightcurve with SPECPHOT and thus capturing the position of the transit drop (Fig.3.5). I imposed a relatively high deviation on the prior PDF of T_0 (depending on the lightcurve ~ 5 to 15 minutes) since the assumed mean value was based on visual thought. It should be noted that in the context of individual analyses, the orbital period is not considered as a jump parameter because it cannot be determined from a single transit. I therefore fixed its value for each planet [46].
Those priors on the stellar and planet parameters aimed at isolating the signal of the transits from the noise. It is particularly important in the presented dataset since despite the good-quality data processing, SPECPHOT does not have a functionality to reduce the water vapor perturbations that can be significant.

[6] The transit depths are given at $3.6\mu m$, but I still used these values as priors since dF does not vary significantly with the wavelength (see Subsection 1.2.3).

[7] As seen on Table 1.2, their eccentricity is small so this assumption is acceptable.

As a next step, I started the individual analysis which is divided in three stages for each of the 40 lightcurves.

The goal of the first stage is to obtain the **detrended** lightcurve by compensating the potential photometric variations created by systematic effects that have not been removed previously. The approach of the MCMC is to find the optimal baseline function, that consists in a polynomial combination of the different systematics to which is associated a model order to assess their effects on the lightcurve. The parameters considered by the code are the systematics listed previously (fwhm, dx-dy, airmass, sky) plus the time, to take into account potential time dependent trends. In order to find the optimal baseline function, I made a succession of small MCMC run of $5,000$ steps to observe the effects of the parameters on the lightcurve and on the Bayesian Information Criterion, abbreviated BIC [96]. The BIC is a proxy of a model's 'evidence', i.e. a parameter enabling to quantify the relative probability of several models. It is defined by [87]:

$$BIC = \chi^2 + klog(N) \tag{3.2}$$

Where χ^2 is the smallest chi-square found during the chain, k is the number of free parameters of the model, and N is the number of photometric points relative to the lightcurve (Appendix A).

At the end, the goal is to select the baseline model that results in the smallest BIC, i.e. the model that adjusts the best the data (small χ^2) while having the least parameters possible (small k). This approach can be related to the principle of the Occam's Razor: we must seek for simplicity in the baseline as a too complex one will only have a negative impact (over-detrending). The selected baseline functions are shown in Appendix A. We note that SPECPHOT has a function to visualize the systematics, I used it to have a first overview of which baseline function could be suitable for each lightcurve.

Once I was satisfied with the selected baseline function, I moved on to the second stage of the analysis whose goal is to evaluate how the data are still affected by noise, to estimate the need to rescale the photometric errors of the lightcurve. It is quantified with two scaling factors, β_w and β_r. β_w is the white (uncorrelated) noise linked to measurement errors, as opposed to β_r, which corresponds to the red (correlated) noise and describes the inability of the model to represent perfectly the data. A scaling factor inferior (resp. superior) to 1.00 means that the corresponding noise is overestimated (resp. under-estimated). By multiplying them, we get the correction factor CF that quantifies the need to rescale the photometric errors. To obtain these factors, I run a chain of $50,000$ steps assuming the baseline function selected at the first stage. The correction factors found are written in the Appendix A for the 40 lightcurves.

Finally, I performed for each lightcurve a MCMC analysis composed of two chains of $75,000$ steps with the optimal baseline function and the CF derived as described above. A good convergence of both chains is ensured by using the Gelman-Rubin test, which assesses the ratio of the between-chains and within-chain variances for each model parameter. On the one hand, if it is large, this means the two chains did not converge properly and this should be improved for example with the use of longer chains. On the other hand, if it is close to 1, the convergence is good. Typically, we are satisfied with a ratio < 1.1 for each model parameter, which was the case for every individual analysis performed. After the last stage, I deduced the jump and

derived parameters from the median and $1-\sigma$ deviation of their corresponding posterior PDFs along with the best-fit of the lightcurve.

To summarize:

- I made a succession of $5,000$ steps chains to find the optimal baseline function;
- I estimated the correction factor with a $50,000$ steps chain;
- I deduced my results with 2 chains of $75,000$ steps.

Table 3.2: Assumed prior PDFs on the stellar and planets parameters during the individual analyses.

Parameter	Prior	Value
Star		
Mass $M_\star$	normal	Table 1.1
Effective temperature T_{eff}	normal	Table 1.1
Metallicity [Fe/H]	normal	Table 1.1
Planets		
Transit depth dF	normal	Table 1.2
Impact parameter b	normal	Table 1.2
Mid-transit time T_0	normal	Depends on the lightcurve
Transit duration W	uniform	Table 1.2

Global analysis

The global planet by planet analyses aimed to maximize the constraints on the system parameters from my dataset. I started by grouping together the lightcurves relative to each planet. If several transits were visible in a single observation, I cut it to attribute each transit signal to each planet. This separation could not be done for blended transits, hence I did not consider them during this part (see Table 3.1). I discarded also the two incomplete transits of d as I had a low number of observations for this object, so incomplete transits could have affected the accuracy of the results (bad convergence). On the contrary, I estimated that I had plenty enough lightcurves for b to keep its incomplete transits. Furthermore, I cut the two flare signals on the lightcurves of the 28 Aug and 30 Oct 2019, as they were already characterized during the individual analyses.
In total, I considered in this part 19 transits of b, 8 of c, 5 of d, 3 of e, and 2 of h. The planet f and g were not considered for the global analysis as I had only one transit for each.

I then assumed some prior PDFs (summarize in Table 3.3). I decided to assume less constraining priors than in the individual analysis to let the algorithm explore more freely the parameter space while benefiting from stronger constraints from the data than for individual analyses. In other words, I did not want too important priors to govern the obtained system parameters. For the stellar parameters, I kept normal prior distributions, here on the mass, radius, effective temperature and metallicity, again from Table 1.1. Next, to give more freedom in the

exploration of the parameter spaces by the MCMC, for each planet, I chose less constraining uniform priors on the transit depth, impact parameter and transit duration, based on Table 1.2. I also kept the assumption of a circular orbit ($e = 0$). Moreover, I considered in the global analyses the transit timing variation of each transit as jump parameter. The values input to the algorithm were found by following the approach described in Section 1.3, i.e. by subtracting the timings C, calculated with the equation (1.15), from the observed timings O, derived during the individual analyses. The ephemeris T_0 and P are found by performing a linear regression on the set of observed timings, as described in Chapter 4.

After the lightcurves are grouped, the priors assumed, and the TTVs calculated, I began the global analysis of each planet. It was done in the same way as the individual one, except that I kept the optimal baseline models determined previously for each observation. I started by running a $50,000$ steps chain to estimate the correction factors CF of each lightcurve, and then I performed two chains of $75,000$ steps using the Gelman-Rubin test to ensure a good convergence. Indeed, I got a coefficient < 1.1 for every jump parameter of each planet, attesting the correct convergence of the performed global analyses. Consequently , I obtained the best constrained jump and derived parameters along with the best-fit of each lightcurve. I also got a global best-fit lightcurve by shifting all the transits to a common center, as we saw in Figure 1.9.

Table 3.3: Assumed prior PDFs on the stellar and planets parameters during the global analyses.

Parameter	**Prior**	**Value**
Star		
Mass $M_\star$	normal	Table 1.1
Radius $R_\star$	normal	Table 1.1
Effective temperature T_{eff}	normal	Table 1.1
Metallicity [Fe/H]	normal	Table 1.1
Planets		
Transit depth dF	uniform	Table 1.2
Impact parameter b	uniform	Table 1.2
Transit duration W	uniform	Table 1.2

CHAPTER 4

Results

This chapter will go through the results of this Master thesis as derived from the individual and global analyses of the lightcurves detailed in Subsection 3.3.2. The consistency of my results will be checked by comparing with the scientific literature. In this context, I will notably focus on the paper of E. Ducrot et al. (2020) [46] and L. Delrez et al. (2018) [97] that performed a very precise analysis on the TRAPPIST-1 planets from Spitzer observations. For the TTV, I will focus on the two papers frequently cited through this document, S.L. Grimm et al. (2018) [29] and Agol et al. (2020) [76].

The output files of the MCMC are designed to be autonomously plotted with SuperMongo, but for more flexibility and clarity, I processed those files with Python and made the figures with the package MATPLOTLIB [98].

4.1 Individual analysis

Several inferences could be drawn from the individual analyses. As the goal of this work is to support the next generation of TTV studies, the obtained transit timings will be presented along with their variations. I will then briefly interpret and discuss the scientific significance of the observed flares and blended transits. The interested reader will find the best-fit model of every lightcurve in Appendix B.

4.1.1 Transit timings and variations

In Table 4.1 are shown the median and deviation of the posterior PDF for the 47 mid-transit timings I observed. The time reference is the BJD_{TDB} as it is the most appropriate one for the census of astronomical events [93]. This time is a continuous count of day since a reference epoch thousands of years ago and its current value is around $2,458,000$. For the seek of visual clarity, I remove $2,450,000$ from this count of day as it is commonly done in the literature. Along with that are written the transit timings predicted by Agol et al. (2020) [76], I will detail it later.

It can seen that the errors are typically around $\sim 5 \times 10^{-4}$ day, which represents less than a minute. In comparison, it is the same order of magnitude as what can be found in the literature when the measurements are made from ground-based observations, see for instance the timing data obtained by S.L. Grimm et al. (2018) [29] with TRAPPIST and SPECULOOS. With a state-of-the-art space telescope like Spitzer, the errors are lower, commonly about a dozen of

seconds ([46], [97]). We note that greater errors in the table are associated to bad weather conditions on the observation night, or an incomplete/blended transit for which the timing is generally less properly constrained. For instance, the transit of TRAPPIST-1d on 8759 days has an important error ~ 10 minutes, but the Figure B.32 in Appendix B shows that it is incomplete.

Table 4.1: Observed and predicted ([76]) mid-transit timings along with the $1-\sigma$ errors.

Observed time BJD_{TDB} − 2,450,000 [days]	$-\sigma$ [day]	$+\sigma$ [day]	**Predicted time** BJD_{TDB} − 2,450,000 [days]	σ_{post} [day]
TRAPPIST-1b				
8624.89660	0.00047	0.00045	8624.897058	0.000071
8627.92046	0.00058	0.00091	8627.919382	0.000075
8668.71040	0.00054	0.00050	8668.712760	0.000080
8674.75706	0.00041	0.00041	8674.756757	0.000079
8677.77834	0.00081	0.00074	8677.778275	0.000080
8680.79947	0.00033	0.0003	8680.799792	0.000081
8692.88623	0.00031	0.00031	8692.886822	0.000082
8695.90866	0.00025	0.00026	8695.908853	0.000079
8698.9320	0.0016	0.0020	8698.930827	0.000081
8730.65880	0.00034	0.00032	8730.659359	0.000085
8736.70189	0.00051	0.00046	8736.702778	0.000085
8742.74703	0.00031	0.00033	8742.746433	0.000085
8751.81040	0.00066	0.00067	8751.811219	0.000087
8777.4972	0.0036	0.0022	8777.496147	0.000088
8780.51886	0.00055	0.00051	8780.518472	0.000087
8783.54020	0.00037	0.00034	8783.539932	0.000087
8786.56203	0.00055	0.00093	8786.561775	0.000091
8789.58466	0.00086	0.0011	8789.583209	0.000089
8792.60562	0.00028	0.00026	8792.605540	0.000089
8801.67128	0.00056	0.0005	8801.670277	0.000090
TRAPPIST-1c				
8626.90564	0.00063	0.00058	8626.905460	0.000105
8677.76343	0.00098	0.00091	8677.763907	0.000106
8694.71562	0.00063	0.00059	8694.716477	0.000099
8706.82518	0.00058	0.0006	8706.825474	0.000099
8723.77770	0.00055	0.00058	8723.777878	0.000101
8728.62225	0.00045	0.00045	8728.622363	0.000102
8745.57412	0.00033	0.00032	8745.574317	0.000101
8762.52730	0.00069	0.00064	8762.527513	0.000106
8774.63661	0.00047	0.00049	8774.636574	0.000108
8791.58923	0.00064	0.00059	8791.588685	0.000110
8808.54105	0.00052	0.00053	8808.541828	0.000118

Second part on the next page.

Observed time BJD_{TDB} − 2,450,000 [days]	$-\sigma$ [day]	$+\sigma$ [day]	**Predicted time** BJD_{TDB} − 2,450,000 [days]	σ_{post} [day]
TRAPPIST-1d				
8625.84748	0.00097	0.0010	8625.849060	0.000836
8694.6847	0.0016	0.0017	8694.685220	0.000861
8698.7356	0.0018	0.0017	8698.734924	0.000861
8706.8325	0.0015	0.0014	8706.833050	0.000862
8759.4761	0.0076	0.0071	8759.475206	0.000868
8763.5283	0.0015	0.0016	8763.524963	0.000876
8775.6745	0.0015	0.0013	8775.672985	0.000879
8779.7227	0.0012	0.0013	8779.722169	0.000871
8844.5137	0.0035	0.0057	8844.511679	0.000919
TRAPPIST-1e				
8776.57585	0.00057	0.00059	8776.576115	0.000360
8782.67521	0.00098	0.0011	8782.674774	0.000370
8837.55895	0.00063	0.00070	8837.558790	0.000465
TRAPPIST-1f				
8674.89789	0.00074	0.00068	8674.897346	0.000463
TRAPPIST-1g				
8789.5303	0.0013	0.0011	8789.529882	0.000316
TRAPPIST-1h				
8694.7771	0.0018	0.0021	8694.767888	0.000965
8788.6092	0.0012	0.0012	8788.606513	0.001240

As we have seen in Section 1.3 and Section 1.4, the architecture of the TRAPPIST-1 system creates strong gravitational interactions between the planets, which causes orbital deviations and transit timing variations from a *Keplerian* reference where P is constant. As a result, if we compare the observed timings, denoted O, to what would be measured with a constant period orbit, denoted C, we would be able to visualize the TTV (O-C) from that reference. Here, the observed timings are those written on Table 4.1 and the calculated timings are computed with the equation (1.15). The epoch corresponds to the transit number from the reference at $E = 0$, and are written for each observed event in Appendix A. I then only need to compute the value of the ephemeris P and T_0 for each planet to apply the equation and obtain the TTV with respect to this ephemeris.
I will start by representing the transit timing variations of my dataset alone, and then I will compare them to the results and predictions of the upcoming article of Agol et al. (2020) [76].

The gravitational interactions make the orbital periods of the seven planets vary with time, and their values can quickly drift. As a consequence, the main issue when plotting the TTV signal of a given dataset is to find the average periods during the time interval of the survey, to use as references. To do so, I refined the ephemeris of each planet with a Python function that does

a linear regression on the set of observed timings to calculate P, T_0, and their corresponding errors, by using the ordinary least squares (OLS) statistic method. We note that this function only considers a symmetric error, therefore, I took the highest one of each transit timing on Table 4.1. To centralize the planets parameters to a same table, the computed ephemerides are written in Table 4.3. After that, I plotted on Figure 4.1 the transit timing variations of the planets with respect to their respective mean ephemeris, excluded f and g since it is not possible to perform a linear regression with a single transit time.

Visually, we see that selecting the mean ephemerides makes the TTV signal quite flat, well distributed around the grey vertical line drawn for illustrative purpose at $TTV = 0$. A data point above (resp. below) that line means that the transit happened a few minutes after (resp. before) what would be expected with the *Keplerian* reference. Even though I gathered a non negligible number of transits (47), it is difficult to notice any tendencies in the signal of the different planets. As already mentioned, greater errors are associated to poor weather conditions during the observation, or an incomplete/blended transit.

It is interesting to note again the importance to be in the time reference BJD_{TDB}. In JD, one would observe timing variations over the months that are related notably to the position of the Earth on its orbit rather than to real orbital deviations of the TRAPPIST-1 planets.

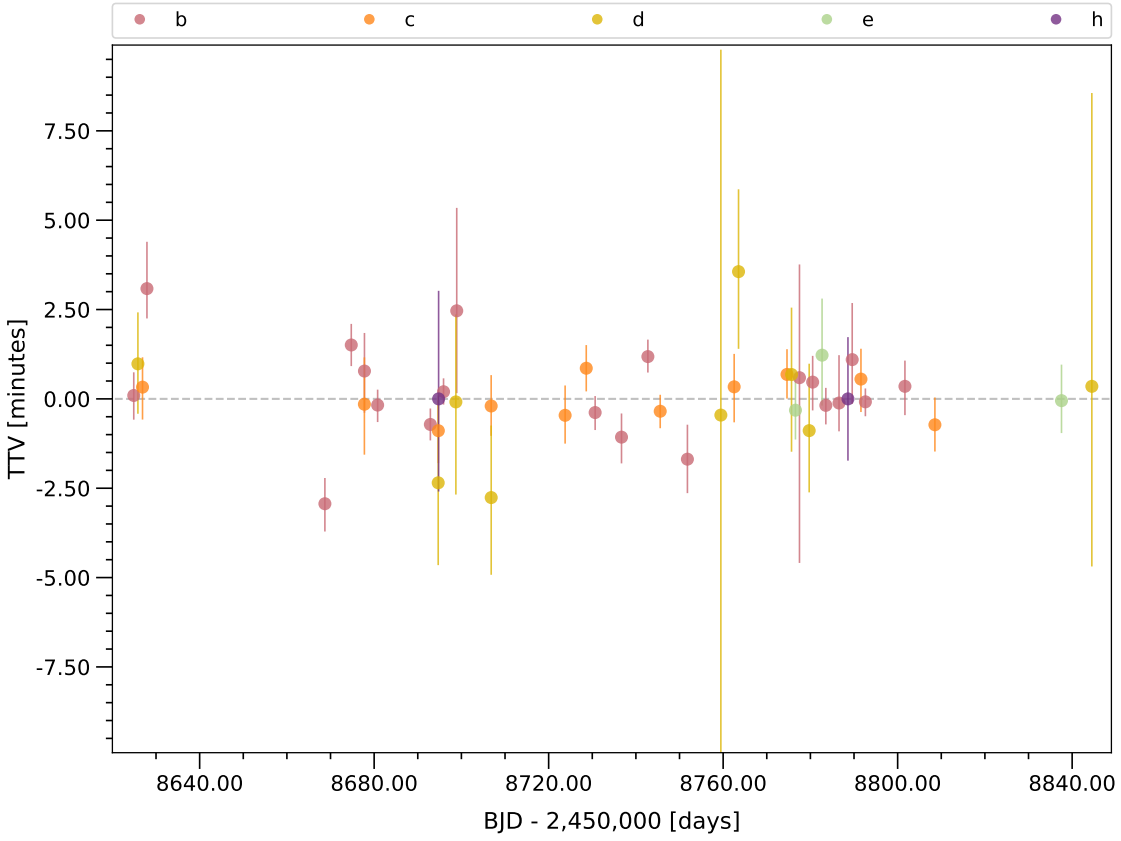

Figure 4.1: Transit timing variations of the observed events of b, c, d, e, and h, with respect to their ephemerides derived from the linear regressions. The errors represented are those of the observed timings (Table 4.1). A vertical line (grey) is plotted for illustrative purpose.

Now, we can analyze my timings and their variations with the results of Agol et al. (2020) [76]. I chose this article because, based on a thorough TTV modeling, it predicts the transit timings of the TRAPPIST-1 planets up to the end of 2019. As a consequence, we are able to compare what I obtained with respect to their predictions, which enables us to assess the accuracy of my measurements but also the accuracy of the TTV model. As mentioned, I included their predictions in the Table 4.1, which consists in the mean t_{post} and standard deviation σ_{post} obtained from the posterior sample of their analysis with a N-body integrator. In the context of this Master thesis, I will not detail how their predictions were computed, but only compare their values with my timing data. The interested reader will find a complete discussion in the concerned article, once it is published.

For a visual approach, I also built figures (Fig.4.2) displaying for each planet: (1) the best-fit transit-time model they computed (blue), (2) the transit timing variation measurements (+ errors) they used (black), based on Spitzer, K2, and ground-based observations, and (3) the measurements obtained from my work (+ errors), keeping the same color code as the Figure 4.1 for the planets. We note that the TTV are now calculated with the ephemerides used by Agol et al., in order for the variations to be based on the same reference.

From a quantitative approach with the exact values in Table 4.1, or a qualitative one with the figures, we notice an excellent agreement between the predictions and my measurements. The difference is typically around a minute, which is similar to the order of magnitude of the errors in my measurements. However, we still identify some noticeable outliers. For TRAPPIST-1b, the transit around 8668 days has a difference of more than 3 minutes. It cannot be explained by bad weather conditions since they were appropriate, and there is nothing unusual about its lightcurve (Fig.B.3). Such unexplained variations have also been found by Agol et al., they estimated that about 10% of their transits were affected at different levels. It could be due to an unknown systematic effect, stellar variability, or even a flare. However, to impact the computed timing, a flare should occur during the transit ingress or egress, which is unlikely due to their short timescale. For TRAPPIST-1d, we have one outlier at 8763 days that is certainly due to bad weather conditions. It can be seen on Figure B.33 that shows a poor quality lightcurve. We note that no data points were collected in 2019 by Agol et al. for this planet, my measurements are therefore interesting as they allow to confirm the sharp decrease seen on the corresponding figure. For TRAPPIST-1h, we notice that the two data points do not fit the predictions, with a difference respectively of 13.2 and 3.85 minutes. The weather conditions can provide an explanation as they were not optimal for both observations, in particular for the first transit. Indeed, we can see on Figure B.22 significant variations in the photometric points, even when corrected with an important baseline function. The difference with the predictions could also be explained by a less accurate TTV modeling for this planet. As it is the most distant one of the system, its relatively long period makes its observation less frequent, which decreases the amount of timing data, hence the accuracy of the predictions.
We notice with the figures that the TTV signals of the TRAPPIST-1 planets are varying over several years, so my measurements obtained over a few months are clearly not sufficient to result in a meaningful TTV modeling. It is also interesting to note that, in some cases, we can visually understand how the planets are interacting. For instance, b and c display TTV signals closely anti-correlated, which shows that they interact preferably with each other.

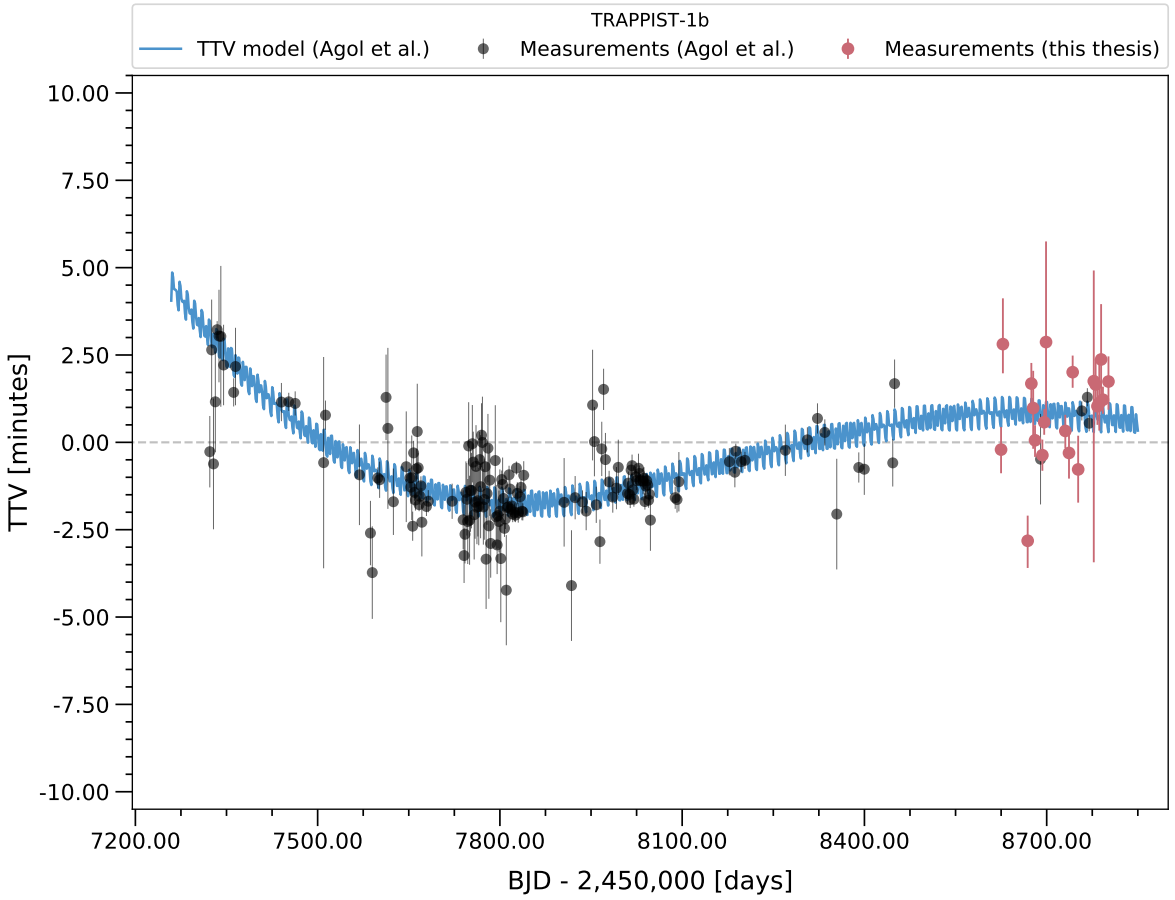
TRAPPIST-1b
TTV model (Agol et al.)
Measurements (Agol et al.)
Measurements (this thesis)
TTV [minutes]
10.00
7.50
5.00
2.50
0.00
-2.50
-5.00
-7.50
-10.00
7200.00
7500.00
7800.00
8100.00
8400.00
8700.00
BJD - 2,450,000 [days]

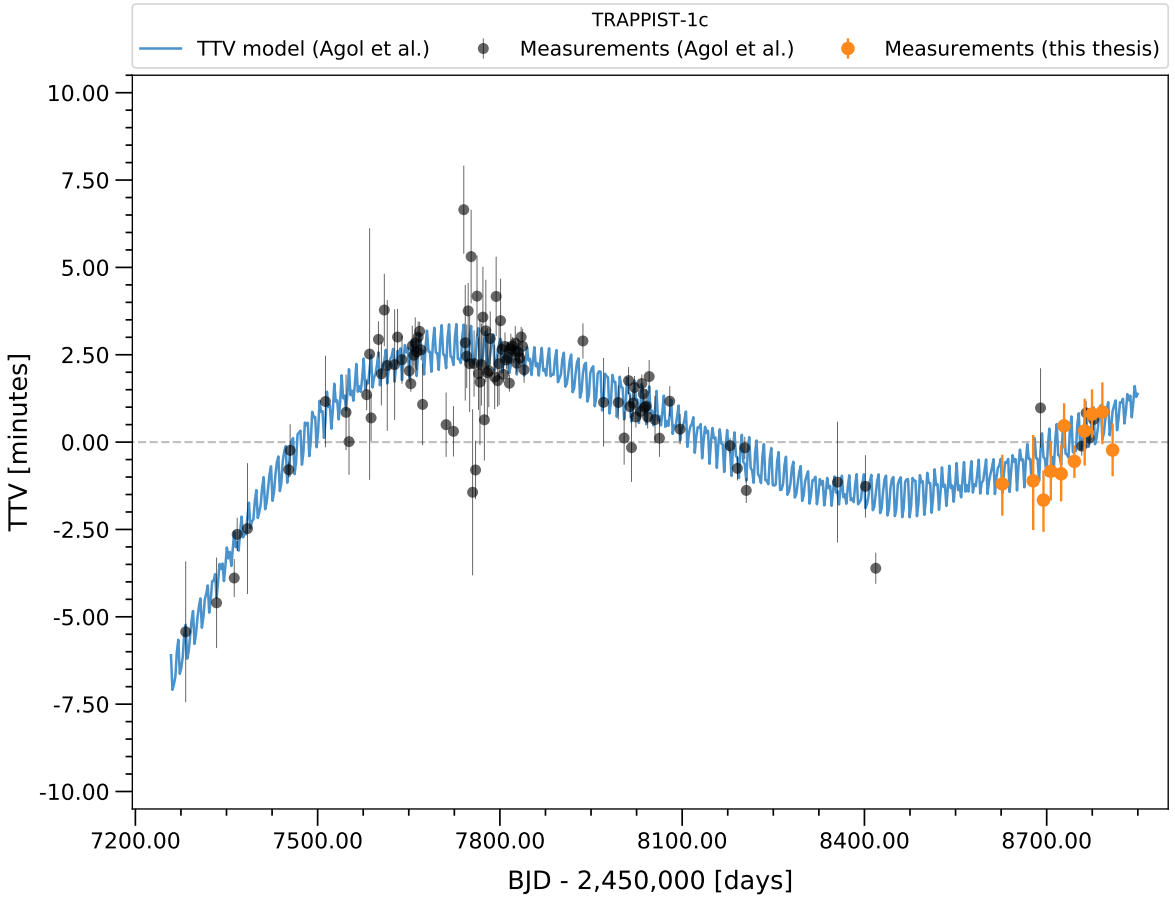
TRAPPIST-1c
TTV model (Agol et al.)
Measurements (Agol et al.)
Measurements (this thesis)
TTV [minutes]
10.00
7.50
5.00
2.50
0.00
-2.50
-5.00
-7.50
-10.00
7200.00
7500.00
7800.00
8100.00
8400.00
8700.00
BJD - 2,450,000 [days]

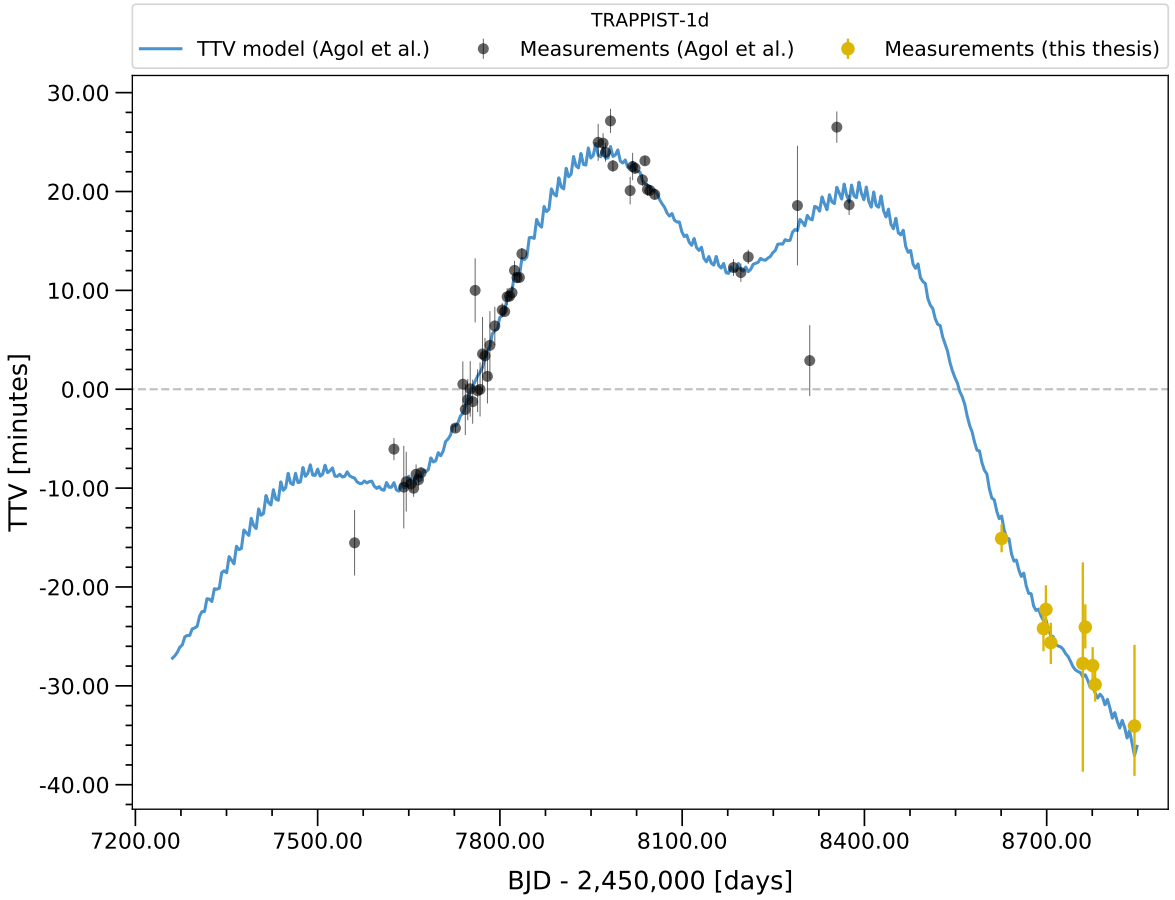
TRAPPIST-1d
TTV model (Agol et al.)
Measurements (Agol et al.)
Measurements (this thesis)
TTV [minutes]
30.00
20.00
10.00
0.00
-10.00
-20.00
-30.00
-40.00
7200.00
7500.00
7800.00
8100.00
8400.00
8700.00
BJD - 2,450,000 [days]

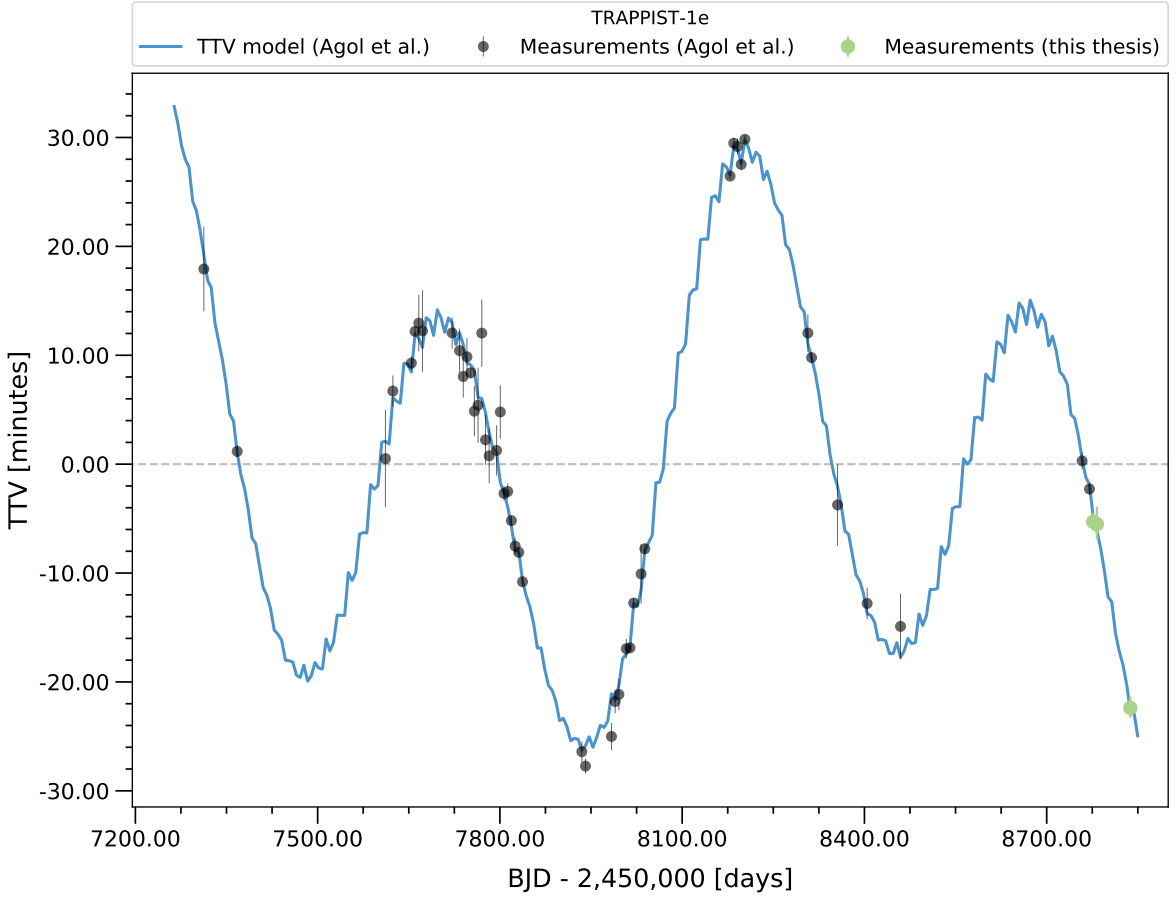
TRAPPIST-1e
TTV model (Agol et al.)
Measurements (Agol et al.)
Measurements (this thesis)
TTV [minutes]
30.00
20.00
10.00
0.00
-10.00
-20.00
-30.00
7200.00
7500.00
7800.00
8100.00
8400.00
8700.00
BJD - 2,450,000 [days]

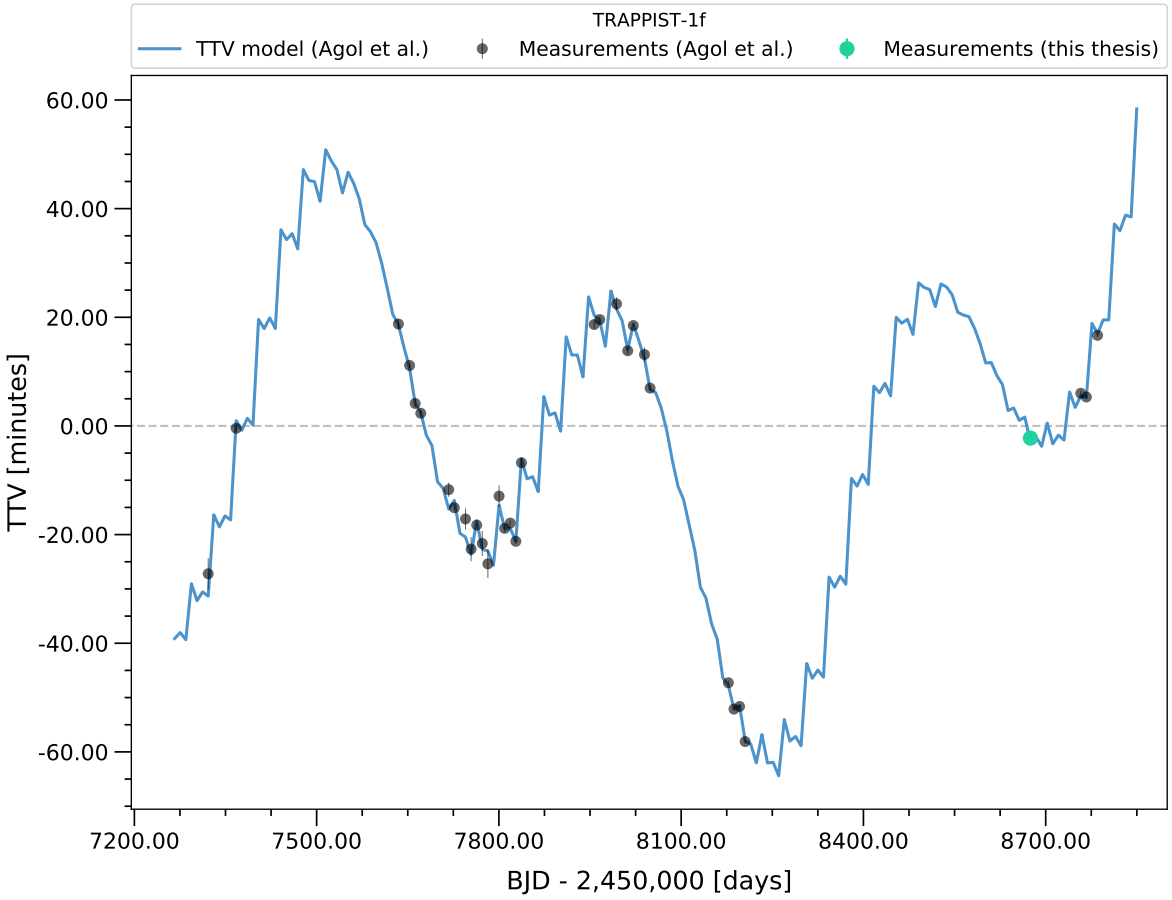
TRAPPIST-1f
TTV model (Agol et al.)
Measurements (Agol et al.)
Measurements (this thesis)
60.00
40.00
20.00
0.00
-20.00
-40.00
-60.00
TTV [minutes]
7200.00
7500.00
7800.00
8100.00
8400.00
8700.00
BJD - 2,450,000 [days]

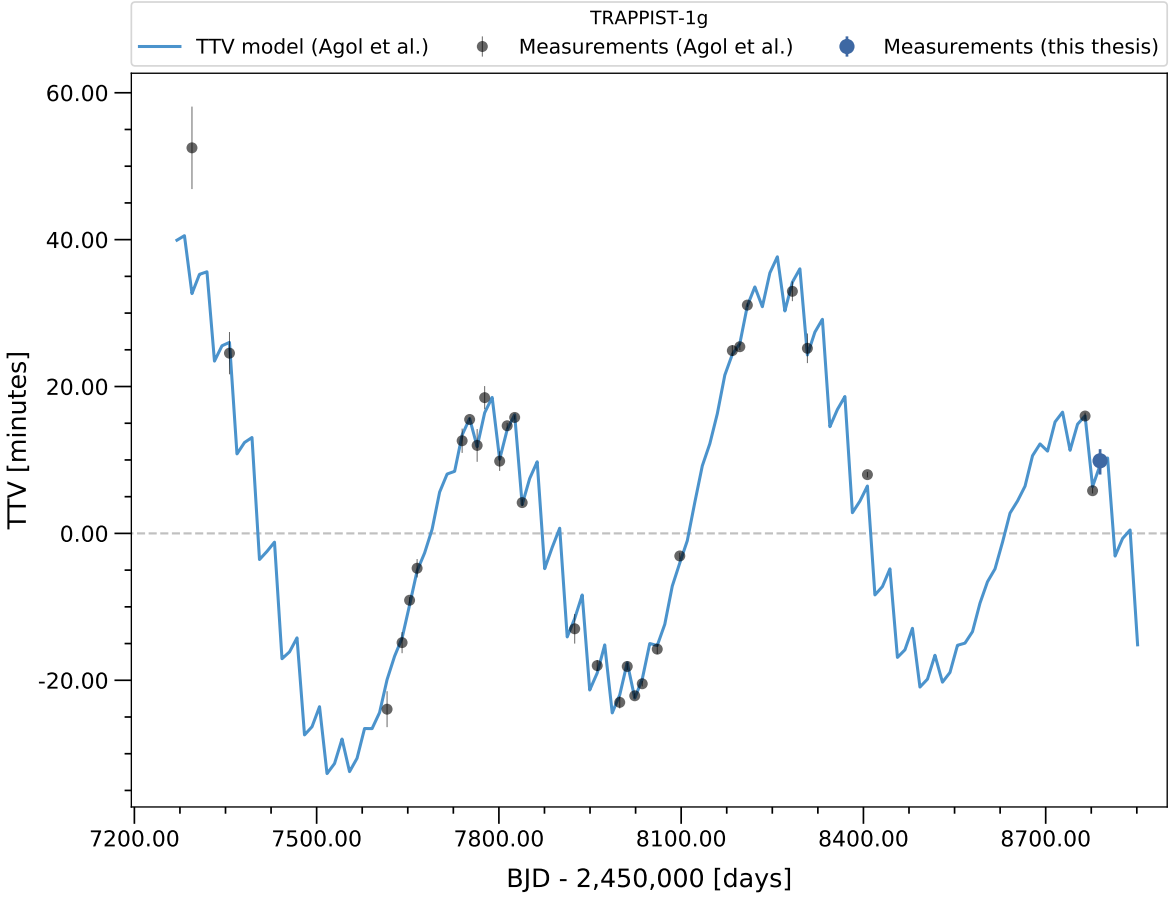
TRAPPIST-1g
TTV model (Agol et al.)
Measurements (Agol et al.)
Measurements (this thesis)
60.00
40.00
20.00
0.00
-20.00
TTV [minutes]
7200.00
7500.00
7800.00
8100.00
8400.00
8700.00
BJD - 2,450,000 [days]

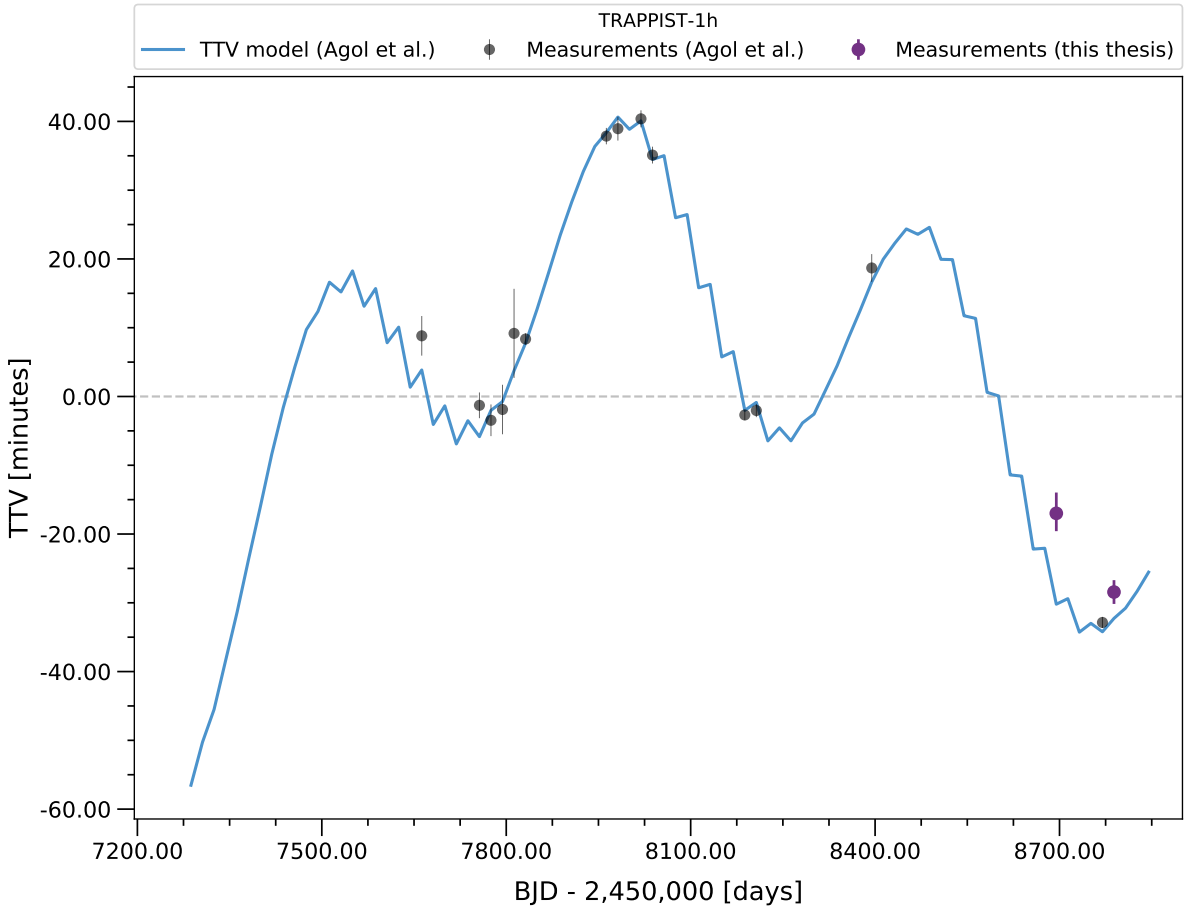

Figure 4.2: Transit timing variations of the TRAPPIST-1 planets. The measurements of Agol et al. (2020) with K2, Spitzer, or ground-based telescopes are in black, their best-fit transit-time models in blue, and my measurements are in the color corresponding to the planet. A vertical line (grey) is plotted for illustrative purpose.

4.1.2 Flares

As we mentioned, Ultra-Cool Dwarf stars can have an important magnetic activity, resulting in flares which are associated with the release of energy during magnetic reconnections [12]. They create emissions across the spectrum, and can therefore be seen in the observations in the infrared. On the lightcurves, they correspond to a peak of the flux received from the star, followed by an exponential decay. They are characterized by three parameters: (1) the peak timing t_0, (2) the flux amplitude A, and (3) the timescale τ. They are represented in the MCMC code with the equation [46]:

$$F(t) = A \times \exp\Big[-(t - t_0)/\tau \Big] \tag{4.1}$$

where $F(t)$ represents the flux changing across the time.

Depending the cases, it can be challenging to recognize if a flux peak in the lightcurve is linked to a flare, or to potential external perturbations. Indeed, despite the image calibration, differential photometry, and detrending, some variations not intrinsic to the TRAPPIST-1 system

still remain. To investigate, I first looked at the number of photometric points in the flux peak. Typically, a single point is not sufficient to prove we have a flare. Then, I tried several baseline functions to see if it was possible to compensate the variation. If it was the case, it meant that the flux peak was probably not due to the star but to other variations (e.g. sky background variation). And finally, I looked at the water vapor variation the night of the observation. Since my lightcurves are not corrected for it, it was indeed an important thing to check. For instance, a sharp change of the water vapor in the atmosphere at the same time as the flux peak could discard a potential flare.

In total, I could identify two clear flare signals. One after the transit of TRAPPIST-1c on 28 Aug 2019, and one before the transit of TRAPPIST-1b on 30 Oct 2019. They are displayed on Figure 4.3. The values of the three parameters computed by the MCMC individual analyses are shown in Table 4.2 for both flares.

In a scientific context, the observation and characterization of flares from UCD stars is important. Indeed, we have seen in Section 1.4 that the flaring activity can have a significant impact on the planets and their habitability. But to assess accurately their impact, it is necessary to well constrain their frequency and energy, which requires to lead a study on a large sample of flare data. However, flares have a short time duration and are not predictable, hence the probability to observe them is low. As a consequence, every observed flare matters, and the data of the two additional flares reported in this Master thesis will certainly be useful to support future work about the impact of TRAPPIST-1 flares on its planets. A first step would be to determine the energy of the two flares, for instance following the approach of T. Shibayama et al. (2013) [99], to see if it follows the flare energy power law computed by E. Ducrot et al. (2020) for TRAPPIST-1. Depending on the flare distribution, some planets of the system could be positively impacted as the flares could trigger prebiotic chemistry [59].

Table 4.2: Parameters of the two flares observed during the survey, as computed with the individual MCMC analyses.

UT date	**Timing** $BJD_{TDB} - 2,450,000$ [days]	**Amplitude** [%]	**Timescale** [day]
2019/08/28	$8723.79946^{+0.00014}_{-0.00013}$	$3.23^{+0.83}_{-0.61}$	$0.00097^{+0.00030}_{-0.00023}$
2019/10/30	$8786.53957^{+0.00038}_{-0.00034}$	$0.81^{+0.19}_{-0.17}$	$0.0117^{+0.010}_{-0.0044}$

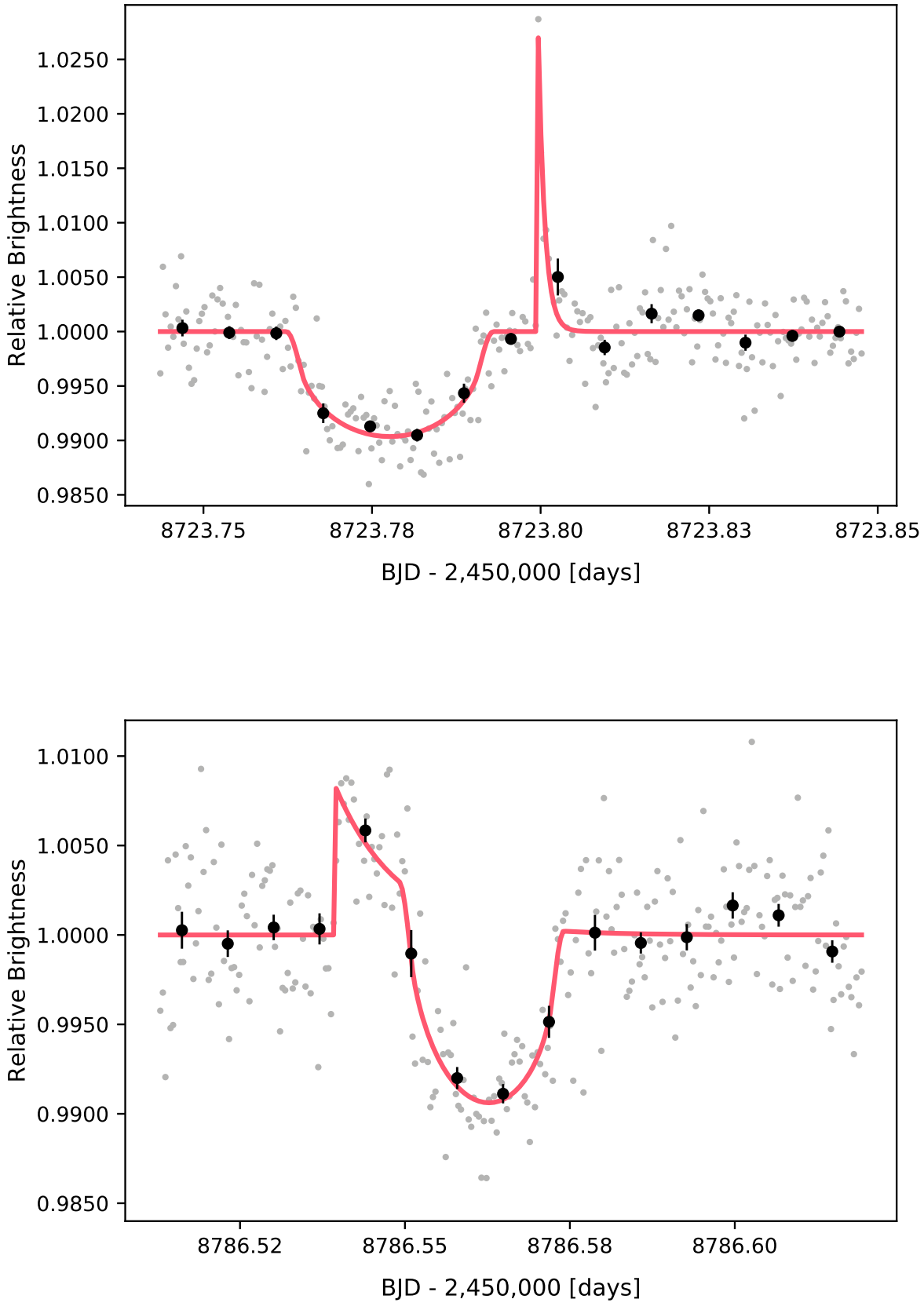

Figure 4.3: Transit lightcurves of TRAPPIST-1 on 28 Aug (top) and 30 Oct 2019 (bottom). The photometric points corrected with the baseline model are in grey and binned per 10 minutes in black (with the error bars). In red is superimposed the best-fit lightcurve computed with the MCMC.

4.1.3 Blended transits

When we deal with transiting multiplanetary system, it is probable that two planets or more transit their host at the same time, resulting in blended transits on the lightcurve. In such a case, the shape of the signal can be complex, and is only dependent on the system configuration at this time. For instance, we could be in a *caught-up* configuration where an outer slower planet starts its transit, and an inner one with a superior orbital velocity catches up the other one. Another example was shown on Figure 1.10, where we can see a triple transit signal created by TRAPPIST-1c, e and f. Most of the time, blended transits create an impressive signal, but that does not bring any additional information about the system. But there is one specific case that can allow interesting constraints on the system parameters. If we deal with a co-planar multiplanetary system with a nearly edge-on orientation, like TRAPPIST-1, it is possible to observe a planet-planet transit, also called mutual transit [100]. During such an event, the disks of the two planets in transit overlap, resulting in a decrease of the eclipsed fraction of the stellar disk, and thus to a minor flux increase in the lightcurve. With the shape and time of the bump, one can constrain the mutual inclination between the concerned planets and investigate their prograde or retrograde motions. For example, it had been observed by Hirano et al. (2012) [101] during a photometric survey of Kepler-89[1] (Fig 4.4). We note that such a brightening can also be linked to one planet obscuring a starspot, but it is unlikely to confuse them because the amplitude and duration of the bump is different [100].

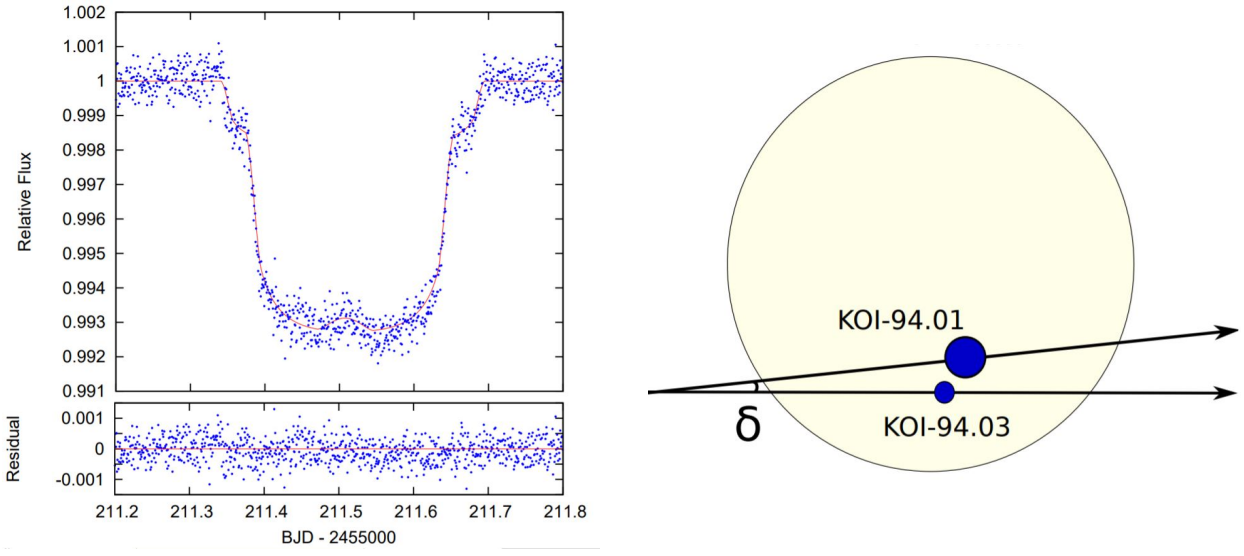

Figure 4.4: Left: blended transit lightcurve of Kepler-89d and e. The brightening in the center is due to the partial occultation of the inner planet d by the outer e. Right: Schematic (not to scale) showing the configuration and mutual inclination creating the observed bump. [101]

From the analyzed dataset, I report the observation of three blended transits, but none of them present a planet-planet transit. The associated lightcurves are shown on Figure 4.5 with an illustration of the system configuration at different times of the events. To build this representation, I fixed on the plot the radius of the star and I calculated those of the planets using the parameter $R_p/R_\star$ obtained from the MCMC analyses (Table 4.3), by doing so, I ensured

[1] In the article, the system is referred to as KOI-94 (Kepler Object of Interest) since its exoplanets were not officially confirmed.

that the star and the planets are in scale. I then drew a vertical line at a distance b of the star center representing the motion of the planets, where b is the impact parameter (Table 4.3). After that, I computed the position of the planets by using the transit duration (Table 4.3) and by assuming that they have a circular orbit ($e = 0$) so the orbital velocity is constant. As they orbit at different distances from their host, they have different velocities, hence the relative distance between them on sky vary. For instance, on the first figure, we can see that b is getting closer to c with time. It is worth mentioning that, by convention, we represent them transiting the northern part of the stellar disk, but in fact we cannot determine if it is this one or the southern one.

The first figure (13 Jul 2019) is a blend of c and b. We can see a first drop in the received flux due to c, after its ingress it is joined by b, that creates an additional drop. Then the flux increases from the egress of c, and then b. Then, on the second figure (30 Jul 2019) is a blend of c and d, but partial as only the egress of d/ingress of c are concerned. We note the poor quality of this lightcurve due to bad weather conditions that night, and the transit of h after c and d. Finally, the third one (11 Aug 2019) is also a blend of c and d. We can see that d starts its ingress right after the one of c, which creates a nearly continuous ingress.

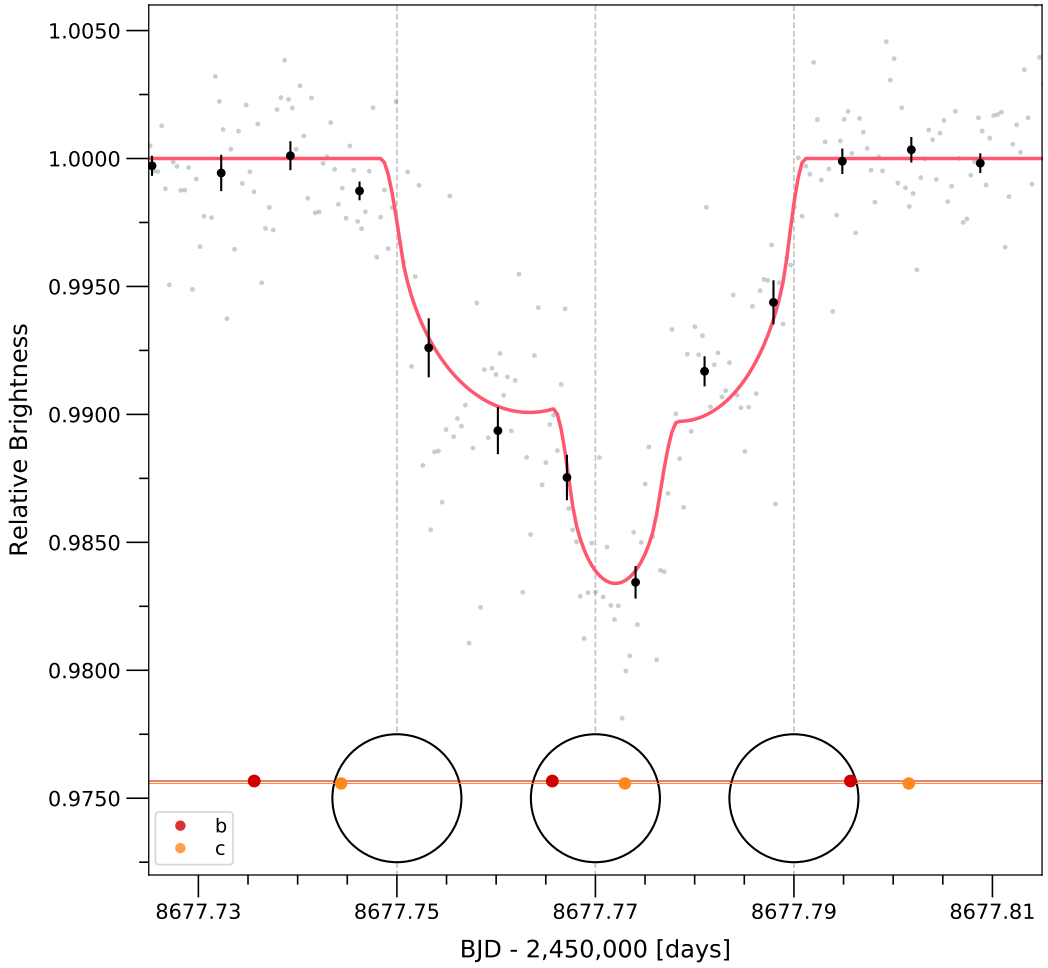

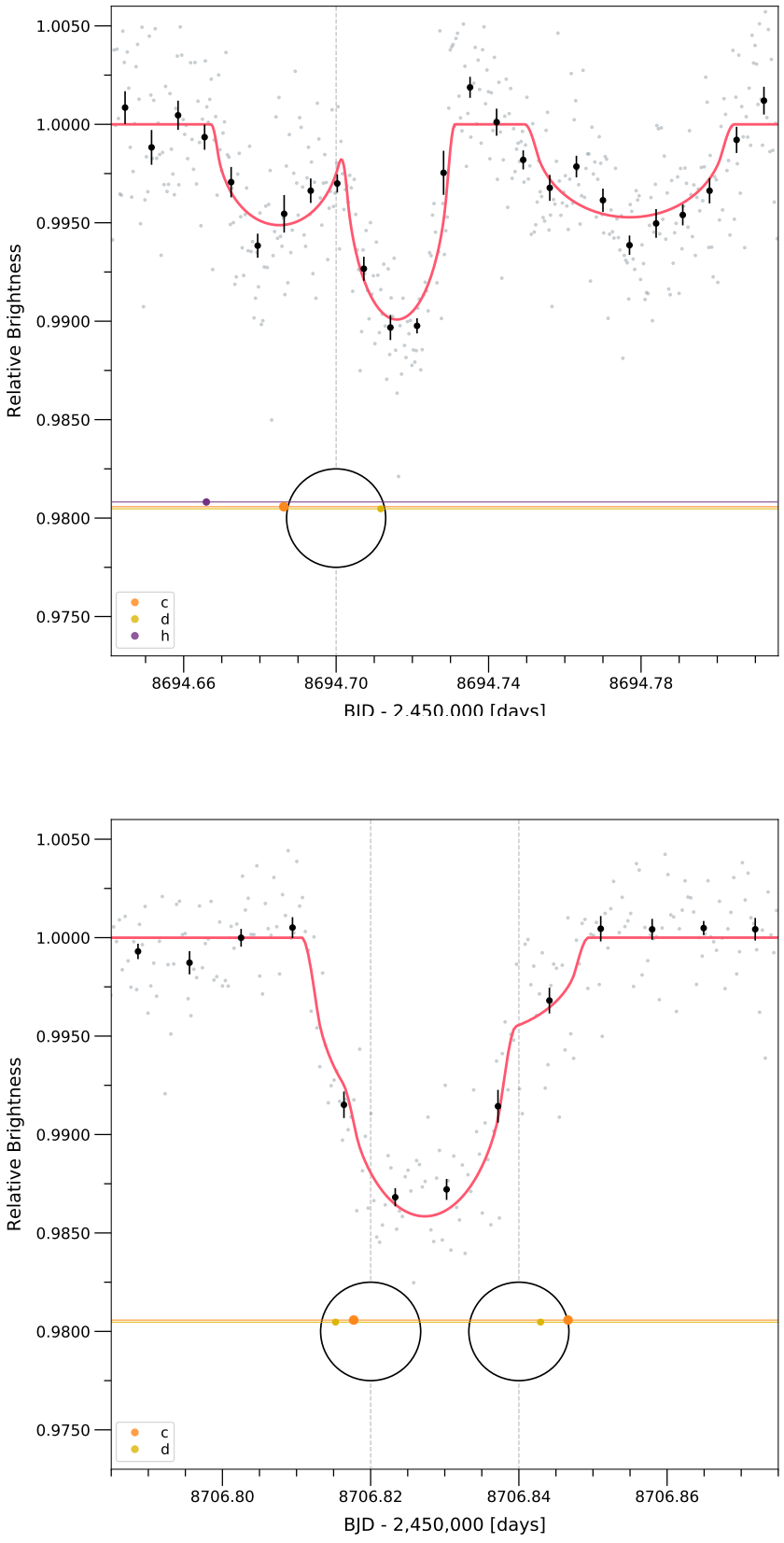

Figure 4.5: Transit lightcurves of TRAPPIST-1 on 13 Jul (top), 30 Jul (middle) and 11 Aug 2019 (bottom). Here also, the corrected photometric points are in grey and the binned in black (with the error bars), and in red is the best-fit lightcurve computed with the MCMC. On the bottom part of each figure is the illustration of the system configuration at different times.

4.2 Global analysis

In this section are shown the results of the global planet-per-planet analysis of TRAPPIST-1b, c, d, e, and h, for which I considered respectively 19, 8, 5, 3 and 2 transits. The computed system parameters (median and 1-σ errors of the posterior PDFs) are written in Table 4.3. To centralize all the information to a same table, I added the parameters of f and g obtained from a second individual analysis, in which I took the same priors as the global analysis. By doing so, I ensured that all the parameters are computed in the same conditions. I also included the period and T_0 found earlier from the linear regressions on the observed timings, except for f and g since it is not feasible from a single transit.

The stellar parameters are obtained from the analysis of each planet. We can see that their values are similar but not exactly equal, for example for the density $\rho_\star$. The difference between them could be explained by the unequal distribution of data between each planet, so an object for which I observed less transits is more subjected to perturbations and its analysis is less accurate. Following this approach, with 19 transits, the global analysis of b would be the most precise one. But it could also be due to the computation of the stellar parameters being biased by intrinsic properties of the planet used for the analysis. Regarding the stellar density, it is calculated in the MCMC code using the transit shapes and Kepler third's law. But as there are seven planets in the system, it makes seven possible paths to $\rho_\star$. In this context, one could naturally expect the choice of the planet in the analysis to influence the computed stellar parameters. As a consequence, to constrain them properly from the dataset, it is preferable to perform a global analysis with all the planets together, to reduce the potential bias. This brief discussion shows one of the advantage of having several planets in a system, as it is not possible to compensate such a bias in a system with a single known exoplanet. Even though it could have been interesting to do so, I did not perform such a complete global analysis as the computation of accurate stellar parameters is not the goal of this work.
Nevertheless, I plotted the deduced stellar density as a function of the period of the planet used for the analysis, to look for a potential bias like observed by E. Ducrot et al. (2020) [46], but I did not find anything noticeable. However, this result does not discard the finding of the mentioned article, as my dataset is less extended and the deduced stellar density certainly less accurate than with Spitzer[2].

Concerning the planets parameters, we can see that my results are in good agreement with the literature, see for instance those of E. Ducrot et al. (2020) [46] written in Table 1.2. The major difference comes from the order of magnitude of the errors, higher in my case. Again, it can be explained by the fact that my results are obtained from ground-based observations, while those presented in the literature ([42], [46], [97]) are generally achieved using the state-of-the-art Spitzer telescope. Moreover, regarding the number of transits, I have less data than those studies. As a consequence, in my case, the analyses, hence the deduced parameters, are more likely to be affected by external perturbations.

[2]As mentioned, the transit shape is used to compute this parameter. Since I did ground-based observations without a correction on the water vapor, it is certain that the shape, hence the stellar density, is better constrained in the article of E. Ducrot et al. (2020) since it is based on precise Spitzer measurements.

The transits analyzed to compute the parameters of the star and the planets are shown on Figure 4.6 in a so-called period-folded plot[3]. It is built by grouping the photometric points of the considered transits, centered to a common center by taking into account the TTVs (jump parameters in the global analyses). They are separated vertically planet by planet with a constant offset of 0.02 between each. The photometric points are corrected following the baseline model of their corresponding observation, they are represented in a different color depending on the planet. In white are displayed the photometric measurements binned per 10 minutes for visual clarity, along with the error bars. The best-fit transit models are shown as dark lines and they are computed from the global analyses for b, c, d, e, and h, and from individual analyses for f and g. We can clearly see the difference of data between the planets, for instance b (red) has the highest density of points thanks to the 19 transits considered. We also observe the variation of the transit duration depending on the planets, being longer for outer planets as their orbital velocity is smaller. Moreover, as a result of the combination of the lightcurves, the number of photometric points in the bin is increased so the error bars are nearly not visible (see discussion in Appendix B). If we compare with the articles already cited previously, all showing a period-folded plot of TRAPPIST-1 transits from Spitzer observations, we can see that my lightcurves look deeper and more rounded. This is only a visual effect due to the limb darkening, more significant in my observations with SSO telescopes in the near-IR than in the IR with Spitzer (3.6 μm and 4.5 μm). This effect can also be seen in the lightcurves of the individual analyses shown in Appendix B.

[3]As a reminder, I used 19 transits of b, 8 of c, 5 of d, 3 of e, 1 from f and g, and 2 of h.

Table 4.3: Parameters of the TRAPPIST-1 planets constrained from my observations. They were all deduced from global (or individual for f and g) MCMC analyses, except P and T_0 that were obtained through a linear regression on the transit timings.

Planet	**b**	**c**	**d**	**e**	**f**	**g**	**h**
Transit depth (%)	$0.761^{+0.033}_{-0.034}$	$0.709^{+0.041}_{-0.034}$	$0.349^{+0.027}_{-0.024}$	$0.466^{+0.035}_{-0.031}$	$0.630^{+0.076}_{-0.073}$	$0.727^{+0.024}_{-0.024}$	$0.398^{+0.044}_{-0.04}$
Impact parameter ($R_\star$)	$0.269^{+0.1}_{-0.16}$	$0.231^{+0.12}_{-0.15}$	$0.189^{+0.14}_{-0.13}$	$0.242^{+0.13}_{-0.15}$	$0.274^{+0.14}_{-0.17}$	$0.481^{+0.065}_{-0.083}$	$0.327^{+0.15}_{-0.2}$
Transit duration (min)	$35.928^{+0.504}_{-0.418}$	$42.374^{+0.778}_{-0.763}$	$49.828^{+1.397}_{-1.44}$	$56.686^{+1.426}_{-1.44}$	$65.205^{+2.016}_{-2.16}$	$66.627^{+1.872}_{-1.872}$	$80.101^{+3.168}_{-3.888}$
$R_p/R_\star$	$0.0872^{+0.0019}_{-0.002}$	$0.0842^{+0.0024}_{-0.0021}$	$0.0591^{+0.0022}_{-0.0021}$	$0.0682^{+0.0025}_{-0.0023}$	$0.0794^{+0.0046}_{-0.0048}$	$0.0852^{+0.0014}_{-0.0014}$	$0.0631^{+0.0034}_{-0.0033}$
Inclination (°)	$89.24^{+0.45}_{-0.32}$	$89.52^{+0.3}_{-0.26}$	$89.72^{+0.19}_{-0.22}$	$89.73^{+0.17}_{-0.15}$	$89.77^{+0.14}_{-0.12}$	$89.67^{+0.06}_{-0.05}$	$89.83^{+0.1}_{-0.08}$
Semi-major axis (10^{-3} AU)	$11.536^{+0.095}_{-0.097}$	$15.80^{+0.13}_{-0.14}$	$22.24^{+0.19}_{-0.19}$	$29.25^{+0.25}_{-0.26}$	$38.48^{+0.33}_{-0.34}$	$46.87^{+0.40}_{-0.40}$	$61.89^{+0.53}_{-0.53}$
Scale parameter $a/R_\star$	$20.26^{+0.49}_{-0.53}$	$27.66^{+0.64}_{-0.73}$	$38.53^{+0.96}_{-0.93}$	$51.0^{+1.3}_{-1.3}$	$67.2^{+1.7}_{-1.8}$	$82.6^{+2.5}_{-2.3}$	$108.2^{+3.0}_{-2.9}$
Equilibrium temperature[1] (K)	$395.9^{+8.1}_{-7.5}$	$338.9^{+6.9}_{-6.4}$	$287.0^{+5.9}_{-5.6}$	$249.7^{+5.0}_{-5.0}$	$217.4^{+4.4}_{-4.4}$	$196.0^{+4.2}_{-4.2}$	$171.4^{+3.5}_{-3.5}$
Irradiation ($S_\odot$)	$4.08^{+0.34}_{-0.3}$	$2.19^{+0.18}_{-0.16}$	$1.127^{+0.095}_{-0.086}$	$0.645^{+0.053}_{-0.051}$	$0.371^{+0.031}_{-0.029}$	$0.245^{+0.022}_{-0.02}$	$0.143^{+0.012}_{-0.011}$
Radius ($R_\oplus$)	$1.162^{+0.052}_{-0.043}$	$1.126^{+0.052}_{-0.036}$	$0.799^{+0.036}_{-0.032}$	$0.916^{+0.045}_{-0.039}$	$1.066^{+0.073}_{-0.072}$	$1.133^{+0.036}_{-0.036}$	$0.846^{+0.055}_{-0.051}$
Period (days)	1.51089317 ±0.00000299	2.42181510 ±0.00000882	4.04938344 ±0.00003382	6.09829108 ±0.00008896	/	/	18.76642191 ±0.00048373
Mid-transit time T_0 - 2,450,000 (BJD_{TDB})	7322.5066268 ±0.0000911	7282.7980359 ±0.0002162	7670.1923078 ±0.0005428	7660.5888024 ±0.0012156	/	/	7662.6238595 ±0.0037084
Mass $M_\star$ ($M_\odot$)	0.0898 ± 0.0022	0.0899 ± 0.0023	0.0896 ± 0.0023	0.0899 ± 0.0024	0.0898 ± 0.0023	0.0901 ± 0.0023	0.0899 ± 0.0023
Radius $R_\star$ ($R_\odot$)	$0.1225^{+0.0032}_{-0.0028}$	$0.1229^{+0.0031}_{-0.0027}$	$0.1241^{+0.003}_{-0.0029}$	$0.1232^{+0.0031}_{-0.003}$	$0.1231^{+0.0032}_{-0.003}$	$0.1220^{+0.0033}_{-0.0033}$	$0.1231^{+0.0032}_{-0.0031}$
Density $\rho_\star$ ($\rho_\odot$)	$48.9^{+3.7}_{-3.7}$	$48.4^{+3.5}_{-3.7}$	$46.8^{+3.6}_{-3.3}$	$48.0^{+3.8}_{-3.6}$	$48.1^{+3.8}_{-3.8}$	$49.6^{+4.6}_{-4.1}$	$48.2^{+4.1}_{-3.8}$
Luminosity $L_\star$ ($L_\odot$)	$0.000543^{+0.000045}_{-0.000039}$	$0.000547^{+0.000045}_{-0.00004}$	$0.000558^{+0.000046}_{-0.000042}$	$0.000552^{+0.000045}_{-0.000042}$	$0.000549^{+0.00004}_{-0.000042}$	$0.000538^{+0.000047}_{-0.000044}$	$0.000548^{+0.000046}_{-0.000042}$
Effective temperature T_{eff} (K)	2520 ± 39	2520 ± 39	2520 ± 39	2522 ± 40	2520 ± 39	2520 ± 39	2520 ± 39
Metallicity [Fe/H] (dex)	$0.0515^{+0.091}_{-0.087}$	$0.0507^{+0.087}_{-0.088}$	$0.0512^{+0.089}_{-0.084}$	$0.0528^{+0.09}_{-0.086}$	$0.0563^{+0.087}_{-0.089}$	$0.0533^{+0.089}_{-0.086}$	$0.0528^{+0.09}_{-0.089}$

[1] assuming a null Bond albedo.

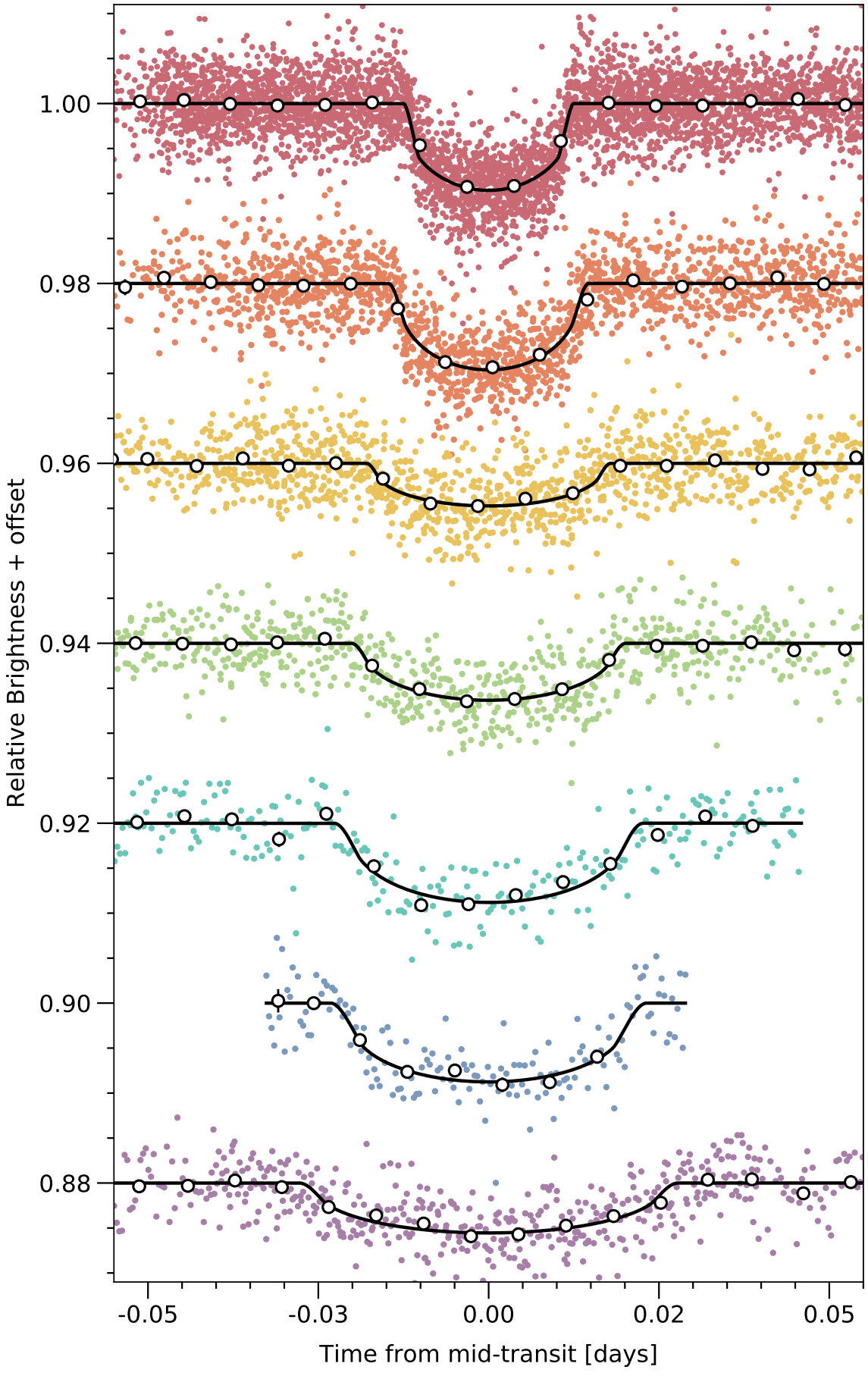

Figure 4.6: Period-folded plot showing the corrected photometric points, unbinned and binned per 10 minutes (+ errors), along with the best-fit transit models from the global (or individual for f and g) analyses. From top to bottom: b, c, d, e, f, g, h. To obtain these combined lightcurves (except for f and g), the individual transits were corrected from their best-fit TTV before proceeding to the period-folding.

CHAPTER 5

Conclusions and future prospects

The Io telescope of the SPECULOOS Southern Observatory observed 47 transits of the TRAPPIST-1 planets spread on 40 nights between May and December 2019. Based on the raw data reduced with the autonomous SSO pipeline, I performed differential photometry with the Python package SPECPHOT to obtain accurate lightcurves of the target for each observation. I then subjected these lightcurves to a MCMC algorithm following an individual approach, and a global planet-per-planet one excepted some discarded transits (blended or incomplete). At the end, and in accordance with the goal of this Master thesis, I measured the timings of every observed event with a precision comparable to what is usually achieved in the literature from ground-based observations. As by-products of this transit monitoring, I also identified two flares of the host star and three blended transits, which unfortunately do not show any hint of a planet-planet transit configuration. In addition, I deduced the parameters of the star and the seven planets, as constrained by my dataset. Even though it was not the goal of this work, the fact that I obtained results consistent with the literature attests of the correct photometric reduction and analysis of the lightcurves. It also shows the great ability of the SPECULOOS network to constrain the parameters of an extrasolar system even from ground-based observations. By the diversity of these results, it can be clearly noticed how powerful the transit method is. Even though my work was focused on transit timings, the observations are so rich in information that they also constrained the flaring activity of the star, the main parameters of the system, and the frequency and topology of their multiple transits. And these only represent what could be done according to this dataset alone, as the transiting configuration makes possible many other detailed studies of a planetary system, for instance to constrain the heterogeneity of the stellar photosphere, to measure the atmospheric composition and the orbital obliquity of the planets, or even to look for potential additional objects [11].

Even though this Master thesis reports an important number of timings, it is not sufficient to result in a meaningful TTV study of the complex TRAPPIST-1 system. Indeed, the article of S.L. Grimm et al. (2018) [29] that offered a first thorough application of this method on TRAPPIST-1 estimated the masses of the seven planets with a precision ranging from 8 to 17% , by using in total 284 transit timings. More recently, with 447 timings Agol et al. (2020) [76] significantly increased our knowledge of the masses of the planets, by reaching a precision ranging from 3 to 5%. As a comparison, such precisions are equivalent to performing radial velocity measurements with an accuracy of $2.5 cm/sec$, which is far beyond the current and upcoming spectroscopic instruments. While extensive, the timing dataset presented here does not compete with those used by these two TTV studies.

Nevertheless, one should also notice the precision improvements between both studies, which is mostly due to the fact that more timings were considered. And these additional data, they are gathered thanks to independent transit surveys led over the years, like the one presented in this work or the Red Worlds program of the Spitzer telescope. This illustrates well that keeping measuring timing data through transit surveys is of major importance to allow future TTV studies to reach even greater accuracies and precisions..

In the future years, it is certain that more surveys of TRAPPIST-1 will be led. As now the main provider of transit data for this system, the Spitzer telescope, stopped its scientific mission, we can expect the SPECULOOS network and other ground-based observatories designed to study Ultra-Cool Dwarf stars to be the center of these observations. With the years, more information on timings will accumulate making possible to study even more in depth the dynamics of TRAPPIST-1 with the TTV method. The planetary masses and densities being fundamental parameters, an increase on their precisions will help improve a wide diversity of other studies. For instance, in the modeling of atmospheric structures, tidal heating dissipation, interior composition, and formation history.

As a final word, we have seen through this Master thesis that TRAPPIST-1 is, nowadays, already considered as a unique and fascinating system. But it is only a beginning and it is certain that the next years will bring, through TTV or other studies, a whole new set of interesting information from those seven worlds.

APPENDIX **A**

Baseline functions and correction factors

The following tables give for my 40 lightcurves the optimal baseline functions, the error correction factors, the number of photometric points, and the transit epochs. We abbreviate the time, airmass and sky respectively as t, a and s for visual clarity. / means that the baseline function is a simple normalization scalar.

UT date	**Planet(s)**	**Epoch**	**Number of points**	**Baseline**	**CF**
2019/05/21	b	862	283	$p(a^1)$	1.41
2019/05/22	d	236	305	$p(fwhm^1)$	1.03
2019/05/23	c	555	192	/	1.74
2019/05/24	b	864	180	/	1.10
2019/07/04	b	891	182	$p(a^1) + p(fwhm^1) + p(s^2)$	1.40
2019/07/10	b ; f	895 ; 109	613	$p(t^1) + p(a^2) + p(fwhm^2) + p(s^2)$	1.44
2019/07/13	c ; b	576 ; 897	311	$p(fwhm^1)$	2.32
2019/07/16	b	899	275	$p(fwhm^1)$	0.955
2019/07/28	b	907	276	$p(a^2) + p(s^1)$	1.17
2019/07/30	d ; c ; h	253 ; 583 ; 55	451	$p(fwhm^3) + p(s^2)$	1.79
2019/07/31	b	909	210	$p(a^1) + p(s^1)$	1.01
2019/08/03	d ; b	254 ; 911	642	$p(t^1) + p(a^2) + p(fwhm^2) + p(s^1)$	2.02
2019/08/11	c ; d	588 ; 256	348	$p(fwhm^2) + p(s^2)$	1.75
2019/08/28	c	595	270	$p(t^1) + p(a^1) + p(fwhm^1)$	1.60
2019/09/02	c	597	243	$p(t^2) + p(a^2) + p(fwhm^1)$	1.54
2019/09/04	b	932	276	$p(a^2) + p(fwhm^1)$	1.03

Second part on the next page.

UT date	Planet(s)	Epoch	Number of points	Baseline	CF
2019/09/10	b	936	279	$p(t^1) + p(a^1) + p(fwhm^1)$	1.52
2019/09/16	b	940	276	$p(a^2) + p(fwhm^1)$	1.17
2019/09/19	c	604	188	/	1.07
2019/09/25	b	946	192	$p(a^1) + p(fwhm^2) + p(s^1)$	1.60
2019/10/02	d	269	213	$p(fwhm^1)$	1.39
2019/10/06	c	611	278	$p(fwhm^2)$	1.43
2019/10/07	d	270	336	$p(t^2) + p(s^1)$	1.79
2019/10/18	c	616	283	$p(fwhm^1)$	1.41
2019/10/19	d	273	219	$p(fwhm^2)$	1.36
2019/10/20	e	183	284	$p(t^1) + p(a^1) + p(fwhm^2)$	1.12
2019/10/21	b	963	97	$p(a^1) + p(fwhm^1)$	0.991
2019/10/23	d	274	244	$p(fwhm^2)$	1.19
2019/10/24	b	965	210	$p(fwhm^1) + p(s^1)$	1.19
2019/10/26	e	184	367	$p(a^1) + p(fwhm^1) + p(s^2)$	1.30
2019/10/27	b	967	263	$p(a^2) + p(fwhm^2)$	1.17
2019/10/30	b	969	276	$p(a^1) + p(fwhm^2) + p(s^2) + p(xy^1)$	1.47
2019/11/01	h	60	365	$p(fwhm^1) + p(s^1)$	1.17
2019/11/02	g ; b	91 ; 971	367	$p(t^1) + p(a^2) + p(fwhm^1) + p(s^3)$	2.18
2019/11/04	c	623	266	$p(a^1)$	1.55
2019/11/05	b	973	278	$p(t^1) + p(a^1) + p(fwhm^2) + p(s^2)$	1.06
2019/11/14	b	979	209	$p(a^1) + p(fwhm^1) + p(s^2)$	1.34
2019/11/21	c	630	260	$p(t^1) + p(a^1) + p(fwhm^1)$	1.40
2019/12/20	e	193	190	$p(a^1)$	0.96
2019/12/27	d	290	136	$p(a^1) + p(fwhm^1)$	1.26

APPENDIX **B**

Individual analysis - Lightcurves

In this appendix are represented the transit lightcurves of the 40 observations of TRAPPIST-1 listed in Table 3.1, after their independent analyzes with the MCMC as detailed in Subsection 3.3.2 . On each figure is displayed:

- the corrected photometric points (grey), i.e. taking into account the detrending with their optimal baseline function (Appendix A.);
- the corrected photometric points binned per 10 minutes (black) along with the error bars;
- the best-fit model lightcurve (red).

We note that, statistically, the error of a binned photometric point decreases with n, the population size in the bin. If I had selected a binning of 5 minutes instead of 10, the error bars would have been visually more important in the figures of this Master thesis as less data are grouped in the bin. For instance, in the case where the error of each photometric point is equal to σ, then the error of the binned point is $\sigma/\sqrt{n}$.

Each figure has been built using the Python package MATPLOTLIB [98].

TRAPPIST-1b

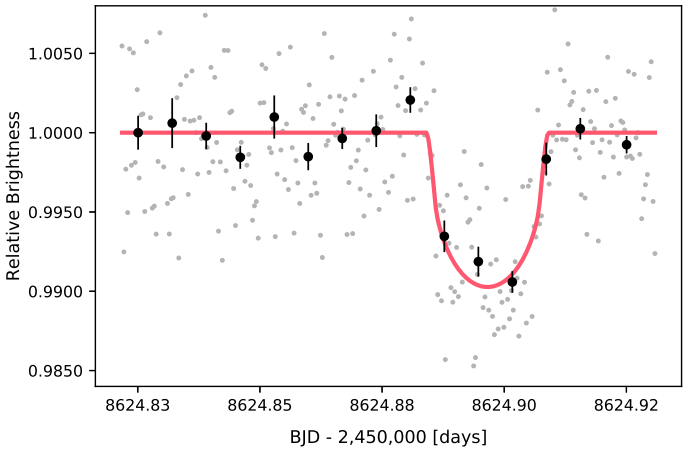

Figure B.1: Observation of 21 May 2019.

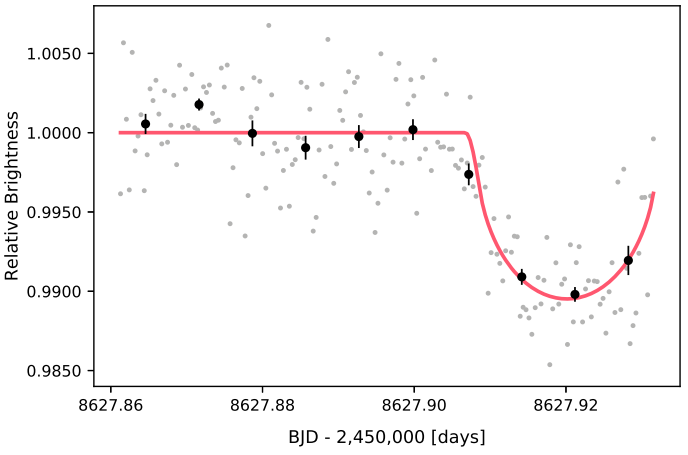

Figure B.2: Observation of 24 May 2019.

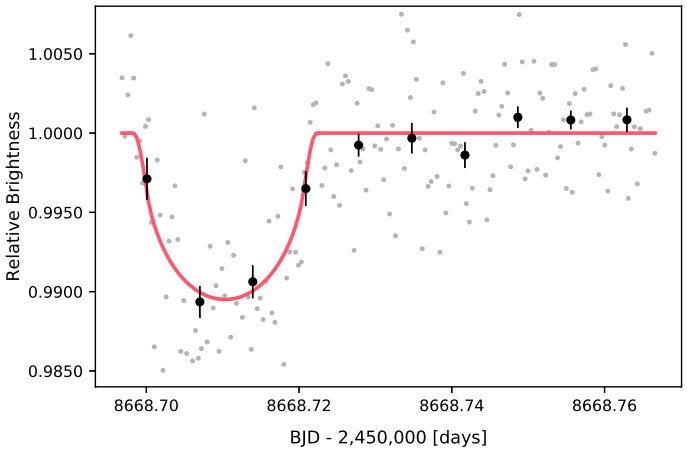

Figure B.3: Observation of 04 Jul 2019.

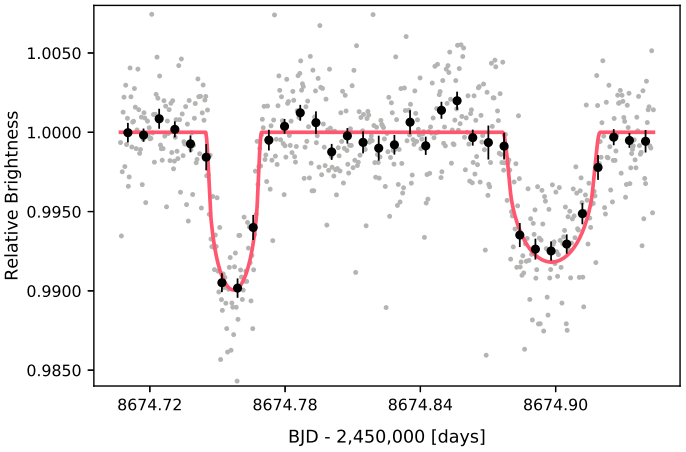

Figure B.4: Observation of 10 Jul 2019 (b ; f).

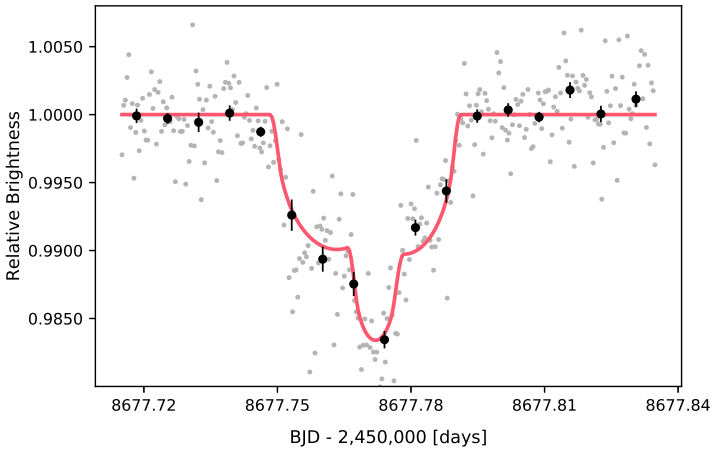

Figure B.5: Observation of 13 Jul 2019 (c ; b).

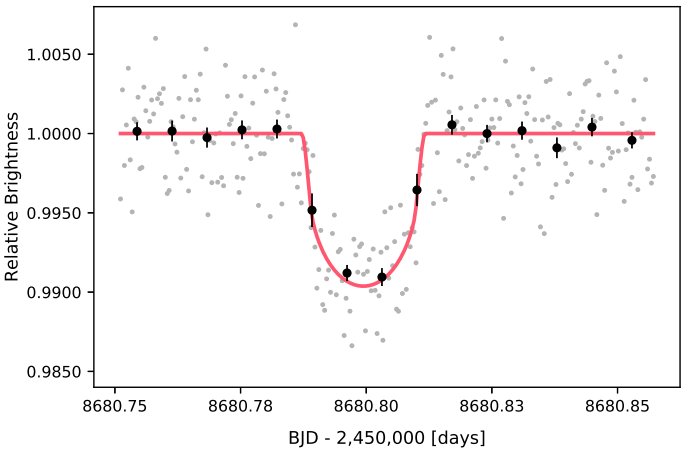

Figure B.6: Observation of 16 Jul 2019.

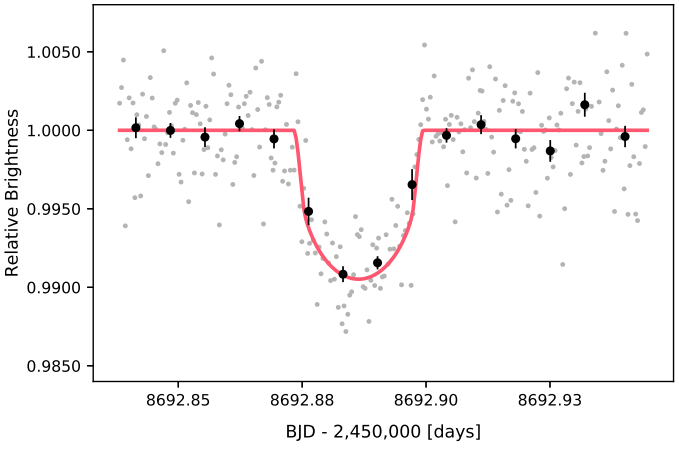

Figure B.7: Observation of 28 Jul 2019.

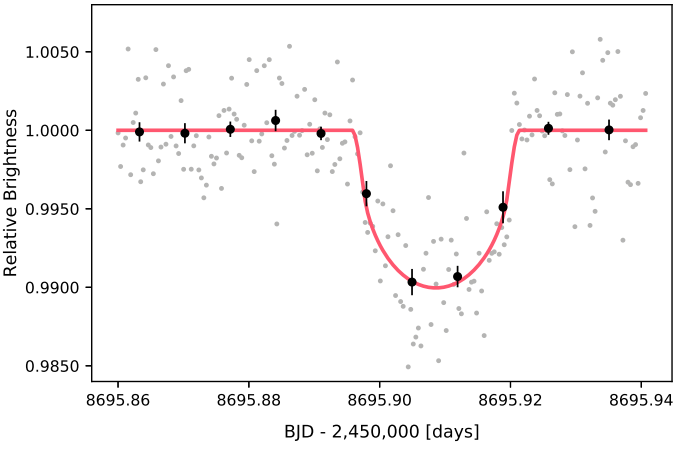

Figure B.8: Observation of 31 Jul 2019.

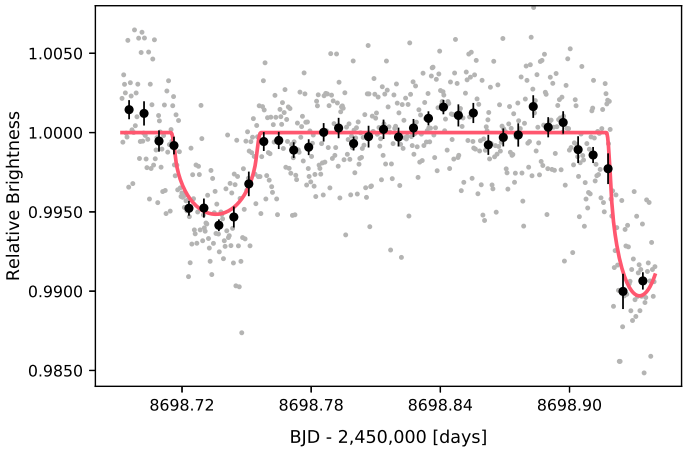

Figure B.9: Observation of 03 Aug 2019 (d ; b).

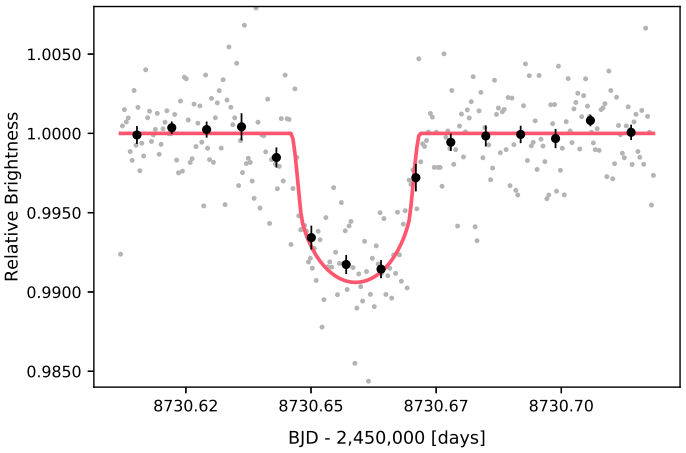

Figure B.10: Observation of 04 Sep 2019.

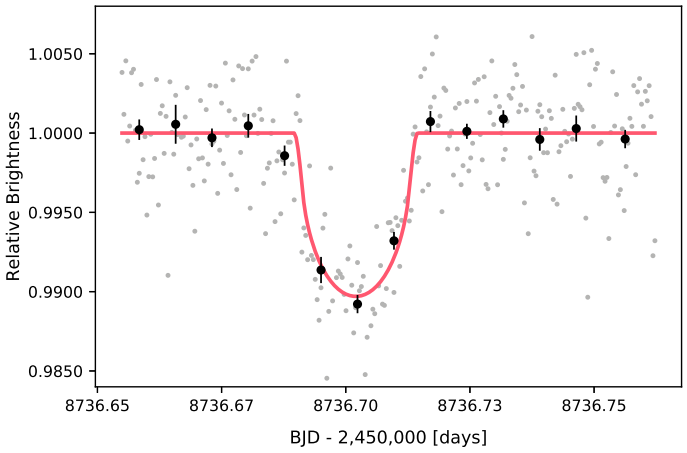

Figure B.11: Observation of 10 Sep 2019.

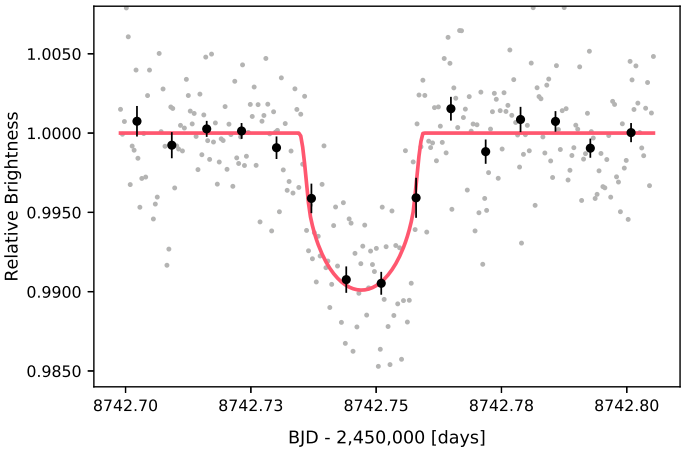

Figure B.12: Observation of 16 Sep 2019.

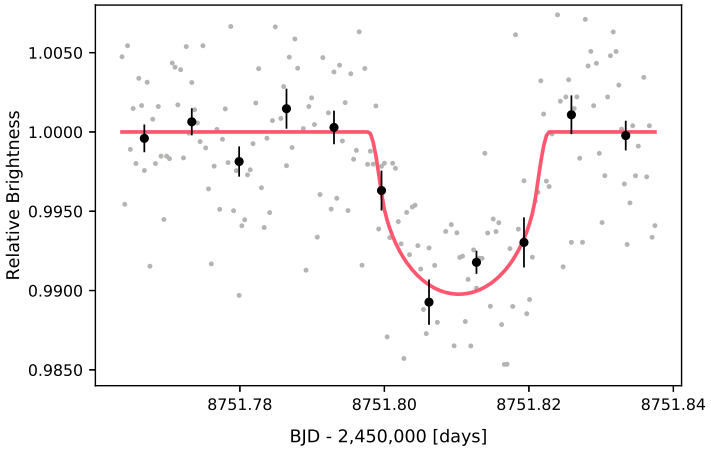

Figure B.13: Observation of 25 Sep 2019.

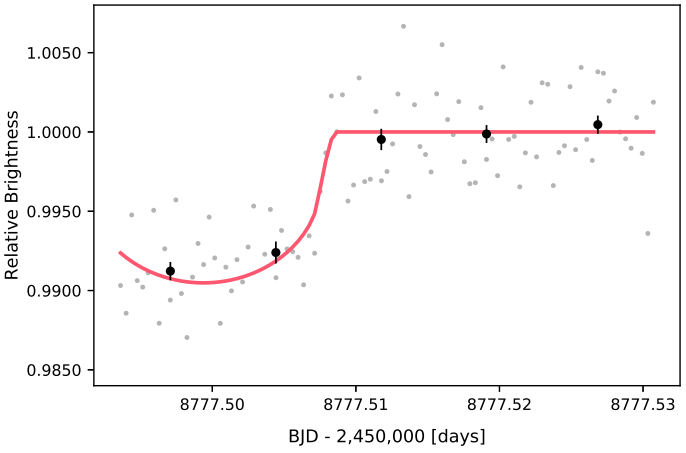

Figure B.14: Observation of 21 Oct 2019.

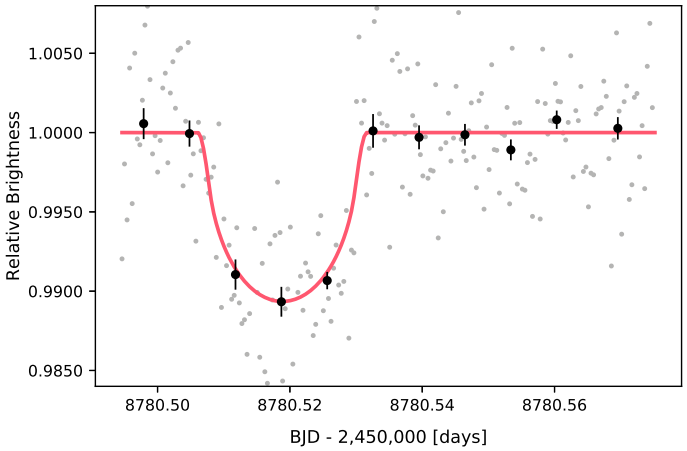

Figure B.15: Observation of 24 Oct 2019.

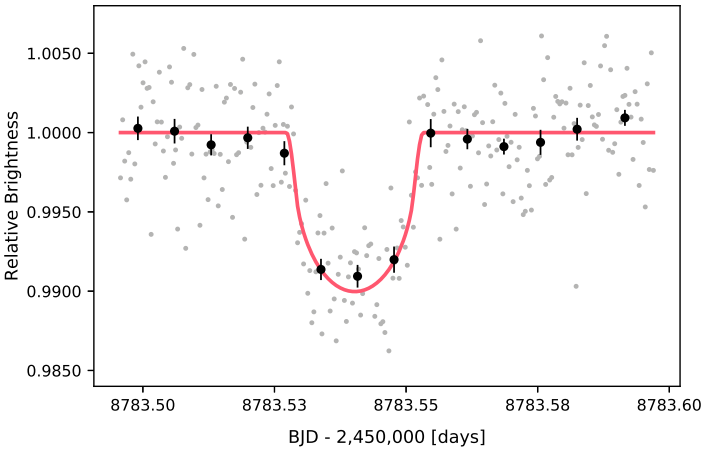

Figure B.16: Observation of 27 Oct 2019.

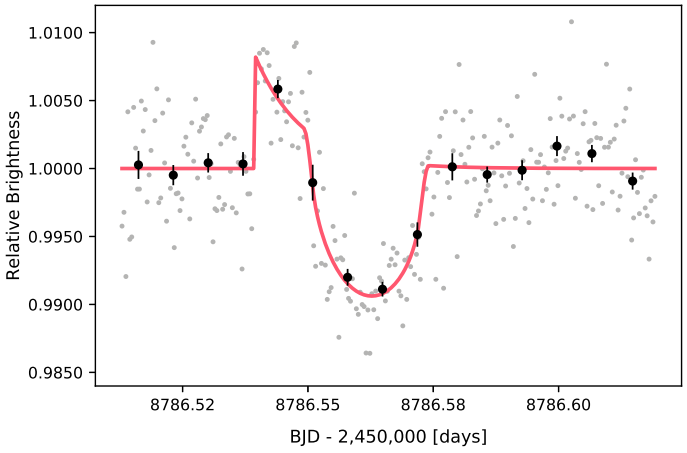

Figure B.17: Observation of 30 Oct 2019.

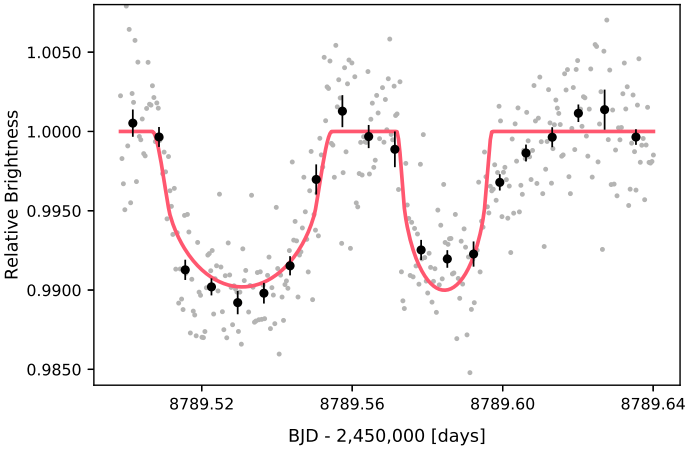

Figure B.18: Observation of 02 Nov 2019 (g ; b).

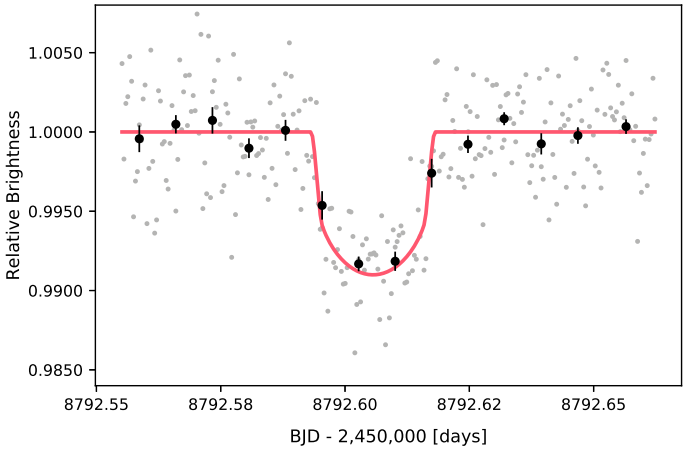

Figure B.19: Observation of 05 Nov 2019.

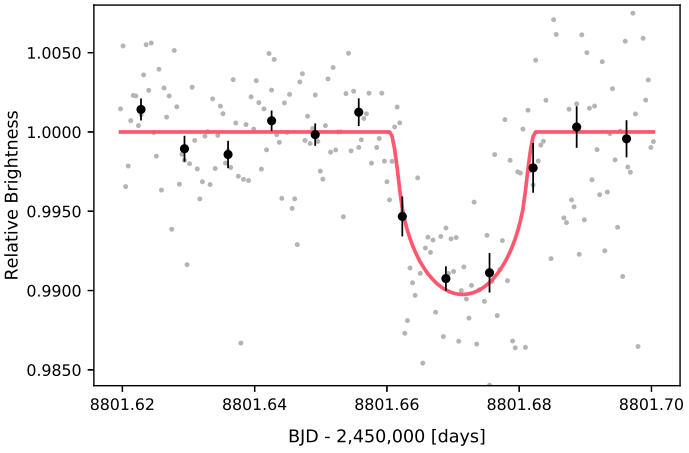

Figure B.20: Observation of 14 Nov 2019.

TRAPPIST-1c

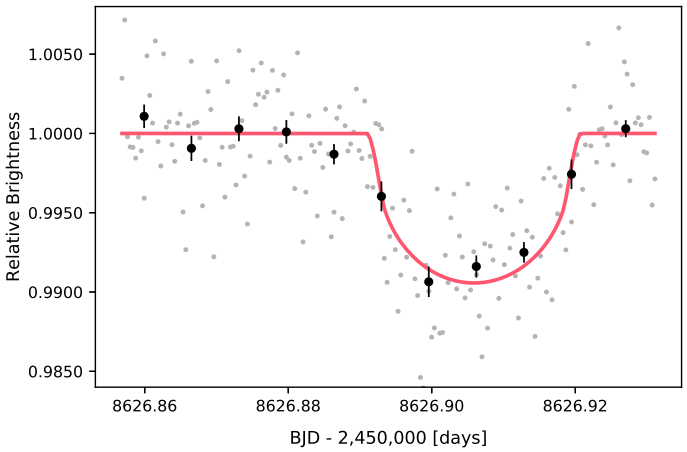

Figure B.21: Observation of 23 May 2019.

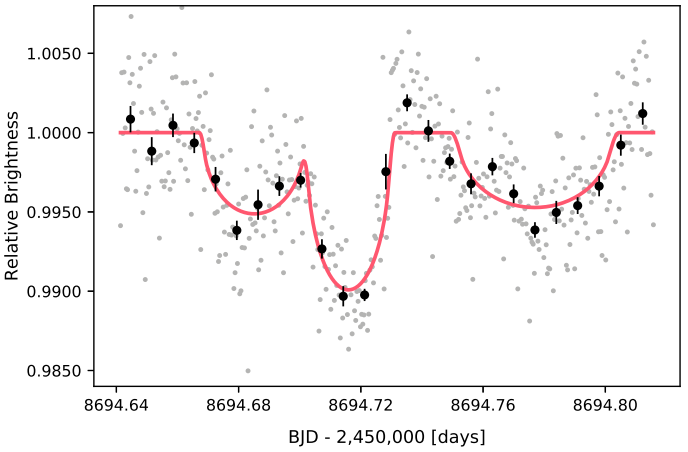

Figure B.22: Observation of 30 Jul 2019 (d ; c ; h).

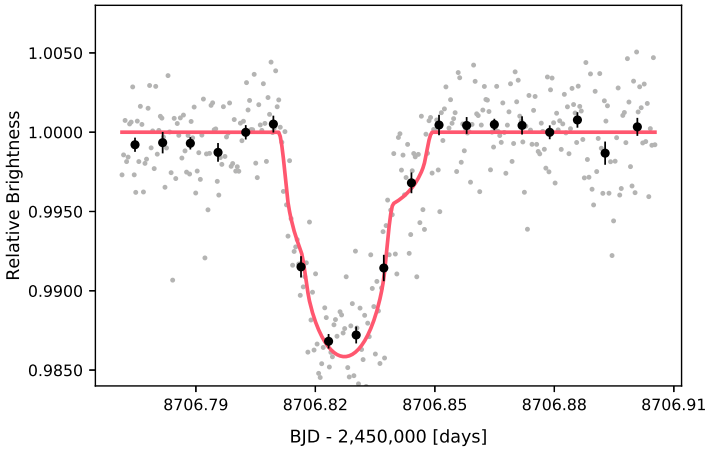

Figure B.23: Observation of 11 Aug 2019 (c ; d).

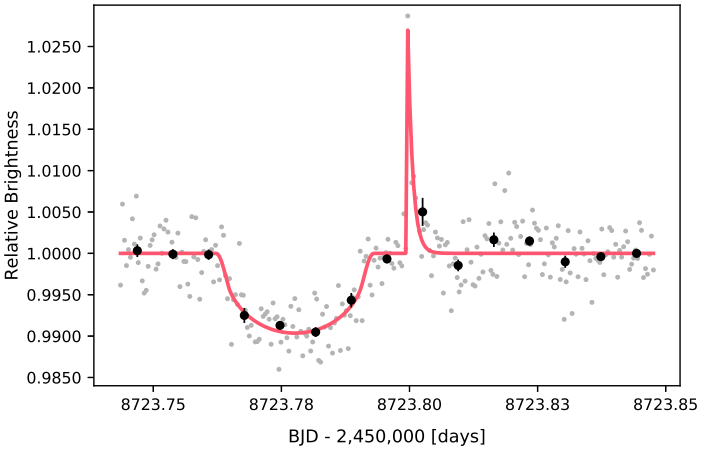

Figure B.24: Observation of 28 Aug 2019.

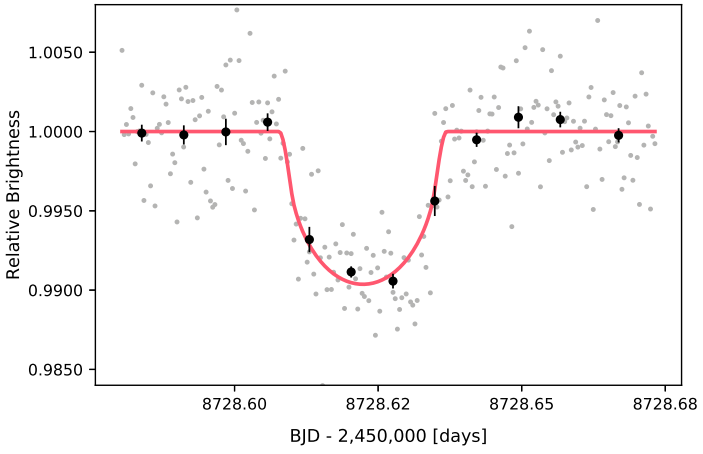

Figure B.25: Observation of 02 Sep 2019.

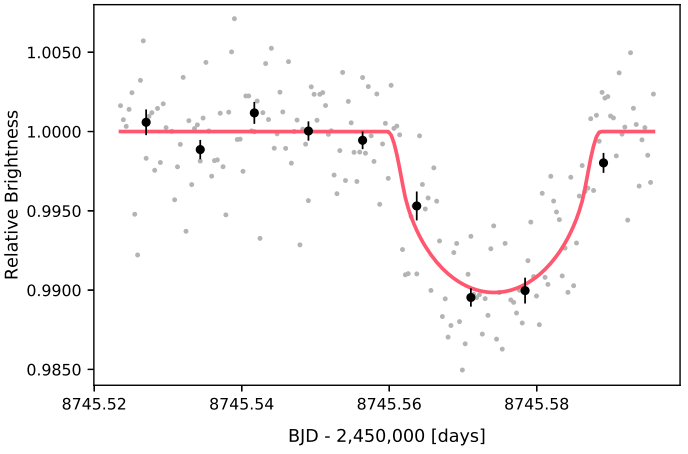

Figure B.26: Observation of 19 Sep 2019.

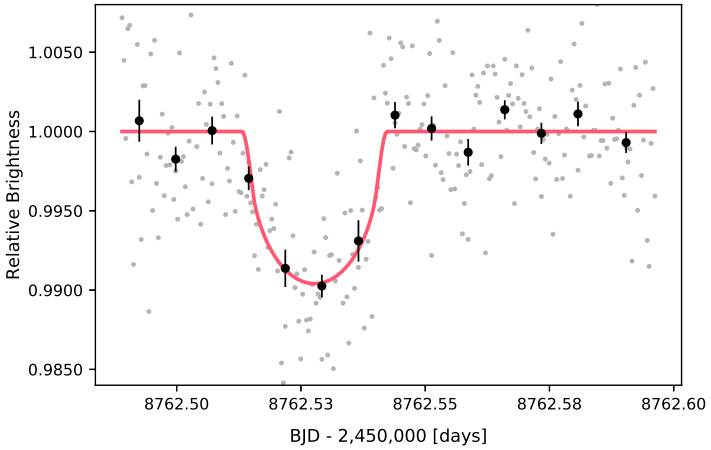

Figure B.27: Observation of 06 Oct 2019.

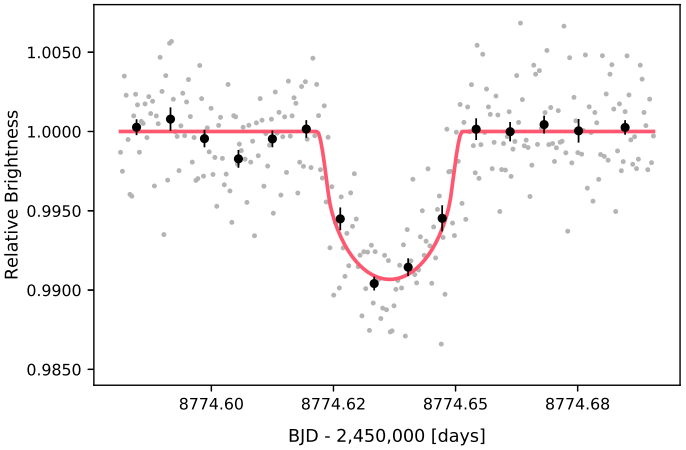

Figure B.28: Observation of 18 Oct 2019.

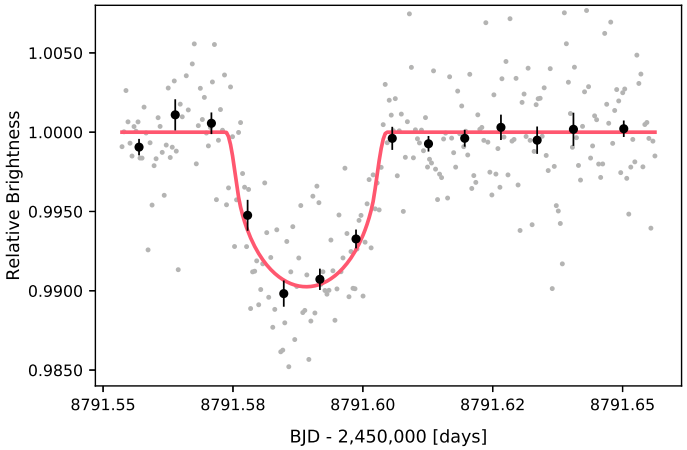

Figure B.29: Observation of 04 Nov 2019.

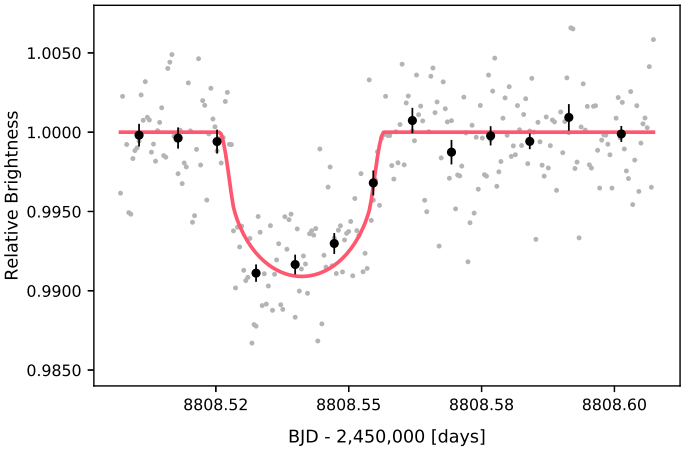

Figure B.30: Observation of 21 Nov 2019.

TRAPPIST-1d

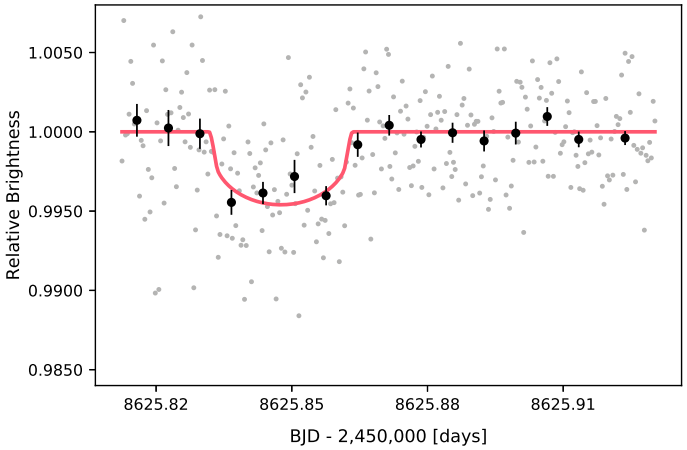

Figure B.31: Observation of 22 May 2019.

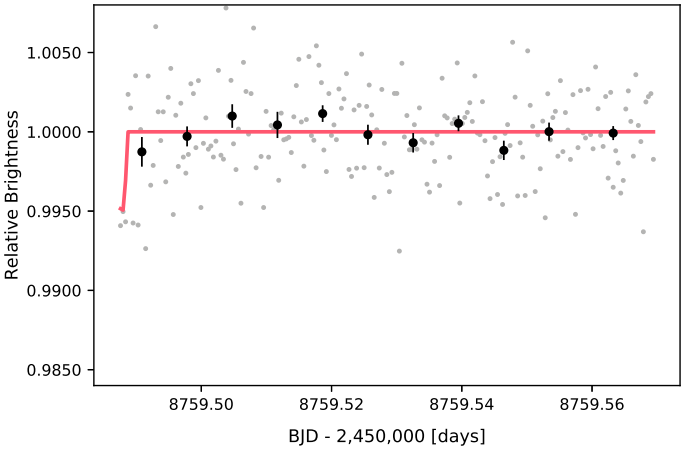

Figure B.32: Observation of 02 Oct 2019.

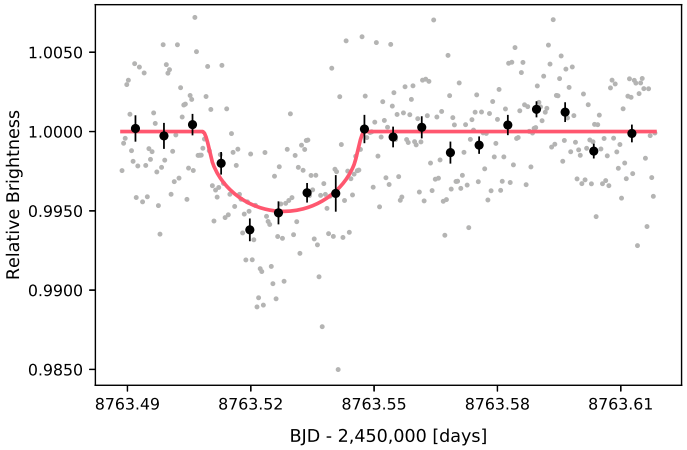

Figure B.33: Observation of 07 Oct 2019.

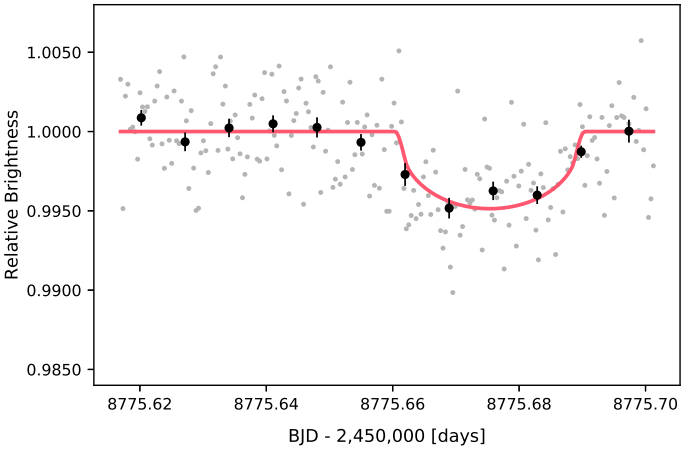

Figure B.34: Observation of 19 Oct 2019.

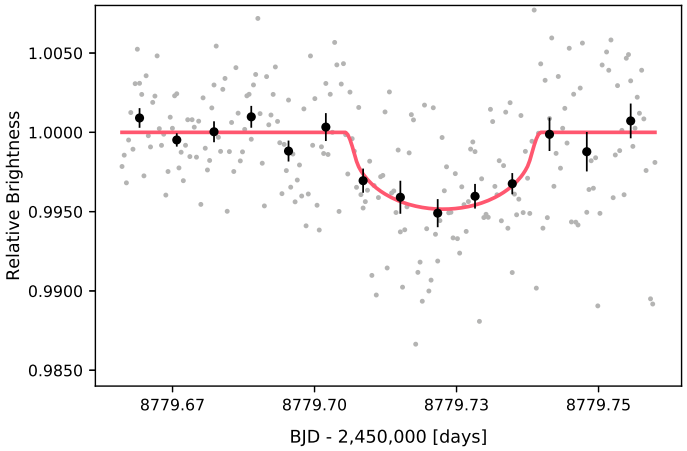

Figure B.35: Observation of 23 Oct 2019.

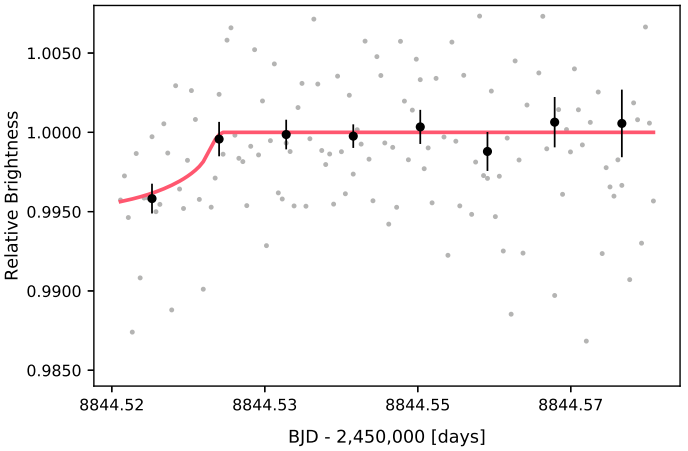

Figure B.36: Observation of 27 Dec 2019.

TRAPPIST-1e

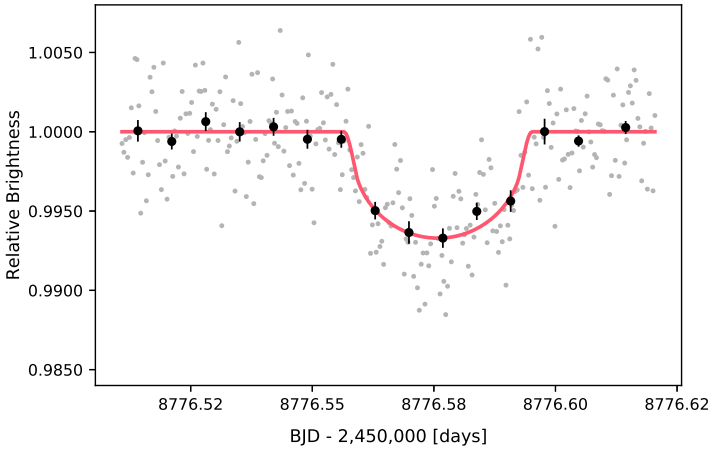

Figure B.37: Observation of 20 Oct 2019.

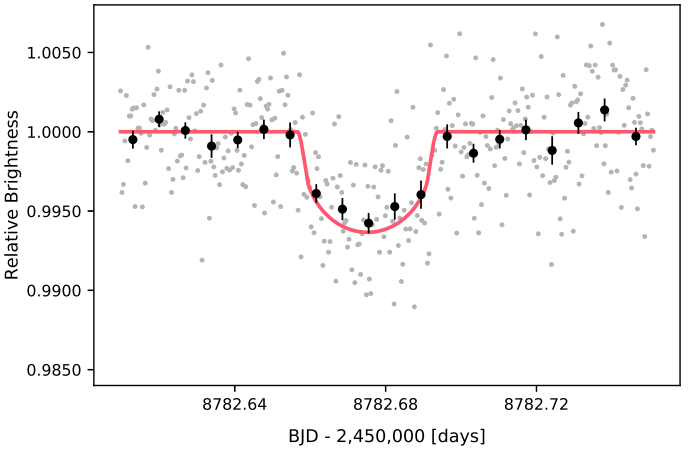

Figure B.38: Observation of 26 Oct 2019.

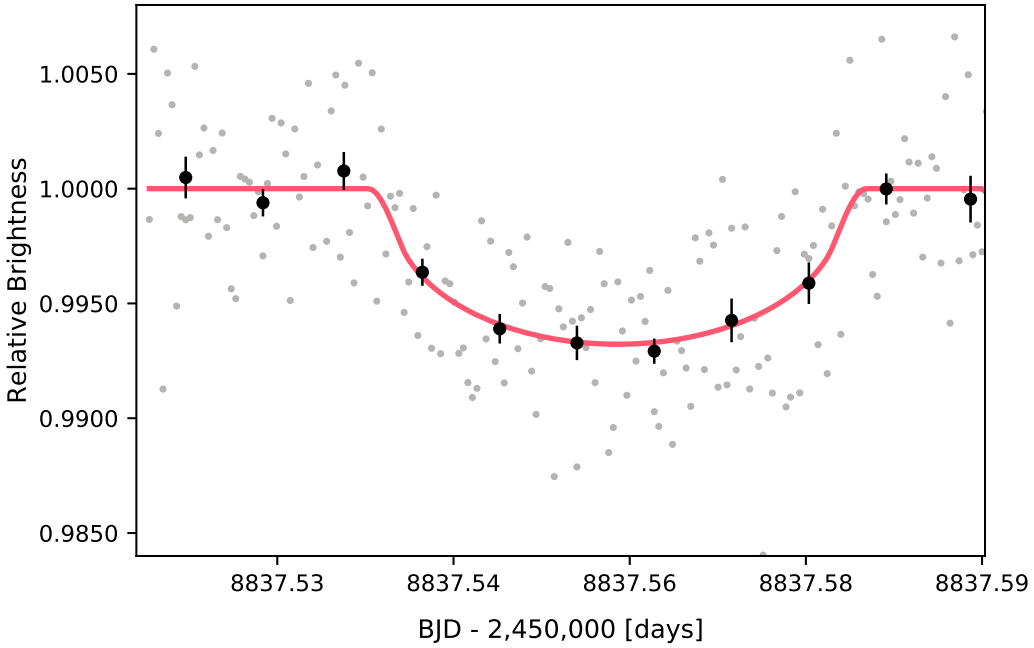

Figure B.39: Observation of 20 Dec 2019.

TRAPPIST-1h

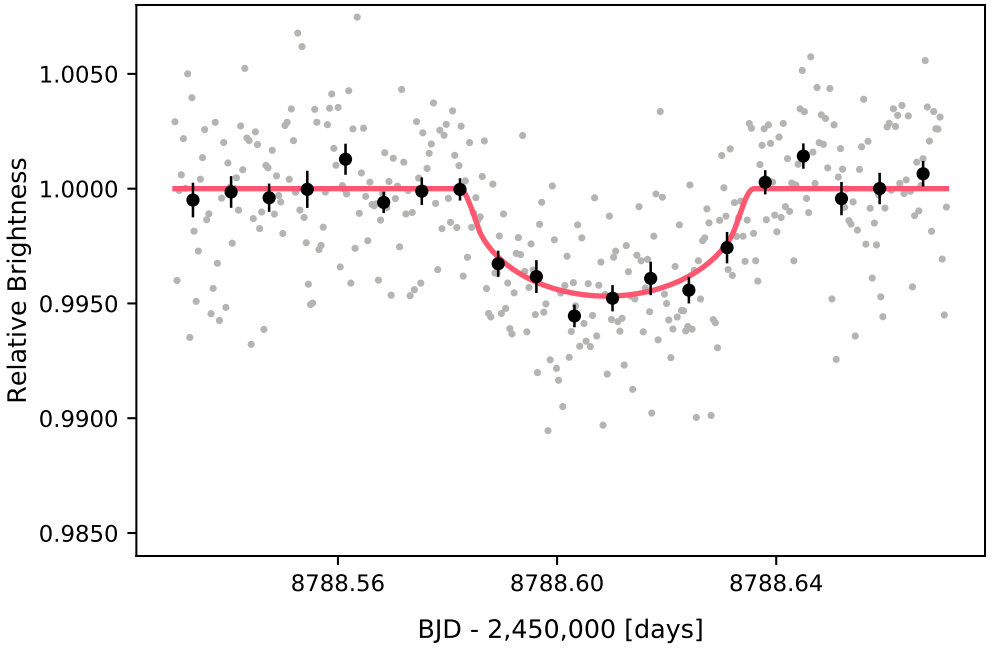

Figure B.40: Observation of 01 Nov 2019.

Bibliography

[1] R. Gomes, H. F. Levison, K. Tsiganis, and A. Morbidelli, *"Origin of the cataclysmic Late Heavy Bombardment period of the terrestrial planets"*, Nature, vol. 435, no. 7041, pp. 466–469, 2005.

[2] M. Mayor and D. Queloz, *"A Jupiter-mass companion to a solar-type star"*, Nature, vol. 378, no. 6555, pp. 355–359, 1995.

[3] "NASA Exoplanet Archive". https://exoplanetarchive.ipac.caltech.edu/exoplanetplots/. [Online; accessed in April 2020].

[4] D. Briot and J. Schneider, *"Prehistory of Transit Searches"*, arXiv preprint arXiv:1803.06896, 2018.

[5] W. Borucki, E. Dunham, D. Koch, W. Cochran, J. Rose, D. Cullers, A. Granados, and J. Jenkins, *"FRESIP: a mission to determine the character and frequency of extra-solar planets around solar-like stars"*, Astrophysics and Space Science, vol. 241, no. 1, pp. 111–134, 1996.

[6] D. Charbonneau, T. M. Brown, D. W. Latham, and M. Mayor, *"Detection of planetary transits across a sun-like star"*, The Astrophysical Journal Letters, vol. 529, no. 1, p. L45, 1999.

[7] A. Udalski, B. Paczynski, K. Zebrun, M. Szymanski, M. Kubiak, I. Soszynski, O. Szewczyk, L. Wyrzykowski, and G. Pietrzynski, *"The optical gravitational lensing experiment. Search for planetary and low-luminosity object transits in the galactic disk. Results of 2001 campaign"*, arXiv preprint astro-ph/0202320, 2002.

[8] W. J. Borucki, D. G. Koch, G. Basri, N. Batalha, A. Boss, T. M. Brown, D. Caldwell, J. Christensen-Dalsgaard, W. D. Cochran, E. DeVore, *et al.*, *"Characteristics of Kepler planetary candidates based on the first data set"*, The Astrophysical Journal, vol. 728, no. 2, p. 117, 2011.

[9] S. B. Howell, C. Sobeck, M. Haas, M. Still, T. Barclay, F. Mullally, J. Troeltzsch, S. Aigrain, S. T. Bryson, D. Caldwell, *et al.*, *"The K2 mission: characterization and early results"*, Publications of the Astronomical Society of the Pacific, vol. 126, no. 938, p. 398, 2014.

[10] D. L. Pollacco, I. Skillen, A. C. Cameron, D. J. Christian, C. Hellier, J. Irwin, T. Lister, R. Street, R. G. West, D. Anderson, *et al.*, *"The WASP project and the SuperWASP cameras"*, Publications of the Astronomical Society of the Pacific, vol. 118, no. 848, p. 1407, 2006.

[11] J. N. Winn, *"Transits and occultations"*, arXiv preprint arXiv:1001.2010, 2010.

[12] M. Perryman, *The exoplanet handbook*. Cambridge University Press, 2018.

[13] S. Seager and G. Mallen-Ornelas, *"A unique solution of planet and star parameters from an extrasolar planet transit light curve",* The Astrophysical Journal, vol. 585, no. 2, p. 1038, 2003.

[14] E. K. Baines, H. A. McAlister, T. A. Ten Brummelaar, J. Sturmann, L. Sturmann, N. H. Turner, and S. T. Ridgway, *"Eleven exoplanet host star angular diameters from the Chara array",* The Astrophysical Journal, vol. 701, no. 1, p. 154, 2009.

[15] G. Torres, J. Andersen, and A. Giménez, *"Accurate masses and radii of normal stars: modern results and applications",* The Astronomy and Astrophysics Review, vol. 18, no. 1-2, pp. 67–126, 2010.

[16] A. Claret, *"A new non-linear limb-darkening law for LTE stellar atmosphere models. Calculations for-5.0<= log [M/H]<=+ 1, 2000 K<= Teff<= 50000 K at several surface gravities",* Astronomy and Astrophysics, vol. 363, pp. 1081–1190, 2000.

[17] W. Hayek, D. Sing, F. Pont, and M. Asplund, *"Limb darkening laws for two exoplanet host stars derived from 3D stellar model atmospheres-Comparison with 1D models and HST light curve observations",* Astronomy & Astrophysics, vol. 539, p. A102, 2012.

[18] H. A. Knutson, D. Charbonneau, R. W. Noyes, T. M. Brown, and R. L. Gilliland, *"Using stellar limb-darkening to refine the properties of HD 209458b",* The Astrophysical Journal, vol. 655, no. 1, p. 564, 2007.

[19] F. Fressin, G. Torres, D. Charbonneau, S. T. Bryson, J. Christiansen, C. D. Dressing, J. M. Jenkins, L. M. Walkowicz, and N. M. Batalha, *"The false positive rate of Kepler and the occurrence of planets",* The Astrophysical Journal, vol. 766, no. 2, p. 81, 2013.

[20] S. Seager and D. D. Sasselov, *"Theoretical transmission spectra during extrasolar giant planet transits",* The Astrophysical Journal, vol. 537, no. 2, p. 916, 2000.

[21] A. M. Mandell, K. Haynes, E. Sinukoff, N. Madhusudhan, A. Burrows, and D. Deming, *"Exoplanet transit spectroscopy using WFC3: WASP-12 b, WASP-17 b, and WASP-19 b",* The Astrophysical Journal, vol. 779, no. 2, p. 128, 2013.

[22] H. R. Wakeford, D. K. Sing, T. Kataria, D. Deming, N. Nikolov, E. D. Lopez, P. Tremblin, D. S. Amundsen, N. K. Lewis, A. M. Mandell, *et al.*, *"HAT-P-26b: A Neptune-mass exoplanet with a well-constrained heavy element abundance",* Science, vol. 356, no. 6338, pp. 628–631, 2017.

[23] L. Nortmann, E. Pallé, M. Salz, J. Sanz-Forcada, E. Nagel, F. J. Alonso-Floriano, S. Czesla, F. Yan, G. Chen, I. A. Snellen, *et al.*, *"Ground-based detection of an extended helium atmosphere in the Saturn-mass exoplanet WASP-69b",* Science, vol. 362, no. 6421, pp. 1388–1391, 2018.

[24] J. Lustig-Yaeger, V. S. Meadows, and A. P. Lincowski, *"The detectability and characterization of the TRAPPIST-1 exoplanet atmospheres with JWST",* The Astronomical Journal, vol. 158, no. 1, p. 27, 2019.

[25] A. H. Triaud, A. C. Cameron, D. Queloz, D. R. Anderson, M. Gillon, L. Hebb, C. Hellier, B. Loeillet, P. F. Maxted, M. Mayor, *et al.*, *"Spin-orbit angle measurements for six*

southern transiting planets-New insights into the dynamical origins of hot Jupiters", Astronomy & Astrophysics, vol. 524, p. A25, 2010.

[26] J. N. Winn, J. A. Johnson, G. W. Marcy, R. P. Butler, S. S. Vogt, G. W. Henry, A. Roussanova, M. J. Holman, K. Enya, N. Narita, *et al.*, *"Measurement of the spin-orbit alignment in the exoplanetary system HD 189733",* The Astrophysical Journal Letters, vol. 653, no. 1, p. L69, 2006.

[27] E. Agol and D. Fabrycky, *"Transit timing and duration variations for the discovery and characterization of exoplanets",* arXiv preprint arXiv:1706.09849, 2017.

[28] J. C. Becker, A. Vanderburg, F. C. Adams, S. A. Rappaport, and H. M. Schwengeler, *"WASP-47: A hot Jupiter system with two additional planets discovered by K2",* The Astrophysical Journal Letters, vol. 812, no. 2, p. L18, 2015.

[29] S. L. Grimm, B.-O. Demory, M. Gillon, C. Dorn, E. Agol, A. Burdanov, L. Delrez, M. Sestovic, A. H. Triaud, M. Turbet, *et al.*, *"The nature of the TRAPPIST-1 exoplanets",* Astronomy & Astrophysics, vol. 613, p. A68, 2018.

[30] J. Miralda-Escudé, *"Orbital perturbations of transiting planets: A possible method to measure stellar quadrupoles and to detect Earth-mass planets",* The Astrophysical Journal, vol. 564, no. 2, p. 1019, 2002.

[31] E. Agol, J. Steffen, R. Sari, and W. Clarkson, *"On detecting terrestrial planets with timing of giant planet transits",* Monthly Notices of the Royal Astronomical Society, vol. 359, no. 2, pp. 567–579, 2005.

[32] M. J. Holman and N. W. Murray, *"The use of transit timing to detect terrestrial-mass extrasolar planets",* Science, vol. 307, no. 5713, pp. 1288–1291, 2005.

[33] M. J. Holman, D. C. Fabrycky, D. Ragozzine, E. B. Ford, J. H. Steffen, W. F. Welsh, J. J. Lissauer, D. W. Latham, G. W. Marcy, L. M. Walkowicz, *et al.*, *"Kepler-9: A system of multiple planets transiting a Sun-like star, confirmed by timing variations",* science, vol. 330, no. 6000, pp. 51–54, 2010.

[34] J. H. Steffen, D. C. Fabrycky, E. B. Ford, J. A. Carter, J.-M. Désert, F. Fressin, M. J. Holman, J. J. Lissauer, A. V. Moorhead, J. F. Rowe, *et al.*, *"Transit timing observations from Kepler–III. Confirmation of four multiple planet systems by a Fourier-domain study of anticorrelated transit timing variations",* Monthly Notices of the Royal Astronomical Society, vol. 421, no. 3, pp. 2342–2354, 2012.

[35] D. Nesvornỳ, D. Kipping, D. Terrell, J. Hartman, G. A. Bakos, and L. A. Buchhave, *"KOI-142, the king of transit variations, is a pair of planets near the 2: 1 resonance",* The Astrophysical Journal, vol. 777, no. 1, p. 3, 2013.

[36] J. D. Kirkpatrick, T. J. Henry, and D. A. Simons, *"The solar neighborhood. 2: the first list of dwarfs with spectral types of M7 and cooler",* The Astronomical Journal, vol. 109, pp. 797–807, 1995.

[37] J. E. Gizis, D. G. Monet, I. N. Reid, J. D. Kirkpatrick, J. Liebert, and R. J. Williams, *"New neighbors from 2MASS: activity and kinematics at the bottom of the main sequence",* The Astronomical Journal, vol. 120, no. 2, p. 1085, 2000.

[38] J. Liebert and J. E. Gizis, *"RI Photometry of 2MASS-selected Late M and L Dwarfs",* Publications of the Astronomical Society of the Pacific, vol. 118, no. 843, p. 659, 2006.

[39] M. Gillon, E. Jehin, P. Magain, V. Chantry, D. Hutsemékers, J. Manfroid, D. Queloz, and S. Udry, *"TRAPPIST: a robotic telescope dedicated to the study of planetary systems",* in *EPJ Web of Conferences*, vol. 11, p. 06002, EDP Sciences, 2011.

[40] E. Jehin, M. Gillon, D. Queloz, P. Magain, J. Manfroid, V. Chantry, M. Lendl, D. Hutsemékers, and S. Udry, *"TRAPPIST: TRAnsiting planets and PlanetesImals small telescope",* Msngr, vol. 145, pp. 2–6, 2011.

[41] M. Gillon, E. Jehin, S. M. Lederer, L. Delrez, J. de Wit, A. Burdanov, V. Van Grootel, A. J. Burgasser, A. H. Triaud, C. Opitom, *et al.*, *"Temperate Earth-sized planets transiting a nearby ultracool dwarf star",* Nature, vol. 533, no. 7602, pp. 221–224, 2016.

[42] M. Gillon, A. H. Triaud, B.-O. Demory, E. Jehin, E. Agol, K. M. Deck, S. M. Lederer, J. De Wit, A. Burdanov, J. G. Ingalls, *et al.*, *"Seven temperate terrestrial planets around the nearby ultracool dwarf star TRAPPIST-1",* Nature, vol. 542, no. 7642, pp. 456–460, 2017.

[43] R. Luger, M. Sestovic, E. Kruse, S. L. Grimm, B.-O. Demory, E. Agol, E. Bolmont, D. Fabrycky, C. S. Fernandes, V. Van Grootel, *et al.*, *"A seven-planet resonant chain in TRAPPIST-1",* Nature Astronomy, vol. 1, no. 6, pp. 1–8, 2017.

[44] V. Van Grootel, C. S. Fernandes, M. Gillon, E. Jehin, J. Manfroid, R. Scuflaire, A. J. Burgasser, K. Barkaoui, Z. Benkhaldoun, A. Burdanov, *et al.*, *"Stellar parameters for TRAPPIST-1",* The Astrophysical Journal, vol. 853, no. 1, p. 30, 2018.

[45] A. J. Burgasser and E. E. Mamajek, *"On the Age of the TRAPPIST-1 System",* The Astrophysical Journal, vol. 845, no. 2, p. 110, 2017.

[46] E. Ducrot *et al.*, *"TRAPPIST-1: Global Results of the Spitzer Exploration Science Program Red Worlds",* submitted, 2020.

[47] M. Gillon, E. Jehin, A. Fumel, P. Magain, and D. Queloz, *"TRAPPIST-UCDTS: A prototype search for habitable planets transiting ultra-cool stars",* in *EPJ Web of Conferences*, vol. 47, p. 03001, EDP Sciences, 2013.

[48] V. Bourrier, D. Ehrenreich, P. Wheatley, E. Bolmont, M. Gillon, J. de Wit, A. Burgasser, E. Jehin, D. Queloz, and A. Triaud, *"Reconnaissance of the TRAPPIST-1 exoplanet system in the Lyman-α line",* Astronomy & Astrophysics, vol. 599, p. L3, 2017.

[49] L. Delrez, M. Gillon, D. Queloz, B.-O. Demory, Y. Almleaky, J. de Wit, E. Jehin, A. H. Triaud, K. Barkaoui, A. Burdanov, *et al.*, *"SPECULOOS: a network of robotic telescopes to hunt for terrestrial planets around the nearest ultracool dwarfs",* in *Ground-based and Airborne Telescopes VII*, vol. 10700, p. 107001I, International Society for Optics and Photonics, 2018.

[50] Y. Miguel, A. Cridland, C. Ormel, J. Fortney, and S. Ida, *"Diverse outcomes of planet formation and composition around low-mass stars and brown dwarfs",* Monthly Notices of the Royal Astronomical Society, vol. 491, no. 2, pp. 1998–2009, 2020.

[51] J. R. Cantrell, T. J. Henry, and R. J. White, *"The solar neighborhood XXIX: the habitable real estate of our nearest stellar neighbors",* The Astronomical Journal, vol. 146, no. 4, p. 99, 2013.

[52] S. Peacock, T. Barman, E. L. Shkolnik, P. H. Hauschildt, and E. Baron, *"Predicting the extreme ultraviolet radiation environment of exoplanets around Low-mass stars: the TRAPPIST-1 system",* The Astrophysical Journal, vol. 871, no. 2, p. 235, 2019.

[53] C. Garraffo, J. J. Drake, O. Cohen, J. D. Alvarado-Gómez, and S. P. Moschou, *"The threatening magnetic and plasma environment of the TRAPPIST-1 planets",* The Astrophysical Journal Letters, vol. 843, no. 2, p. L33, 2017.

[54] J. Guo and L. Ben-Jaffel, *"The influence of the extreme ultraviolet spectral energy distribution on the structure and composition of the upper atmosphere of exoplanets",* The Astrophysical Journal, vol. 818, no. 2, p. 107, 2016.

[55] R. Luger and R. Barnes, *"Extreme water loss and abiotic O2 buildup on planets throughout the habitable zones of M dwarfs",* Astrobiology, vol. 15, no. 2, pp. 119–143, 2015.

[56] M. J. Heath, L. R. Doyle, M. M. Joshi, and R. M. Haberle, *"Habitability of planets around red dwarf stars",* Origins of Life and Evolution of the Biosphere, vol. 29, no. 4, pp. 405–424, 1999.

[57] J. T. O'Malley-James and L. Kaltenegger, *"UV surface habitability of the TRAPPIST-1 system",* Monthly Notices of the Royal Astronomical Society: Letters, vol. 469, no. 1, pp. L26–L30, 2017.

[58] A. Valio, R. Estrela, L. Cabral, and A. Grangeiro, *"The biological impact of superflares on planets in the Habitable Zone",* International Astronomical Union. Proceedings of the International Astronomical Union, vol. 14, no. S345, pp. 176–180, 2018.

[59] P. B. Rimmer, J. Xu, S. J. Thompson, E. Gillen, J. D. Sutherland, and D. Queloz, *"The origin of RNA precursors on exoplanets",* Science advances, vol. 4, no. 8, p. eaar3302, 2018.

[60] R. R. Paudel, J. E. Gizis, D. Mullan, S. J. Schmidt, A. J. Burgasser, P. K. Williams, A. Youngblood, and K. Stassun, *"K 2 Ultracool Dwarfs Survey–V. High superflare rates on rapidly rotating late-M dwarfs",* Monthly Notices of the Royal Astronomical Society, vol. 486, no. 1, pp. 1438–1447, 2019.

[61] C. Dong, M. Jin, M. Lingam, V. S. Airapetian, Y. Ma, and B. van der Holst, *"Atmospheric escape from the TRAPPIST-1 planets and implications for habitability",* Proceedings of the National Academy of Sciences, vol. 115, no. 2, pp. 260–265, 2018.

[62] "HORIZONS Web-Interface - JPL Solar System Dynamics". https://ssd.jpl.nasa.gov/horizons.cgi. [Online; accessed in March 2020].

[63] R. K. Kopparapu, R. Ramirez, J. F. Kasting, V. Eymet, T. D. Robinson, S. Mahadevan, R. C. Terrien, S. Domagal-Goldman, V. Meadows, and R. Deshpande, *"Habitable zones around main-sequence stars: new estimates",* The Astrophysical Journal, vol. 765, no. 2, p. 131, 2013.

[64] D. Tamayo, H. Rein, C. Petrovich, and N. Murray, *"Convergent migration renders TRAPPIST-1 long-lived",* The Astrophysical Journal Letters, vol. 840, no. 2, p. L19, 2017.

[65] X. Bonfils, X. Delfosse, S. Udry, T. Forveille, M. Mayor, C. Perrier, F. Bouchy, M. Gillon, C. Lovis, F. Pepe, *et al.*, *"The HARPS search for southern extra-solar planets-XXXI. The M-dwarf sample",* Astronomy & Astrophysics, vol. 549, p. A109, 2013.

[66] F. A. Pepe, S. Cristiani, R. R. Lopez, N. C. Santos, A. Amorim, G. Avila, W. Benz, P. Bonifacio, A. Cabral, P. Carvas, *et al.*, *"ESPRESSO: the Echelle spectrograph for rocky exoplanets and stable spectroscopic observations",* in *Ground-based and Airborne Instrumentation for Astronomy III*, vol. 7735, p. 77350F, International Society for Optics and Photonics, 2010.

[67] B. Klein and J.-F. Donati, *"Simulating radial velocity observations of TRAPPIST-1 with SPIRou",* Monthly Notices of the Royal Astronomical Society, vol. 488, no. 4, pp. 5114–5126, 2019.

[68] F. Wildi, N. Blind, V. Reshetov, O. Hernandez, L. Genolet, U. Conod, M. Sordet, A. Segovilla, J. Rasilla, D. Brousseau, *et al.*, *"NIRPS: an adaptive-optics assisted radial velocity spectrograph to chase exoplanets around M-stars",* in *Techniques and Instrumentation for Detection of Exoplanets VIII*, vol. 10400, p. 1040018, International Society for Optics and Photonics, 2017.

[69] D. D. B. Koll, "A Scaling Theory for Atmospheric Heat Redistribution on Rocky Exoplanets", 2019.

[70] A. C. Barr, V. Dobos, and L. L. Kiss, *"Interior structures and tidal heating in the TRAPPIST-1 planets",* Astronomy & Astrophysics, vol. 613, p. A37, 2018.

[71] G. J. Veeder, D. L. Matson, T. V. Johnson, A. G. Davies, and D. L. Blaney, *"The polar contribution to the heat flow of Io",* Icarus, vol. 169, no. 1, pp. 264–270, 2004.

[72] J. Tjoa, M. Mueller, and F. F. S. van der Tak, "The subsurface habitability of small, icy exomoons", 2020.

[73] J. de Wit, H. R. Wakeford, M. Gillon, N. K. Lewis, J. A. Valenti, B.-O. Demory, A. J. Burgasser, A. Burdanov, L. Delrez, E. Jehin, *et al.*, *"A combined transmission spectrum of the Earth-sized exoplanets TRAPPIST-1 b and c",* Nature, vol. 537, no. 7618, pp. 69–72, 2016.

[74] J. de Wit, H. R. Wakeford, N. K. Lewis, L. Delrez, M. Gillon, F. Selsis, J. Leconte, B.-O. Demory, E. Bolmont, V. Bourrier, *et al.*, *"Atmospheric reconnaissance of the habitable-zone Earth-sized planets orbiting TRAPPIST-1",* Nature Astronomy, vol. 2, no. 3, pp. 214–219, 2018.

[75] H. R. Wakeford, N. K. Lewis, J. Fowler, G. Bruno, T. J. Wilson, S. E. Moran, J. Valenti, N. E. Batalha, J. Filippazzo, V. Bourrier, *et al.*, *"Disentangling the planet from the star in late-type M dwarfs: a case study of TRAPPIST-1g",* The Astronomical Journal, vol. 157, no. 1, p. 11, 2018.

[76] E. Agol *et al.*, *"Refining the transit timing and photometric analysis of TRAPPIST-1: Masses, radii, densities, eccentricities, and ephemerides.",* in prep., 2020.

[77] "SPECULOOS project - University of Liège". https://www.speculoos.uliege.be/cms/c_4532838/en/speculoos-le-projet. [Online; accessed in April 2020].

[78] D. Sebastian, M. Gillon, E. Ducrot, and D. Queloz, *"The SPECULOOS project: target list and strategy",* in prep., 2020.

[79] R. Cutri, M. Skrutskie, S. Van Dyk, C. Beichman, J. Carpenter, T. Chester, L. Cambresy, T. Evans, J. Fowler, J. Gizis, *et al.*, *"Vizier online data catalog: 2MASS all-sky catalog of point sources (Cutri+ 2003)",* VizieR online data catalog, vol. 2246, 2003.

[80] "Observability date". https://observability.date/. [Online; accessed in May 2020].

[81] R. Cutri, E. Wright, T. Conrow, *et al.*, "VizieR Online Data Catalog: II/311", 2012.

[82] C. Murray *et al.*, *"Photometry and Performance of SPECULOOS-South",* in prep., 2020.

[83] B. D. Warner *et al.*, *A practical guide to lightcurve photometry and analysis*, vol. 300. Springer, 2006.

[84] R. R. Laher, V. Gorjian, L. M. Rebull, F. J. Masci, J. W. Fowler, G. Helou, S. R. Kulkarni, and N. M. Law, *"Aperture photometry tool",* Publications of the Astronomical Society of the Pacific, vol. 124, no. 917, p. 737, 2012.

[85] L. Bradley, B. Sipőcz, T. Robitaille, E. Tollerud, Z. Vinícius, C. Deil, K. Barbary, H. M. Günther, M. Cara, I. Busko, S. Conseil, M. Droettboom, A. Bostroem, E. M. Bray, L. A. Bratholm, T. Wilson, M. Craig, G. Barentsen, S. Pascual, A. Donath, J. Greco, G. Perren, P. L. Lim, and W. Kerzendorf, "astropy/photutils: v0.6", Jan. 2019.

[86] C. Broeg, M. Fernández, and R. Neuhäuser, *"A new algorithm for differential photometry: computing anoptimum artificial comparison star",* Astronomische Nachrichten: Astronomical Notes, vol. 326, no. 2, pp. 134–142, 2005.

[87] M. Gillon, A. Triaud, J. Fortney, B.-O. Demory, E. Jehin, M. Lendl, P. Magain, P. Kabath, D. Queloz, R. Alonso, *et al.*, *"The TRAPPIST survey of southern transiting planets-I. Thirty eclipses of the ultra-short period planet WASP-43 b",* Astronomy & Astrophysics, vol. 542, p. A4, 2012.

[88] K. Mandel and E. Agol, *"Analytic light curves for planetary transit searches",* The Astrophysical Journal Letters, vol. 580, no. 2, p. L171, 2002.

[89] D. Van Ravenzwaaij, P. Cassey, and S. D. Brown, *"A simple introduction to Markov Chain Monte–Carlo sampling",* Psychonomic bulletin & review, vol. 25, no. 1, pp. 143–154, 2018.

[90] A. Claret, P. Hauschildt, and S. Witte, *"New limb-darkening coefficients for PHOENIX/1D model atmospheres-I. Calculations for 1500 K < Teff < 4800 K Kepler, CoRot, Spitzer, uvby, UBVRIJHK, Sloan, and 2MASS photometric systems",* Astronomy & Astrophysics, vol. 546, p. A14, 2012.

[91] P. Gregory, *"A Bayesian analysis of extrasolar planet data for HD 73526",* The Astrophysical Journal, vol. 631, no. 2, p. 1198, 2005.

[92] E. B. Ford, *"Quantifying the uncertainty in the orbits of extrasolar planets",* The Astronomical Journal, vol. 129, no. 3, p. 1706, 2005.

[93] J. Eastman, R. Siverd, and B. S. Gaudi, *"Achieving better than 1 minute accuracy in the heliocentric and barycentric Julian dates"*, Publications of the Astronomical Society of the Pacific, vol. 122, no. 894, p. 935, 2010.

[94] "Barycentric Julian Date conversion - J.Eastman". http://astroutils.astronomy.ohio-state.edu/time/utc2bjd.html. [Online; accessed in April 2020].

[95] M. Gillon, A. Lanotte, T. Barman, N. Miller, B.-O. Demory, M. Deleuil, J. Montalbán, F. Bouchy, A. C. Cameron, H. Deeg, *et al.*, *"The thermal emission of the young and massive planet CoRoT-2b at 4.5 and 8 μm"*, Astronomy & Astrophysics, vol. 511, p. A3, 2010.

[96] G. Schwarz, *"Estimating the Dimension of a Model"*, Annals of Statistics, vol. 6, pp. 461–464, 03 1978.

[97] L. Delrez, M. Gillon, A. Triaud, B.-O. Demory, J. de Wit, J. Ingalls, E. Agol, E. Bolmont, A. Burdanov, A. Burgasser, *et al.*, *"Early 2017 observations of TRAPPIST-1 with Spitzer"*, Monthly Notices of the Royal Astronomical Society, vol. 475, no. 3, pp. 3577–3597, 2018.

[98] J. D. Hunter, *"Matplotlib: A 2D graphics environment"*, Computing in Science & Engineering, vol. 9, no. 3, pp. 90–95, 2007.

[99] T. Shibayama, H. Maehara, S. Notsu, Y. Notsu, T. Nagao, S. Honda, T. T. Ishii, D. Nogami, and K. Shibata, *"Superflares on solar-type stars observed with Kepler. I. Statistical properties of superflares"*, The Astrophysical Journal Supplement Series, vol. 209, no. 1, p. 5, 2013.

[100] D. Ragozzine and M. Holman, *"The Value of Systems with Multiple Transiting Planets, ArXiv e-prints"*, arXiv preprint arXiv:1006.3727, 2010.

[101] T. Hirano, N. Narita, B. Sato, Y. H. Takahashi, K. Masuda, Y. Takeda, W. Aoki, M. Tamura, and Y. Suto, *"Planet-planet eclipse and the Rossiter-McLaughlin effect of a multiple transiting system: joint analysis of the Subaru spectroscopy and the Kepler photometry"*, The Astrophysical Journal Letters, vol. 759, no. 2, p. L36, 2012.